

POLITECNICO DI TORINO

Master of Science in Mechatronic Engineering

Academic year 2022/2023

Master Thesis

**Composites fatigue analysis of the 15 MW offshore  
reference wind turbine blade in BECAS and  
OpenFAST**



**Politecnico  
di Torino**

**Supervisor:**

Giovanni Bracco

**Advisor:**

Massimo Sirigu

**Candidate:**

Álvaro Moreno

March 2023



# Abstract

Wind energy is becoming one of the best renewable energy options. In recent years, offshore wind turbines have been developed, moving away from the coast, searching for a higher quality wind resource with a lower environmental impact. However, the greater the distance from the coast, the deeper the sea depth, making the cost of fixed foundations prohibitively expensive.

It is in this context that floating wind turbines have been developed. The design and simulation stages are of great importance to reduce their maintenance to a minimum, given their great distance from the coast, and to guarantee maximum service life. In this thesis, composites fatigue theory is applied to predict the service life of the blades for the 15 MW offshore reference wind turbine, developed by the International Energy Agency, operating on a semi-submersible platform, under a realistic set of load cases.

Firstly, an overview of wind energy in the world is presented, with a special focus on both fixed and floating offshore energy. Trends in recent years and expectations for the years to come are analysed in the first chapter. The thesis continues by introducing in the second chapter the theoretical basis of fatigue, with special attention to its application to wind turbines.

Once the theoretical foundations have been laid, the 15 MW offshore reference wind turbine, its blades and the semi-submersible platform are presented in the third chapter, continuing with the methodology applied in the work, set out in the fourth chapter.

The following chapters develop this methodology. The environmental conditions and load cases are described to represent a realistic case of power production on a specific location, and the wind turbine is simulated under these conditions with the help of OpenFAST as the simulation tool. The results of the simulations are presented in chapter five.

For the fatigue analysis, the simulation results are post-processed with the help of the software BECAS, to obtain the stress cycle at multiple points of various blade cross-sections and finally compute the estimation of service life of the blade. The fatigue analysis and its results are presented in chapter six.

The final section presents the conclusions of the thesis and the final results are discussed.

# Contents

1.	Introduction to the offshore wind energy .....	1
1.1.	Wind energy overlook.....	1
1.2.	Offshore wind energy.....	3
1.3.	Floating offshore wind turbines .....	5
2.	Fatigue theory .....	7
2.1.	Fatigue parameters .....	8
2.2.	S-N curve .....	10
2.3.	Constant life diagrams.....	11
3.	System description .....	13
3.1.	IEA 15-MW Offshore Reference Wind Turbine.....	14
3.2.	Blades .....	14
3.2.1.	Blade aerodynamic properties .....	15
3.2.2.	Blade structural properties .....	16
3.3.	VoltturnUS-S Reference Platform.....	17
3.4.	Controller .....	18
3.4.1.	Generator Torque Controller and blade pitch controller.....	19
3.4.2.	Additional Control Modules .....	19
4.	Methodology.....	21
5.	Aeroelastic simulations .....	24
5.1.	Understanding BeamDyn .....	24
5.2.	Input files.....	25
5.2.1.	Primary input file.....	25
5.2.2.	Blade input file .....	27
5.2.3.	Other input parameters .....	28
5.3.	Setting the simulation parameters .....	29
5.4.	Design load case.....	37
5.4.1.	Site environmental conditions .....	37
5.4.2.	Applied forces on the blade .....	38

5.5.	Simulation results.....	42
5.5.1.	Power .....	43
5.5.2.	Rotor speed .....	43
5.5.3.	DOF of the platform .....	44
5.5.4.	Blade pitch angle .....	45
5.5.5.	DOF of the blade tip .....	46
5.5.6.	DOF of the blade nodes.....	47
5.5.7.	Internal forces at the blade root .....	48
5.5.8.	Internal forces at the blade nodes .....	50
6.	Fatigue analysis .....	52
6.1.	Fatigue analysis on the blade root .....	52
6.1.1.	Stress recovery .....	53
6.1.2.	Damage and life calculation .....	54
6.1.3.	Results analysis.....	58
6.2.	Fatigue analysis on blade sections .....	60
6.2.1.	Postprocessing of the forces .....	60
6.2.2.	Cross-sections properties.....	63
6.2.3.	Stress recovery .....	67
6.2.4.	Damage and life calculation .....	71
6.2.5.	Results analysis.....	73
	Conclusions .....	75
	References.....	76
	List of figures .....	78
	List of tables .....	80

# 1. Introduction to the offshore wind energy

The constant growth of the world's population and the evolution of mankind, accompanied by the quest to improve the quality of life, have led to a steady increase in global energy demand in recent decades. The high dependence on fossil fuels has led to several problems, such as climate change, air pollution and the depletion of the planet's natural resources. It is therefore necessary to search for technologies to exploit renewable energies that allow mankind to meet its energy needs in a sustainable manner. Among them, wind energy is one of the most attractive, as it is available everywhere on the planet with a potential far greater than human energy demand.

## 1.1. Wind energy overlook

Wind energy is the most mature and developed of the renewable energies. Since ancient times, it has been used to propel sailing ships or to move the machinery of windmills through its blades, taking advantage of the kinetic energy of air currents. Since the beginning of the twentieth century and based on the same principle, it has been used to generate electricity through wind turbines. In these devices, the rotor blades, hit by the wind, cause a central axis to rotate. This motion is transferred through a gearbox to an electrical generator which is connected to the grid. Different configurations of wind turbine exist, with vertical or horizontal axis and different number of blades, however the chosen configuration in most of the cases is the horizontal, three bladed wind turbine. Based on its location, wind turbines can be either onshore or offshore [1].

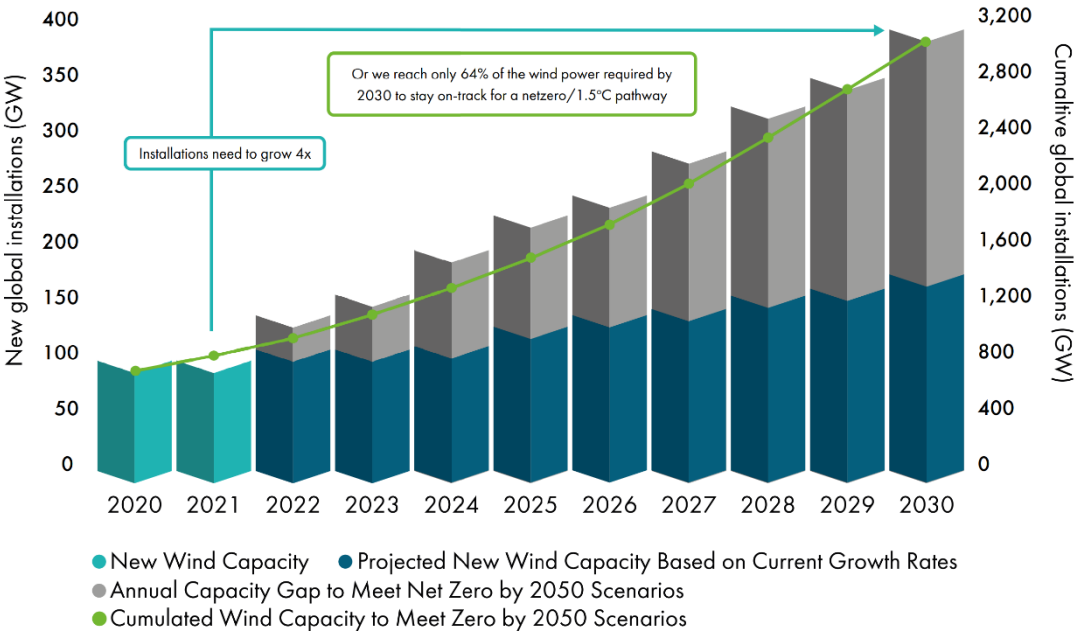


Figure 1. New worldwide wind capacity predictions (2020-2030) [2]

The strong growth of the wind industry in recent years is not surprising. 2021 has been its second-best year, with growth only 1.8% lower than 2020, despite the situation of the COVID-

19 pandemic. A total of 93.6 GW in new installations adds up to a total capacity of 837 GW, with an annual growth of 12%. Unfortunately, this rate of growth is not enough to achieve a safe and resilient energy transition: it is expected that by 2030 the installed capacity will not reach two thirds of what is required for a 1.5°C and net zero pathway (global carbon neutrality) set by 2050.

The onshore market added 72.5 GW worldwide, which is 18% less than the previous year, due to the slowdown in the two largest markets, China and the United States. Conversely, Europe, Latin America and Africa and the Middle East experimented record growth of 19%, 27% and 120%, respectively.

As for the offshore market, it experienced its best year in 2021, with 21.1 GW of installed power worldwide, approximately three times more than the previous year. New offshore installations account for 22.5% of new global wind installations. This brings the total offshore capacity to 57 GW, which represents 7% of the global wind capacity [2].

As far as Europe is concerned the total wind power capacity is 236 GW, 12% of which is offshore. Germany continues to have the largest installed capacity in Europe, followed by Spain, the UK, France, and Sweden. Figure 2 shows the growth in capacity over the period 2012-2021 in Europe. It is expected that 116 GW of new wind farms will be installed over the period from 2022-2026.

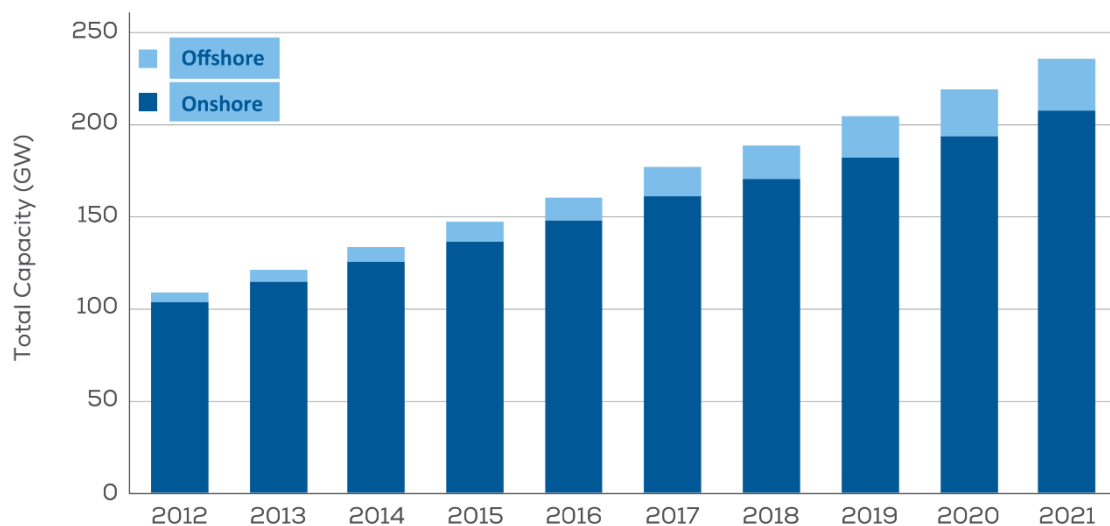


Figure 2. The growth of total wind energy capacity in Europe, 2012-21 [3]

On 2021, 17 GW were installed, which is not even half of what the EU should be building to be on track to deliver its 2030 Climate and Energy goals. 81% of the new installations were onshore, with the UK accounting for most of the new offshore wind installations (figure 3) [3].

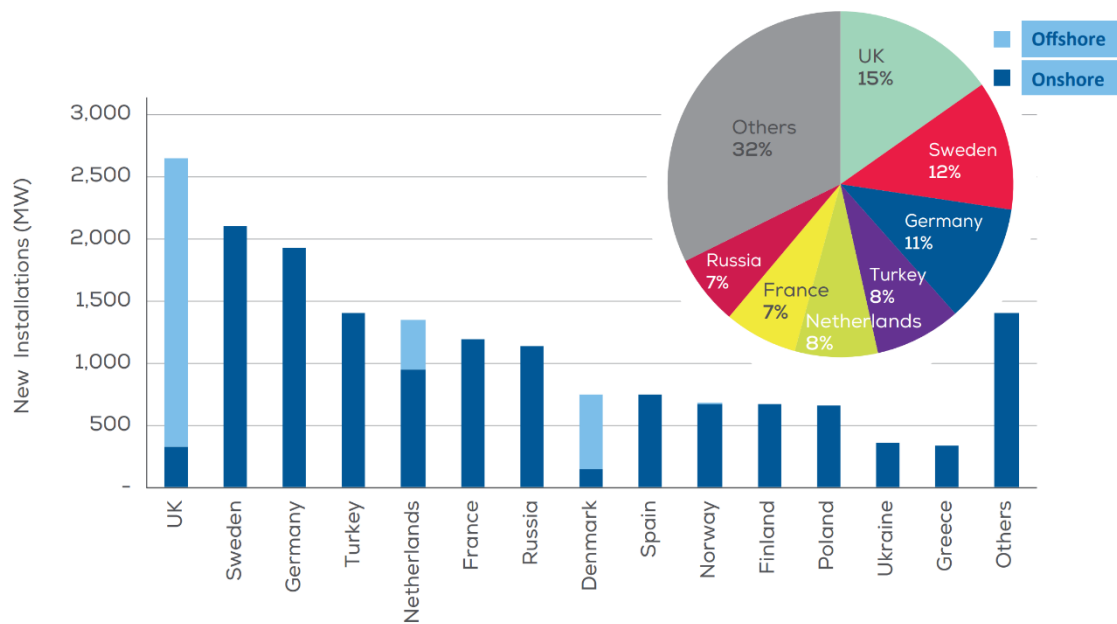
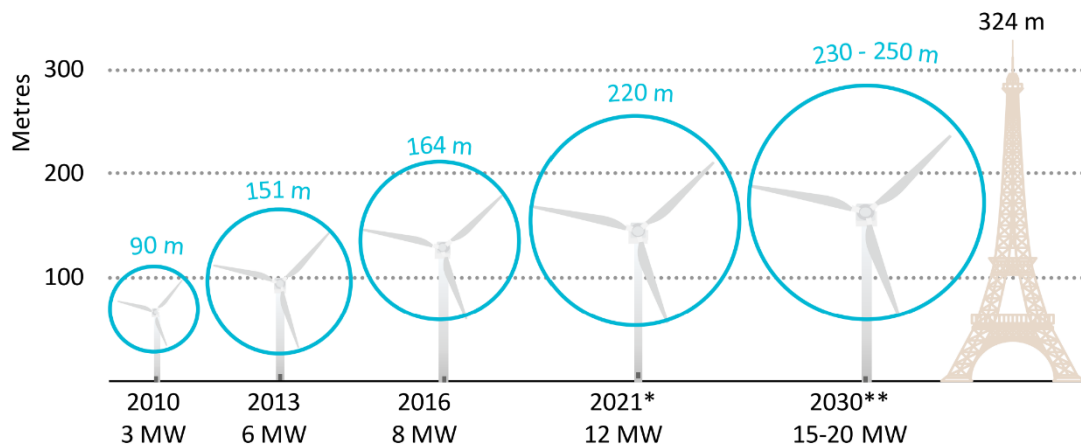


Figure 3. New wind installations in Europe in 2021 per country [3]

## 1.2. Offshore wind energy

Wind turbines can be onshore and offshore, each of them having its own advantages. In the first case, the advantages are mainly due to economic and logistical reasons: as they are cheaper and more accessible, they are easier to install, maintain and repair. On the other hand, offshore wind turbines have two major advantages: firstly, they allow higher capacity factors (the ratio between the energy generated over a period of time and the energy generated if the turbine had been operating at full load during the same period). The reason for this is that the offshore wind resource is of higher quality than onshore wind. As it is not disturbed by the orography and the irregularities of the terrain, the wind reaches higher speeds, which allow a greater extraction of energy by making bigger and taller wind turbines. Secondly, the installation of offshore wind farms significantly reduces the environmental impact, compared to a wind farm on land. The further from the coast, the lesser the impact.

The first offshore wind turbine was installed in Denmark in 1991. Since then, impressive advances have been made, both in terms of size and power. Development of new technologies and manufacturing systems have allowed the tip height to grow from 100 m in 2003 (3 MW turbine) to more than 200 m in 2016 (8 MW turbine), and the swept area to increase by 230%. Development is now focused on 15-20 MW turbines by 2030 (figure 4). The larger the size of the blades the larger the area swept by the turbine, allowing therefore to capture more wind and extract more energy. As will be seen in the next chapter, the International Energy Agency (IEA) 15-MW offshore reference wind turbine will be studied in this work, with a tip height of 270 m.



**Technology advances enabled offshore wind turbines to become much bigger in just a few years and are supporting ongoing increases in scale**

\* Announced expected year of commercial deployments. \*\* Further technology improvements through to 2030 could see bigger turbines sizes of 15-20 MW.

*Figure 4. Evolution of the largest commercially available wind turbines [4]*

Growth in the size of offshore wind turbines has meant a challenge for construction and foundations, in addition to higher capital costs. However, the operation and maintenance costs are reduced, which in the long run causes the levelized cost of energy (LCOE) to also decrease, making offshore energy more competitive.

Another important consequence in relation to larger turbines is the increase of the capacity factor. From 2010, when the average turbine size used in offshore wind farms was 3 MW, to 2018, when the average size was 5.5 MW, annual capacity factors increased from 38% to 43%. Current offshore wind turbines achieve capacity factors well over 50%. Given the same site conditions, a large turbine may have an increase in the capacity factor between 2% and 7%, compared to smaller turbines. However, the capacity factor depends on the quality of the wind and therefore the location, so not all new wind farm projects have to see higher capacity factors, although the trend is for it to continue growing as suggested by the data.

In fact, the average capacity factor is a great tool to reflect the quality of the wind resource for energy production, as it translates the wind speeds in a given area into the average performance over the course of a year. As can be seen from figure 5, wind is strongly affected by the geographical position, specifically the attitude. Wind resources are of higher quality near the poles, as pointed out by the IEA Offshore Wind Outlook 2019: “In Europe, the North Sea, Baltic Sea, Bay of Biscay, Irish Sea and Norwegian Sea, offshore wind has average annual capacity factors of around 45-65%, which is higher than the comparable figures for the United States (40-55%), China (35-45%), and Japan (35-45%). The capacity factor is also high in regions off the coast of South America and New Zealand (50-65%). Moderate wind speeds resources in India translate to a 30-40% average capacity factor. The average capacity factor in general is relatively low in regions nearer to the equator for example in Southeast Asia and parts of western Africa” [4].

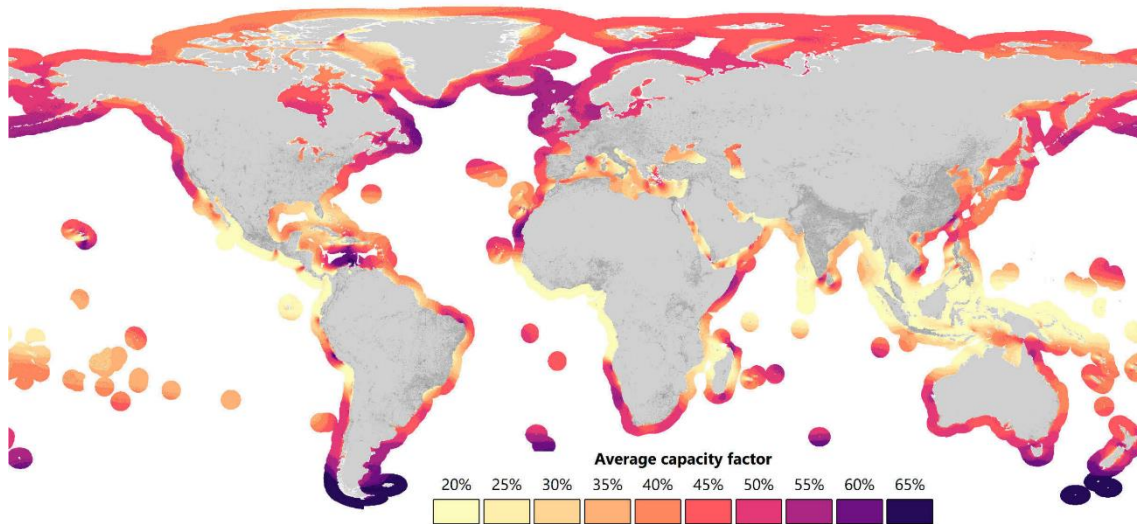


Figure 5. Average simulated capacity factors for offshore wind worldwide [4]

### 1.3. Floating offshore wind turbines

The downside of the offshore wind turbines is generally the cost and difficulty of installation and maintenance, as they are less accessible. As the distance from the coast increases, and with it, the depth of the seabed, bottom-fixed structures become more expensive.

It is estimated that 80% of the world's offshore wind resource potential lies in waters deeper than 60 m. However, at depths of 50 m or more, the cost of the fixed structure becomes prohibitively expensive: in particular, for many countries, bottom-fixed is not an option as their potential for fixed offshore wind is limited. Floating offshore wind turbines (FOWTs) are the solution if these countries want to exploit their wind resource.

The first FOWT was installed in 2009 in Norway. After its success, the offshore industry connected the world's first commercial floating offshore wind project, Equinor/Masdar's Hywind Scotland wind farm, which used 5 SGRE 6MW turbines, in the UK in 2017. The current largest floating offshore wind site is the 50 MW Kincardine project in Scotland which uses the Principal Power Windfloat platform and five Vestas V164-9.5 MW turbines [5].

As illustrated below, there are four dominant types of floating wind foundations in use or development. As will be seen in the next chapter, the study case of this work is the semi-submersible VoltturnUS-S Reference Platform, developed for the IEA Wind 15- MW Offshore Reference Wind Turbine.

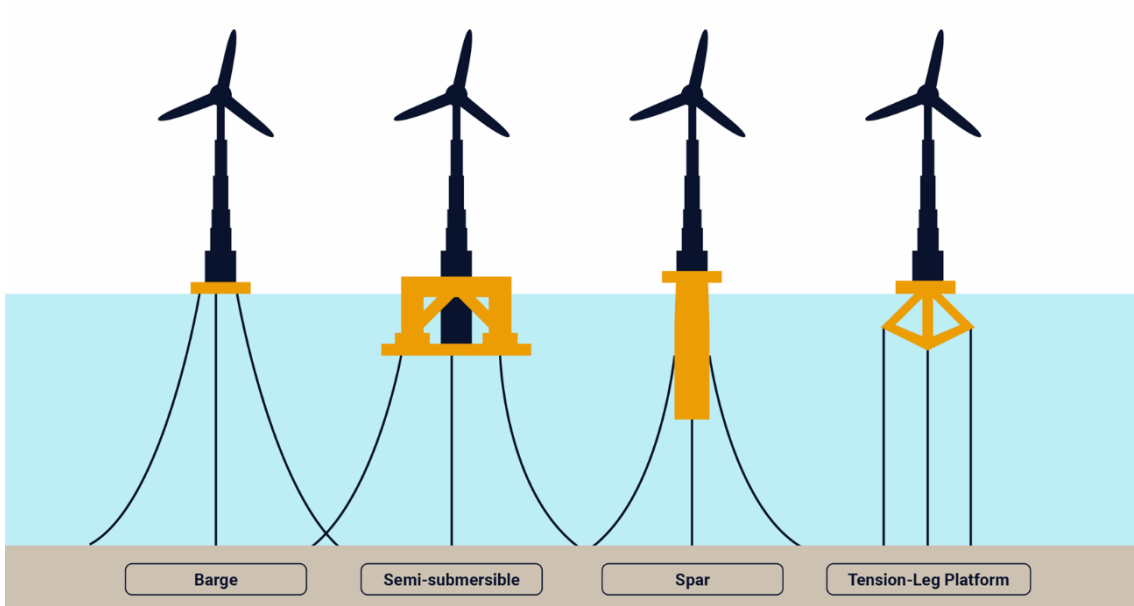


Figure 6. Floating offshore designs [6]

## 2. Fatigue theory

Initially, wind turbines design was conducted using static and quasi-static analyses. This type of analyses, at best, led to over-designed turbines, and at worst, led to premature failures. Soon it was discovered that wind turbines are fatigue critical machines, i.e., its design is dictated by fatigue behaviour. In the specific case of the blades, they are one of the most unique elements of wind turbines: they must satisfy criteria of minimum weight and cost, while ensuring that last a very high number of load cycles during their lifetime, which ranges from approximately 20 to 30 years. Turbine blades must withstand load cycles several orders of magnitude higher than those of an aircraft, as exemplified in figure 7. Composite materials have become the material of choice for blades after years of its study and design.

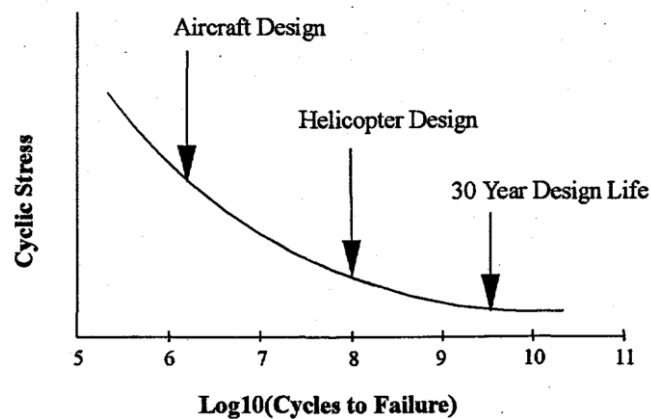


Figure 7. Schematic S-N diagram for different fatigue critical structures [7]

Fatigue can be defined as the structural response to cyclic loading. According to the ASTM E206 standard, "Fatigue is a permanent, progressive and localized phenomenon related to a structural change in a material undergoing stresses and strains changing in time, which can lead to crack nucleation and / or fracture after an adequate number of cycles". [8]

Thus, the repeated application of a load can lead to failure even if the maximum load is lower than the static resistance of the material. Other factors can affect fatigue life: high temperatures can lower material properties; while oxidation, wear, corrosion and friction can help the nucleation of the cracks. The fatigue failure is characterised by several stages:

- Crack nucleation due to applied stresses
- Crack propagation along a plane different from the crack nucleation and perpendicular to the stress direction
- Failure of the material due to the cross-section reduction, no more enough to bear the maximum load

The crack nucleation happens in elastic stress regime, around a surface defect which acts as a stress intensification zone. Every time the stress cycles the crack propagates a defined quantity, which leads to a decrease in the resisting cross section and consequently to an increase in the maximum stress.

Every time the crack opens and closes it pushes the surface asperities, giving the crack surface a smooth look. This propagation takes place until the cross section is so small that the stress

reaches the elastic limit and the residual resisting cross section fails due to a static failure mechanism.

Fatigue fracture surfaces have a typical appearance: firstly, there is no plastic strain present around the failure zone. This is because the failure mechanism is related to microstructural changes and not to plastic strain. On the other hand, the failure surface is recognizable for having different smooth and rough areas. The smooth appearance areas are caused by the gradual fatigue failure and the slow crack propagation resulting in the so-called “sand lines”. The rough appearance areas are caused by the sudden static failure, that is, the sudden crack propagation.

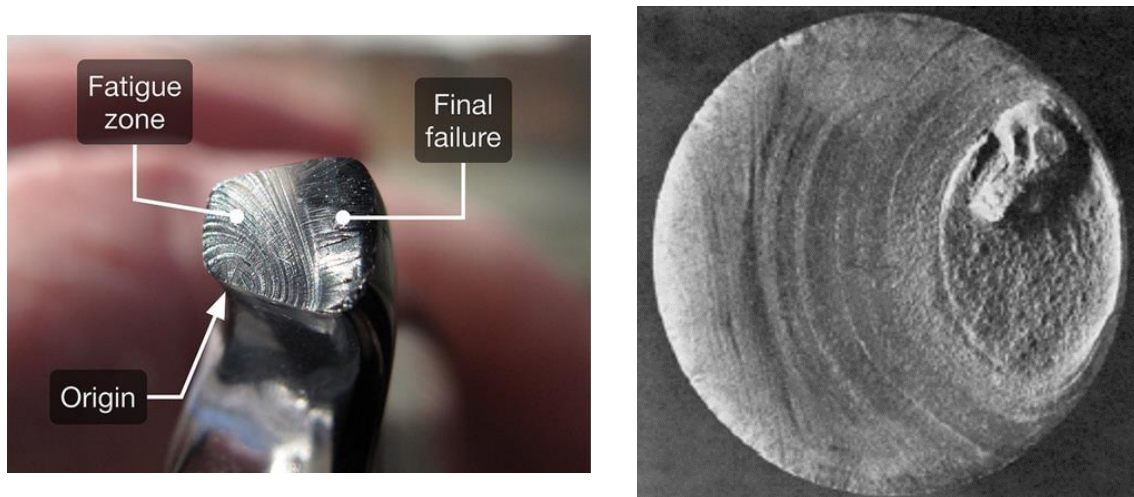


Figure 8. Fatigue failure [9], [10]

Generally, a distinction is made between high and low cycle fatigue. On high cycle fatigue the loads are lower than the elastic limit and no plastic strains appear. Normally, it is referred to when 100.000 load cycles are exceeded. On the other hand, the low cycle fatigue is when the loads applied are larger than the elastic limit and plastic deformation occurs, and it is referred to when less than 100.000 load cycles are reached. All fatigue considerations in this work refer to high cycle fatigue, as wind turbine components are subjected to a very high number of load cycles: the rotation of the rotor, aerodynamic turbulence, and other factors cause up to  $10^9$  load alternations in the typical 20-year lifetime of a turbine. [11]

## 2.1. Fatigue parameters

To analyse the fatigue parameters, it is useful to consider a cyclic load applied in a fatigue test. The stress in whatever point of the structure has a time dependency which can be expressed as a function:

$$\sigma(t) = \sigma_m + \sigma_a \sin(wt)$$

Where:

- $\sigma_m$  is the mean stress
- $\sigma_a$  is the alternate stress
- $w$  is the pulsation

Generally,  $\sigma_m$  and  $\sigma_a$  are not constant. In simple cases they are constant values, as represented in figure 9:

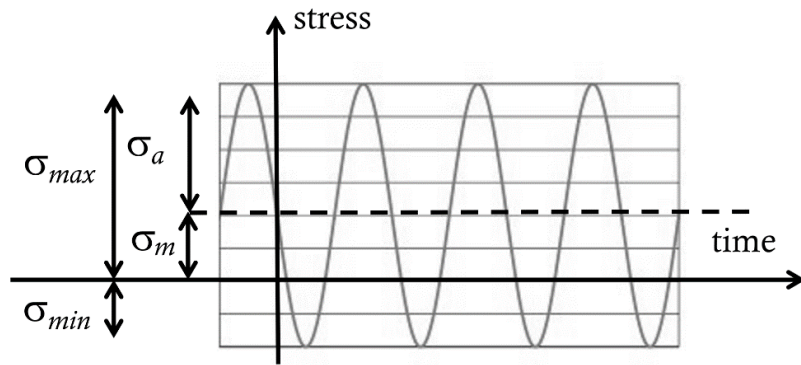


Figure 9. Characterization of a cyclic load [10]

Where  $\sigma_{max}$  and  $\sigma_{min}$  are the maximum and minimum stress in the cycle, respectively. The relation between the alternate, mean, minimum and maximum stress is given by:

$$\sigma_m = \frac{\sigma_{max} + \sigma_{min}}{2}$$

$$\sigma_a = \frac{\sigma_{max} - \sigma_{min}}{2}$$

Other parameters used to describe the fatigue loading are:

- The stress range ( $\Delta\sigma$ ), given by:

$$\Delta\sigma = 2\sigma_a$$

- The stress ratio (R), which is, by definition, the ratio between the minimum and maximum stress:

$$R = \frac{\sigma_{min}}{\sigma_{max}}$$

The stress ratio is a useful parameter to characterize the loads. A typical value for the fatigue test and curves is  $R = -1$ , which means that the load is symmetric and alternate with no mean stress ( $\sigma_m = 0$ ). Different cases of stress ratio are illustrated in figure 10.

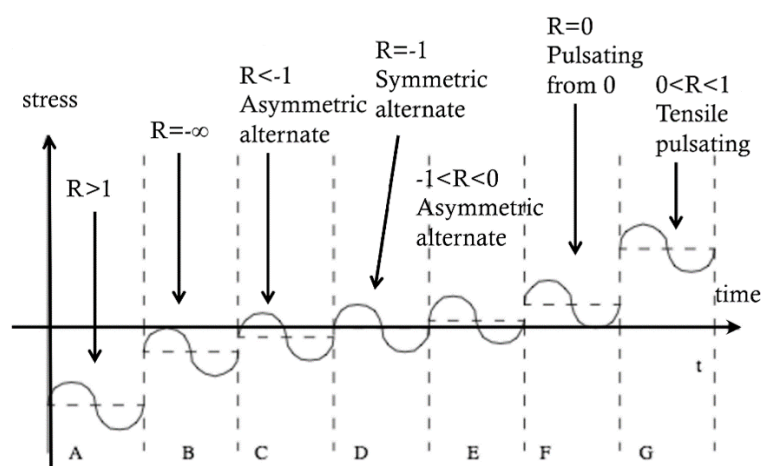


Figure 10. Different stress ratios [10]

## 2.2. S-N curve

Standard tests are defined to describe fatigue behaviour and find the fatigue limit. Different material specimens are tested under cyclic sinusoidal loading with a constant mean value. The number of cycles to failure ( $N$ ) and the alternate stress ( $\sigma_a$ ) are recorded in a diagram known as the Wohler diagram (also S-N curve, in which a stress  $S$  level is required to fail the sample). A threshold number of cycles is set to interrupt the test if specimens do not break, assigning therefore a fatigue limit to the material. Data in this diagrams are normally quite scattered. An example of S-N curve is shown in figure 11.

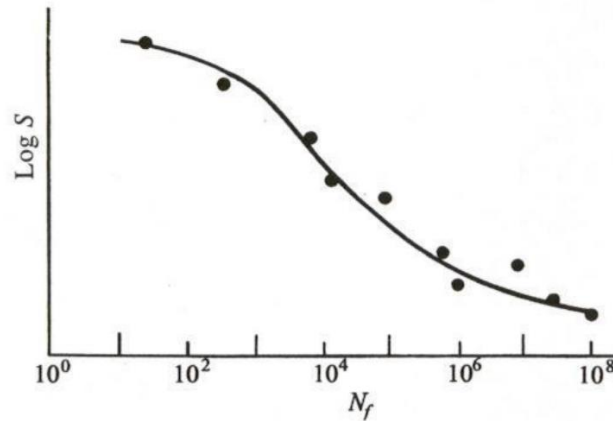


Figure 11. S-N curve [12]

The S-N behaviour of composite materials at constant R value is typically fit using one of two equations [7]. The first is a power law of the form:

$$\sigma = CN^{-1/m}$$

or alternately,

$$\log(\sigma) = \log(C) - \frac{1}{m} \log(N)$$

where:

- $N$  is the number of cycles to failure at a stress level  $\sigma$
- $C$  is a constant
- $m$  is the fatigue exponent (slope of the S-N curve)

In nondimensional form, the equation takes the form:

$$\frac{\sigma}{\sigma_0} = C'N^{-1/m}$$

or

$$\log\left(\frac{\sigma}{\sigma_0}\right) = \log(C') - \frac{1}{m} \log(N)$$

where:

- $\sigma_0$  is the static strength of the composite
- $C'$  has a value of 1 when the curve fit to the S-N data set passes through the static strength at 10<sup>0</sup> cycles (at static failure in the first fatigue cycle)

The second form is given by a logarithmic-linear function of the form:

$$\sigma = C - \frac{1}{m} \log(N) = C - b \log(N)$$

or alternately,

$$10^\sigma = CN^{-1/m}$$

Where the inverse of  $m$  is typically denoted by  $b$ . In nondimensional form, the equation takes the following form:

$$\frac{\sigma}{\sigma_0} = C' - \frac{1}{m} \log(N) = C' - b \log(N)$$

Where  $C'$  also has a value of 1 when the curve fit to the S-N data set passes through the static strength at  $10^0$  cycles. Figure 12 shows the S-N curve for a typical fiberglass composite (material wind turbine blades are based on).

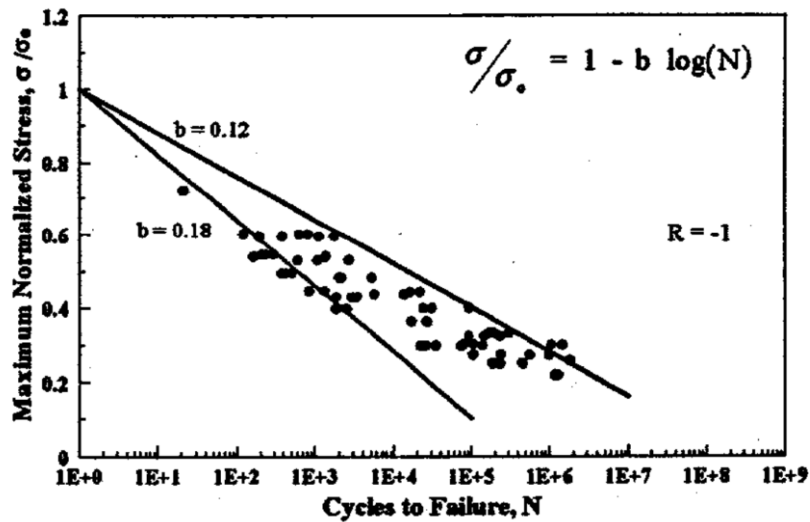


Figure 12. Normalized S-N for a typical fiberglass composite,  $R=-1$  [7]

### 2.3. Constant life diagrams

Most of the S-N curves are done based on tension compression tests with no mean stress ( $R = -1$ ). To take account the effects of the mean stress it is common to use a constant-life Goodman Diagram, which represents the locus of all stress states that produce a given fatigue failure. These curves allow to determine the effect on lifetime changes in the stress on the component studied. A typical Goodman diagram is illustrated in figure 13.

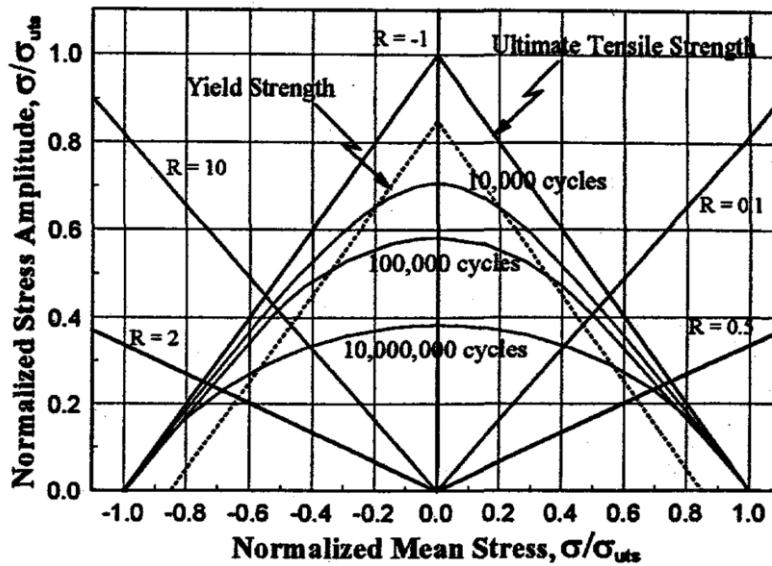


Figure 13. Typical symmetric Goodman Diagram [7]

In the vertical axis the alternate stress is represented (in this case, normalized by the ultimate tensile strength). The horizontal axis measures the mean stress (again, normalized). It can be seen that a constant R ratio plots as a straight line in the diagram. On the other side, the constant life curves, bounded by the ultimate tensile strength (and ultimate compressive strength as this case is symmetric), are plotted based on a family of S-N curves. Different constant-life curve can be plotted: straight lines (simpler, but less accurate), straight-lines segmented, or curves. Figure 14 shows different constant-life curves:

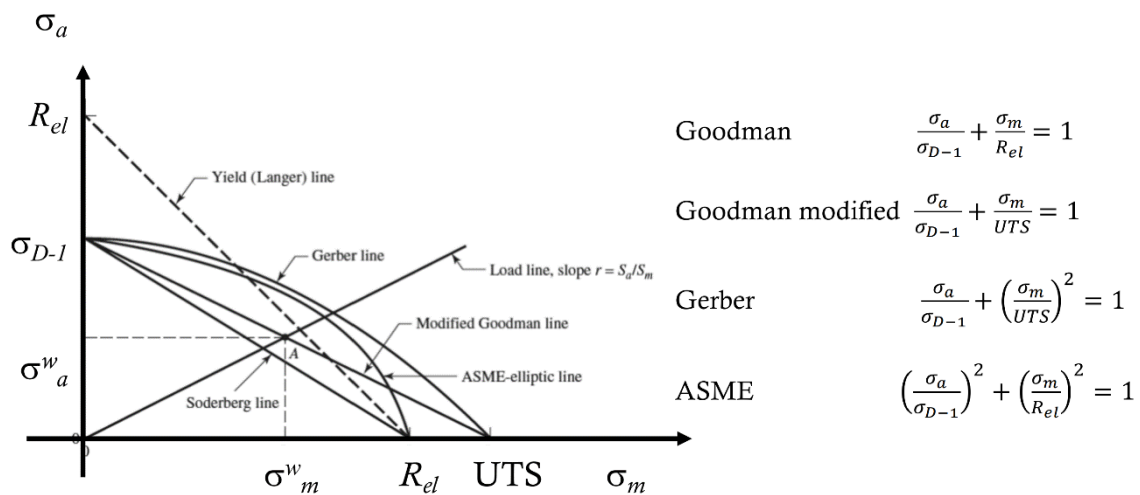


Figure 14. Different Goodman curves [10]

### 3. System description

The case study of this work is focused on the FOWT given by the IEA 15-MW Offshore Reference Wind Turbine supported by the VoltturnUS-S Semisubmersible Reference Platform.

On July 2020, the IEA published the technical report “Definition of the IEA Wind 15-Megawatt Offshore Reference Wind Turbine” [13], as an addendum to IEA Wind Task 37 on Wind Energy Systems Engineering. The report documents the design and performance of the IEA Wind 15-MW reference wind turbine, jointly developed by the National Renewable Energy Laboratory (NREL), Technical University of Denmark (DTU), and the University of Maine (UMaine).

After it, another following technical report was published, regarding the semisubmersible floating platform: “Definition of the UMaine VoltturnUS-S Reference Platform Developed for the IEA Wind 15- Megawatt Offshore Reference Wind Turbine” [14].

The reference floating offshore wind turbine, which is the case study of this work, comprises a floating semisubmersible platform, a chain catenary mooring system, a floating-specific tower, and a rotor-nacelle assembly.

Both the IEA 15-MW offshore reference wind turbine and the VoltturnUS-S reference platform are presented below, with special regard to the turbine blades, which is where the fatigue analysis will be conducted.



*Figure 15. IEA-15-240 RWT and VoltturnUS-S reference platform [13]*

### 3.1. IEA 15-MW Offshore Reference Wind Turbine

The 15 MW offshore reference turbine has a conventional three-bladed upwind design with a rotor diameter of 240 m; a 150-m hub height; a variable-speed, collective pitch controller; and a low-speed, direct-drive generator. The overall parameters of the turbine are shown in the table 1.

Table 1. Key Parameters for the IEA Wind 15-MW Turbine [13]

Parameter	Units	Value
Power rating	MW	15
Turbine class	-	IEC Class 1B
Specific rating	W/m <sup>2</sup>	332
Rotor orientation	-	Upwind
Number of blades	-	3
Control	-	Variable speed Collective pitch
Cut-in wind speed	m/s	3
Rated wind speed	m/s	10.59
Cut-out wind speed	m/s	25
Design tip-speed ratio	-	9.0
Minimum rotor speed	rpm	5.0
Maximum rotor speed	rpm	7.56
Maximum tip speed	m/s	95
Rotor diameter	m	240
Airfoil series	-	FFA-W3
Hub height	m	150
Hub diameter	m	7.94
Hub overhang	m	11.35
Rotor precone angle	deg	-4.0
Blade prebend	m	4
Blade mass	t	65
Drivetrain	-	Direct drive
Shaft tilt angle	deg	6
Rotor nacelle assembly mass	t	1,017
deg - degrees	rpm - Revolutions per minute	
m - meters	t – tons	
m/s – meters per second	W/m <sup>2</sup> – watts per square meter	

### 3.2. Blades

The blade length is 117 m, with a total weight of 65 t. The root diameter is 5.2 m and its maximum chord (5.77 m) is located at approximately 20% span. The most important blade properties are shown in table 2.

Table 2. Blade Properties [13]

Description	Value	Units
Blade length	117	m
Root diameter	5.20	m
Root cylinder length	2.34	m
Max chord	5.77	m
Max chord spanwise position	27.2	m
Tip prebend	4.00	m
Precone	4.00	deg
Blade mass	65,250	kg
Blade center of mass	26.8	m
Design tip-speed ratio	9.00	-
First flapwise natural frequency	0.555	Hz
First edgewise natural frequency	0.642	Hz
Design $C_p$	0.489	-
Design CT	0.799	-

deg - degrees  
m – meters

kg - kilograms  
Hz – Hertz

### 3.2.1. Blade aerodynamic properties

The blade is designed based on the DTU FFA-W3 series of airfoils, which are shown in figure 16.

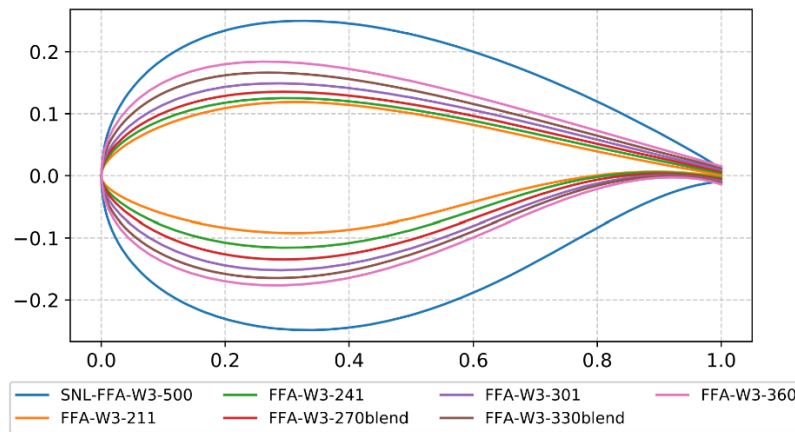


Figure 16. DTU FFA-W3 airfoil family used in the IEA Wind 15-MW blade design [13]

The shape of the blade changes from the cylinder cross section at the blade root to the airfoil shape between the 2%–15% of span, and the maximum chord of 5.77 m is given at 27.2 m of span (23.3%). It is worth mentioning that due to the huge blade radius, the blade is designed with a significant prebend away from the tower to provide additional tip clearance, with 4 m separating the tip chord line from the root.

### 3.2.2. Blade structural properties

The structural layout of the blade is composed of (figure 17):

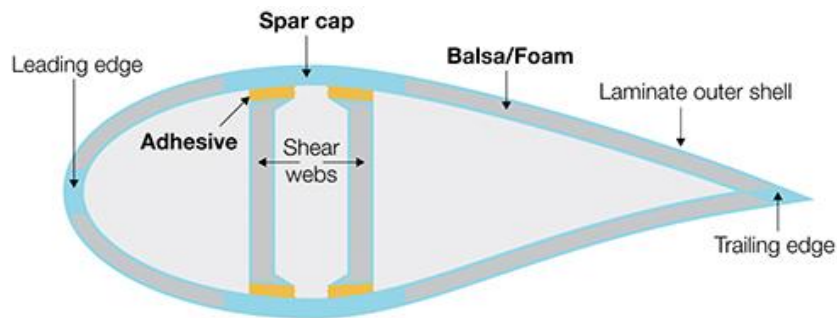


Figure 17. Blade internal structure scheme [15]

- Spar caps: There are two of them, located in the pressure and suction side of the airfoil. As they carry the main loads of the blade, they are made of carbon fiber, to provide as much stiffness with as little weight as possible.
- Trailing and leading edges reinforcement made of uniaxial glass fiber to provide additional edgewise stiffness.
- Shear webs: Two of them connect the pressure side and suction side, attached to the main spars, extending from a 10% to 95% span.
- Foam filler panels: located between the leading-edge and trailing-edge reinforcement and the spar caps, on both the pressure side and suction side.

The figure 18 shows the internal structure of the blade for different cross sections along the span. Change on the shape from the cylindrical cross section to the different airfoils can be noticed.

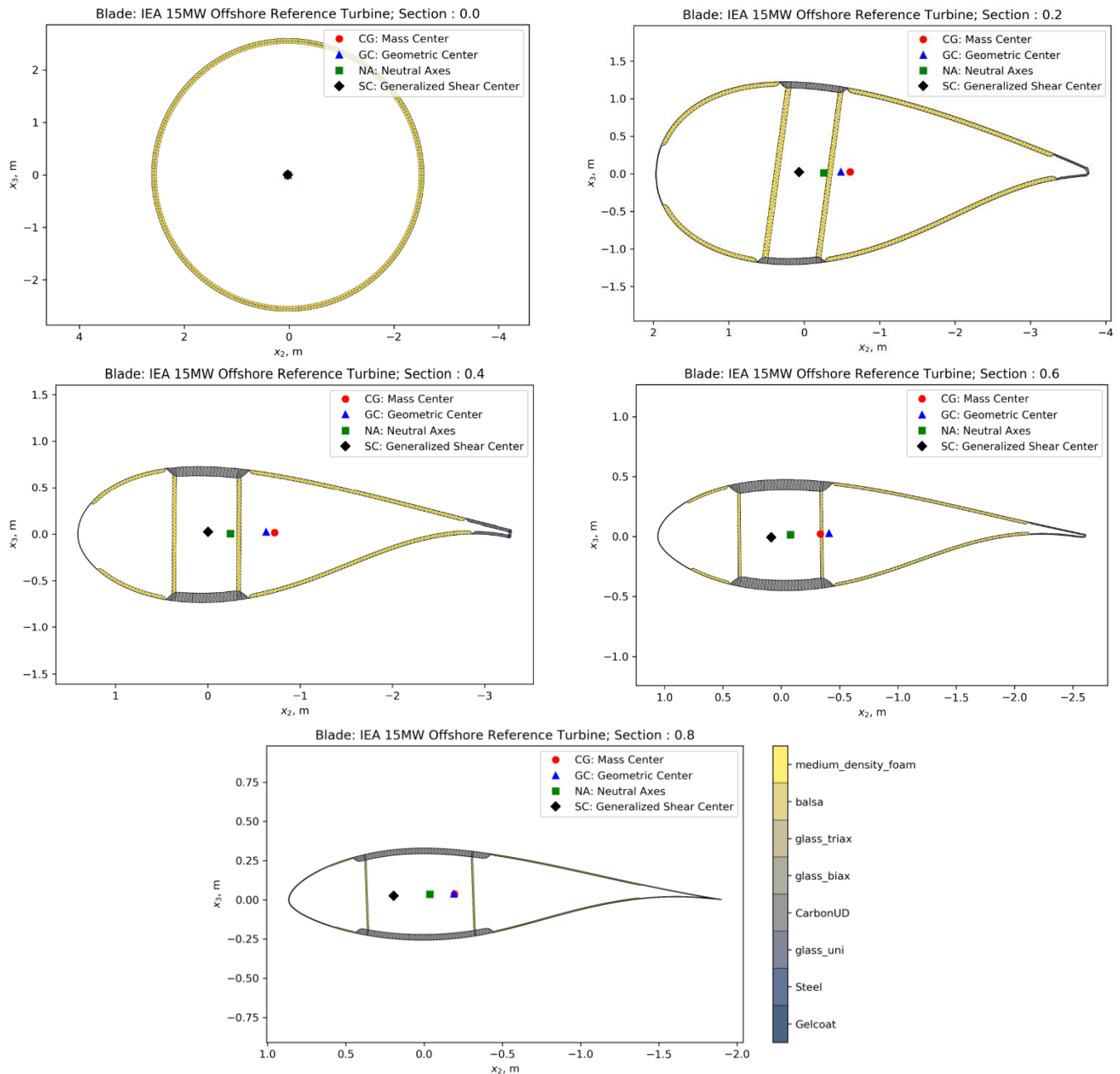


Figure 18. Blade cross sections at different spans [13]

### 3.3. VoltornUS-S Reference Platform

The semisubmersible platform is designed to support the IEA-15-MW wind turbine and comprises a four-column (three-radial and one central) steel attached to the seabed by means of a three-line chain catenary mooring system with a vertical pretension of 6,065 kN.

The tower is specifically designed for the flotation application: floating offshore wind turbine towers have higher stiffness requirements than fixed-bottom configurations because of the increased inertial and gravity loads resulting from platform motion. The design in this case is an isotropic steel tube weighting 1,263 tons.

The platform has a draft of 20 m with a 15-m freeboard to the upper deck of the columns and displaces 20,206 cubic meters of seawater. Figure 19 shows a representation of the whole assembly.

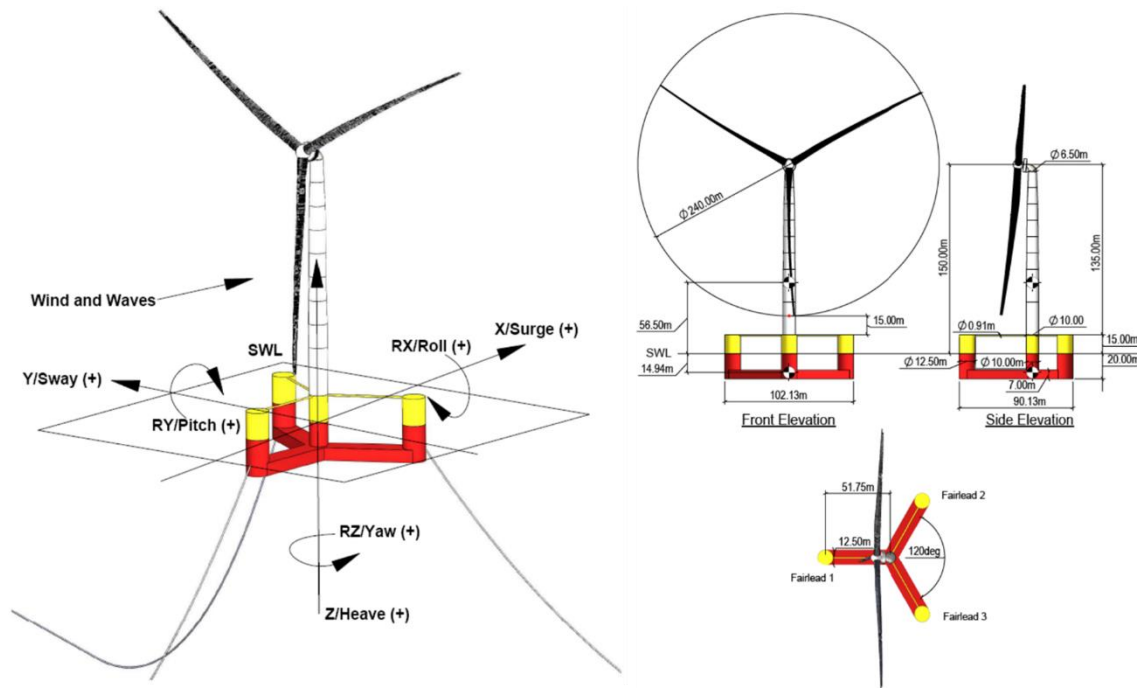


Figure 19. Platform view (left) and top-side view (right) [14]

### 3.4. Controller

The control system of the wind turbine is managed by the ROSCO controller [27] (Reference Open-Source COntroller for fixed and floating offshore wind turbines), developed by the Delft University of Technology. While common controllers are developed for specific turbines and are difficult to modify for use on other turbines, this controller has been developed to provide a reference from which also non-control engineers can deal with.

The objective of the controller is to maximize power modifying three control parameters: the orientation of the rotor (yaw system), the orientation of the blades (pitch system) and the torque generated. This is achieved by two methods of actuation: to control the generator power a variable-speed generator torque controller is used; to regulate rotor speed a collective blade pitch controller is used.

The behaviour of the control system can be divided in four regions, as shown in figure 20:

- Region 1: corresponds to below cut-in wind speed conditions. In this region, wind speed is too low to produce power and the generator torque is set to zero to allow the wind to accelerate the rotor for start-up.
- Region 2: corresponds to below rated conditions. In this region, the objective is the maximum extraction of the wind energy.
- Region 3: corresponds to above rated conditions. In this region, the power is saturated to not damage the components.

- Region 4: corresponds to above cut-out wind speed conditions. In this region, turbine must be turned off because wind speed is too strong. Blades are pitched to reduce thrust force to zero (feathering).

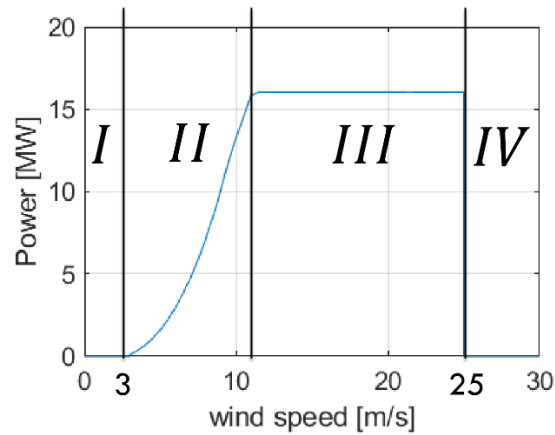


Figure 20. Controller zones [28]

Both generator torque and blade pitch controllers are PI controllers. Both modules vary according to the conditions in which the system is. This two modules plus some additional control modules are briefly discussed below.

### 3.4.1. Generator Torque Controller and blade pitch controller

For the generator torque controller, four different generator torque controllers are available: two methods for below wind speed operations and two methods for above wind speed conditions.

Regarding below rated operations, one of the options to maximize extracted power at each wind condition is to follow a quadratic law of generator torque with respect to rotor angular speed. Alternatively, a tip speed ratio tracking to maintain tip speed ratio (TSR) at its optimal value can be adopted, for which the wind speed can be measured or estimated accurately.

Regarding the two existing methods for above rated conditions, first of them considers a constant generator torque, while the second strategy considers a constant extracted power equal to its rated value.

As for the blade pitch controller, its main goal is to keep the rotor angular speed at its rated value.

### 3.4.2. Additional Control Modules

In addition to the main modules, ROSCO incorporates some additional modules to improve its performance:

- Wind speed estimator: This module estimates wind speed used for TSR tracking in the generator torque controller
- Set Point Smoothing: Near rated operations the generator torque and blade pitch controllers normally conflict due to incompatible reference rotor speed. This module

shifts the speed reference signal of the inactive controller while the active one works to avoid this problem.

- Minimum pitch Saturation: Near rated condition thrust force reaches its highest values, since below rated wind speed is lower and above rated condition blade pitching reduces that force. In order to limit the loads, this module defines a minimum value of blade pitch angle which will be used as a saturation limit during control operations.
- Floating offshore wind turbine feedback: This module introduces a new term in the PI blade pitch controller, with the aim of finding a gains' value that reduces rotor angular acceleration to increase the average extracted power and stabilize the structure.

## 4. Methodology

The objective of this work is to perform a fatigue analysis on the blades of the IEA 15 MW offshore reference wind turbine, supported by the semisubmersible structure platform, under realistic load cases. A brief explanation of the methodology that will be followed in the next chapters is given here:

Firstly, aeroelastic simulations are carried out under specific cases of external conditions (wind speeds and sea states) to obtain the internal forces of the blade. Different cross sections of the blade are selected to retrieve the internal cross-sectional forces and moments.

Then, using a postprocessor, each section is divided in multiple elements, in which the resulting stresses due to the state of loading are calculated. For each of these elements the fatigue analysis is carried out, where the equivalent damage accumulated after the load cycles is calculated. The accumulated damage is used to estimate the life of the material, which allows to understand the behaviour of the blade under the effects of fatigue and even to vary the design of the blade to obtain a better response.

These steps will be further explained in the next chapters. Figure 21 represents a schematic description of the workflow followed for structural blade analysis.

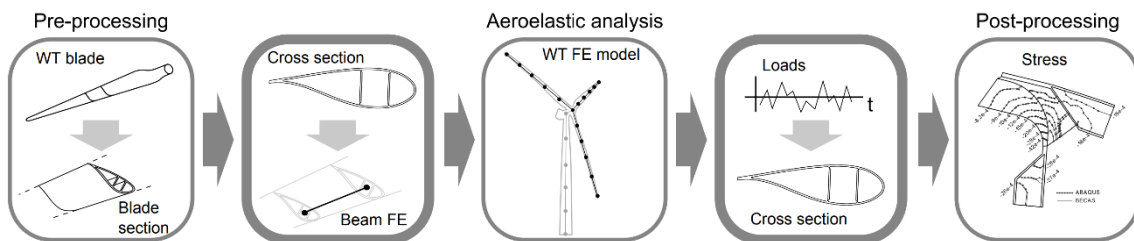


Figure 21. Schematic description of the workflow for structural analysis of the wind turbine blades [16]

Starting from the geometrical model of the blade, a pre-processing phase is necessary to generate the beam finite elements representing the blade in the aeroelastic analysis. To do so, a series of cross sections along the blade are analysed and its geometry and properties are retrieved (figure 22). The resulting is a beam finite elements model which is used to represent the blades in the wind turbine assembly inside the aeroelastic analysis tool. Finally, based on the cross-section forces and moments resulting from the aeroelastic simulations it is possible to recover the detailed three-dimensional stress components, which are used to perform the fatigue analysis.

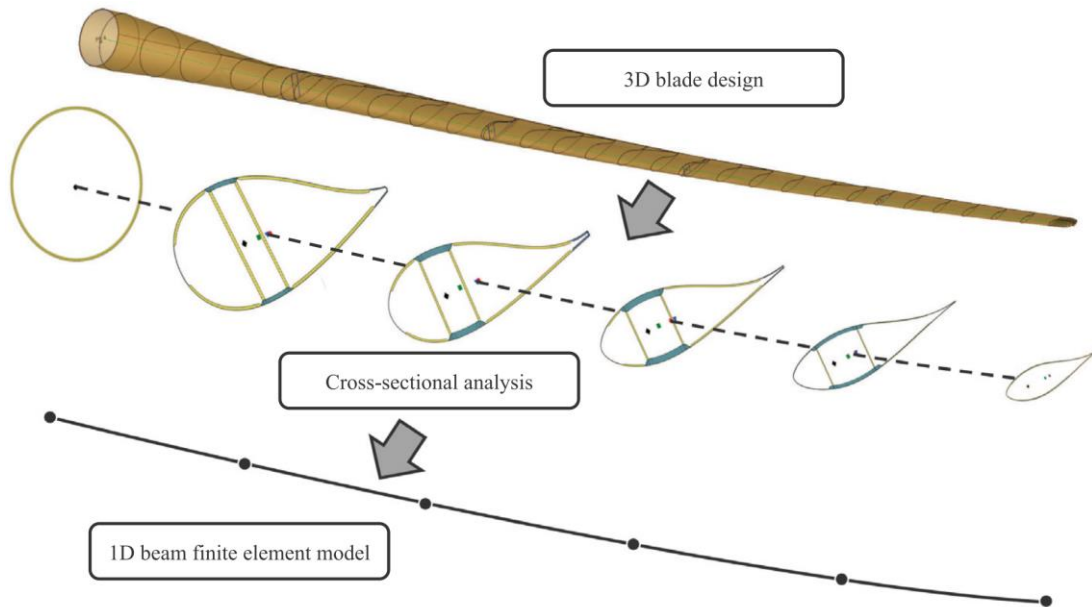


Figure 22. Methodology to account for 3D structural designs in 1D beam finite element models [17]

This work covers the aeroelastic analysis and the post-processing of the results do the fatigue analysis, as the first stages (design of the blade and pre-processing) are already defined. The geometry, materials and internal structure of the blade are already known, and the work of the pre-processor is mainly to compute, based on these quantities, the cross-section stiffness and mass properties, which are then used in the aeroelastic analysis. The developers used SONATA (Structural Optimization and Aeroelastic Analysis) [17], as the pre-processor.

For the aeroelastic analysis, Beamdyn [18] is used to get the internal forces and moments of the cross sections. It works as a module inside OpenFAST [19].

For the Post-processing, BECAS (BEam Cross section Analysis Software) [20] was used. BECAS, a finite element based cross section analysis tool, is a group of Matlab functions used for the analysis of beam cross sections. It can be used either as a pre-processor, that is, for the generation of beam finite element models in cross sections of arbitrary geometry; or as a post-processor, to perform a stress and strain recovery of the cross-section elements, as it is used in this work.

Wind turbine aeroelastic codes are commonly based on beam theory, as is the case for both BeamDyn and BECAS, which allow for an accurate yet computationally inexpensive representation of a general class of three-dimensional beam-like structures. The development of beam models which accurately describe the behaviour of the blades is challenging, as modern wind turbine blades feature complex geometry and a mix of different anisotropic materials. Although 3D finite element models (shell or solid models) provide accurate results, they are computationally expensive. On the other hand, beam models achieve a great level of accuracy while being more computationally efficient (figure 23).

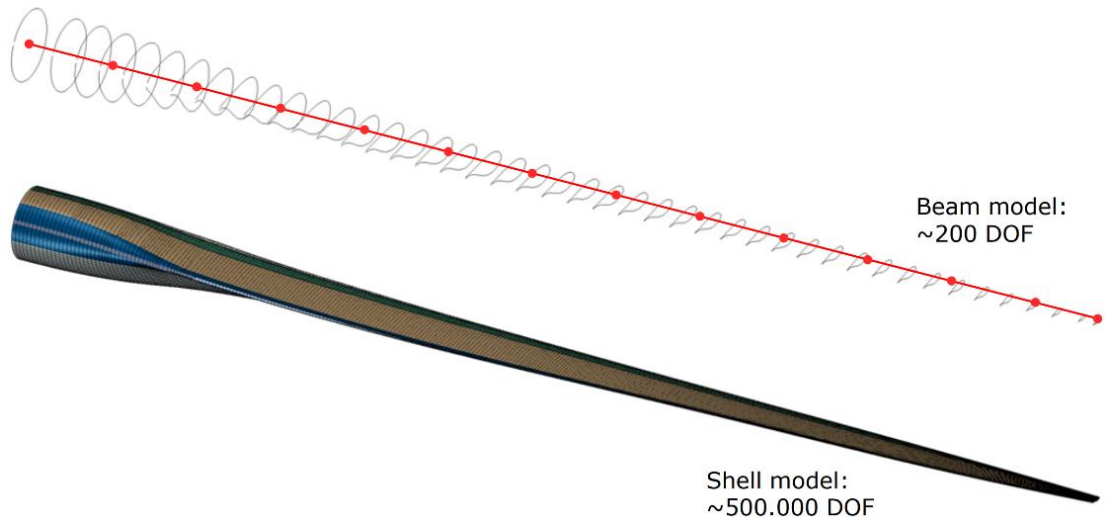


Figure 23. Beam model (up) and shell model (down) of a wind turbine blade [16]

# 5. Aeroelastic simulations

## 5.1. Understanding BeamDyn

The objective of the simulations is to retrieve the internal forces and moments of the blade under a realistic set of load cases. Also, the deflection of the blade will be analysed to better understand its behaviour. To do so, BeamDyn is used coupled into OpenFAST as the software for the aeroelastic simulations. These tools allow to simulate the wind turbine in a dynamic time-domain scenario. OpenFAST (previously called FAST v8) is a computer-aided engineering tool for simulating the coupled dynamic response of wind turbines. It joins:

- Aerodynamics models, using wind-inflow data to compute the blade aerodynamic loads (AeroDyn module)
- Hydrodynamics models, which simulate the incident waves (HydroDyn module)
- Control and electrical system dynamics models, to simulate the controller logic
- Structural dynamics models, which simulate the elasticity of the blades and support structure applying the aerodynamic, hydrodynamic and gravitational loads (BeamDyn and ElastoDyn modules)

There are modules to account also for the mooring system (MoorDyn), the tower and structure motion (ElastoDyn) and wind distributions generation (Turbsim). The coupling between all models is achieved through a glue code.

BeamDyn is based in the geometrically exact beam theory (GEBT), which supports full geometric nonlinearity and large deflection (with bending, torsion, shear, and extensional degree-of-freedom), anisotropic composite material couplings and a reference axis that permits blades that are not straight, as it is the case of the 15 MW wind turbine blade. Figure 24 represents the workflow of BeamDyn when coupled with OpenFAST (BeamDyn can also work in a stand-alone version which will not be dealt with in this work).

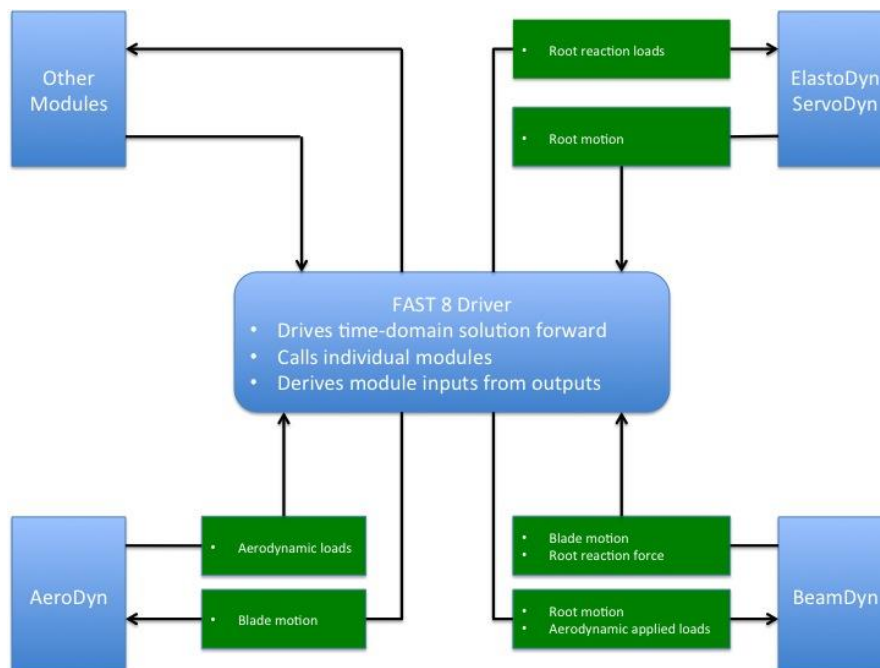


Figure 24. Coupled interaction between BeamDyn and FAST [21]

Loads are transferred between the different modules. From other modules, BeamDyn receives:

- The blade root node displacements (three translations and three rotations)
- The blade root node velocities (three translational and three rotational)
- The blade root node accelerations (three translational and three rotational)

With this variables, BeamDyn computes:

- The six reaction forces at the root (three forces and three moments)
- The blade displacements, velocities, and accelerations along the beam length

These displacements are then used in AeroDyn to compute the aerodynamic loads distributed along the length of the blade, which are used in turn as input to BeamDyn to calculate the internal reaction loads of the blade.

The output values can be requested by the user at a maximum of nine nodes among the quadrature points (QPs), which are the points that BeamDyn uses internally to perform the calculations and derive from the finite element nodes (FE nodes). These points range from the blade root to the blade tip.

## 5.2. Input files

Two input files are used as input to BeamDyn to perform the simulations, which are explained here.

### 5.2.1. Primary input file

Named “IEA-15-240-RWT\_BeamDyn”, in this file the blade geometry is defined through a set of key-point (kp) coordinates and initial twist angles. Each key point is defined by three physical coordinates (“kp\_xr”, “kp\_yr” and “kp\_zr”) in the IEC standard blade coordinate system, where  $Z_r$  is along blade axis from root to tip,  $X_r$  directs normally toward the suction side, and  $Y_r$  directs normally toward the trailing edge. The blade reference coordinate system is represented in figure 25.

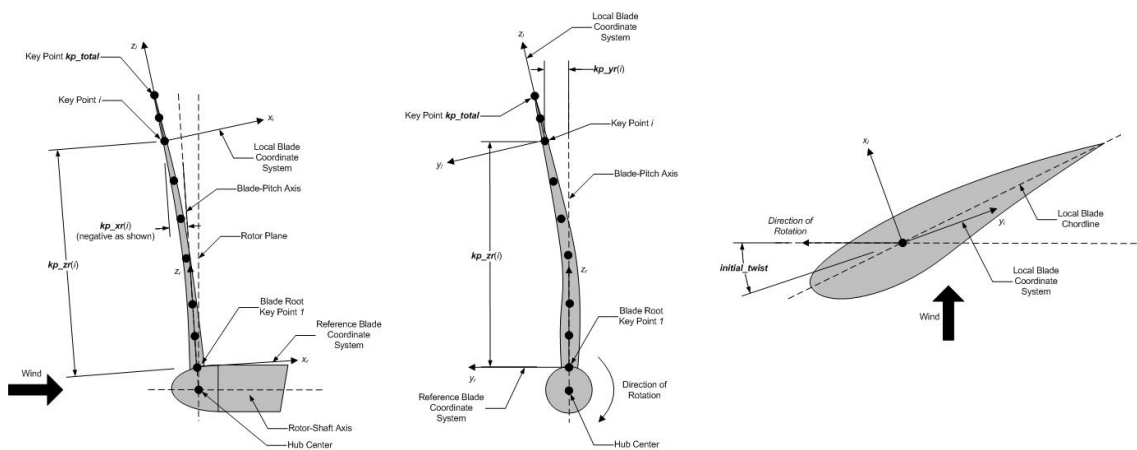


Figure 25. BeamDyn Blade Geometry - Top: Side View; Middle: Front View (Looking Downwind); Bottom: Cross Section View (Looking Toward the Tip, from the Root) [21]

For each key point, a structural twist angle (“initial\_twist” variable) is given. The structural twist angle is also following the IEC standard which is defined as the twist about the negative  $Z_i$  axis.

A total of 50 key points are used to define the geometry of the blade of the 15 MW wind turbine. Table 3 shows the key points and their respective initial twists.

*Table 3. Key points defining the blade geometry in the Reference Blade Coordinate system*

<b>kp_xr (m)</b>	<b>kp_yr (m)</b>	<b>kp_zr (m)</b>	<b>Initial twist (deg)</b>
0.00E+00	0.00E+00	0.00E+00	1.56E+01
1.84E-02	0.00E+00	2.39E+00	1.56E+01
4.43E-02	0.00E+00	4.78E+00	1.53E+01
7.04E-02	0.00E+00	7.16E+00	1.49E+01
1.03E-01	0.00E+00	9.55E+00	1.42E+01
1.35E-01	0.00E+00	1.19E+01	1.34E+01
1.65E-01	0.00E+00	1.43E+01	1.23E+01
1.95E-01	0.00E+00	1.67E+01	1.13E+01
2.19E-01	0.00E+00	1.91E+01	1.03E+01
2.39E-01	0.00E+00	2.15E+01	9.37E+00
2.47E-01	0.00E+00	2.39E+01	8.57E+00
2.50E-01	0.00E+00	2.63E+01	7.85E+00
2.49E-01	0.00E+00	2.87E+01	7.19E+00
2.47E-01	0.00E+00	3.10E+01	6.56E+00
2.45E-01	0.00E+00	3.34E+01	5.93E+00
2.41E-01	0.00E+00	3.58E+01	5.36E+00
2.37E-01	0.00E+00	3.82E+01	4.80E+00
2.32E-01	0.00E+00	4.06E+01	4.31E+00
2.25E-01	0.00E+00	4.30E+01	3.84E+00
2.09E-01	0.00E+00	4.54E+01	3.45E+00
1.86E-01	0.00E+00	4.78E+01	3.08E+00
1.45E-01	0.00E+00	5.01E+01	2.74E+00
9.73E-02	0.00E+00	5.25E+01	2.42E+00
4.10E-02	0.00E+00	5.49E+01	2.11E+00
-2.32E-02	0.00E+00	5.73E+01	1.83E+00
-8.97E-02	0.00E+00	5.97E+01	1.56E+00
-1.60E-01	0.00E+00	6.21E+01	1.30E+00
-2.44E-01	0.00E+00	6.45E+01	1.07E+00
-3.35E-01	0.00E+00	6.69E+01	8.42E-01
-4.49E-01	0.00E+00	6.92E+01	6.38E-01
-5.69E-01	0.00E+00	7.16E+01	4.37E-01
-6.98E-01	0.00E+00	7.40E+01	2.40E-01
-8.33E-01	0.00E+00	7.64E+01	3.61E-02
-9.70E-01	0.00E+00	7.88E+01	-1.73E-01
-1.11E+00	0.00E+00	8.12E+01	-4.16E-01
-1.26E+00	0.00E+00	8.36E+01	-6.89E-01
-1.41E+00	0.00E+00	8.60E+01	-1.00E+00
-1.58E+00	0.00E+00	8.83E+01	-1.32E+00
-1.74E+00	0.00E+00	9.07E+01	-1.62E+00
-1.92E+00	0.00E+00	9.31E+01	-1.88E+00
-2.10E+00	0.00E+00	9.55E+01	-2.06E+00
-2.29E+00	0.00E+00	9.79E+01	-2.16E+00
-2.48E+00	0.00E+00	1.00E+02	-2.18E+00
-2.67E+00	0.00E+00	1.03E+02	-2.15E+00
-2.88E+00	0.00E+00	1.05E+02	-2.10E+00
-3.09E+00	0.00E+00	1.07E+02	-2.02E+00
-3.31E+00	0.00E+00	1.10E+02	-1.89E+00
-3.54E+00	0.00E+00	1.12E+02	-1.71E+00
-3.77E+00	0.00E+00	1.15E+02	-1.48E+00
-4.00E+00	0.00E+00	1.17E+02	-1.24E+00

Notice that the key points are entered sequentially (from the root to tip) in accordance with the Z coordinate, which ranges from 0 m (blade root) to 117 m (blade tip).

In addition to the blade geometry, the following parameters are specified in this file, which are necessary for the simulations:

- Quadrature: this value specifies the spatial numerical integration scheme, between Gauss quadrature and trapezoidal quadrature. Trapezoidal quadrature is selected.
- Refine factor: this value is used in trapezoidal quadrature and splits the space between two input stations into “Refine factor” of segments. An increment in the refinement factor multiplies the number of quadrature points for a more precise calculation, however, simulation times are considerably longer. For this reason, a refine factor value of two is selected.
- Number of members: the blade beam model is composed of several “members” in contiguous series. As specified in the BeamDyn user guide: “with the LSFE discretization, a single member and a sufficiently high element order, may well be sufficient. [...] With the LSFE discretization, an increase in accuracy will, in general, be better achieved by increasing the element order (i.e., p-refinement) rather than increasing the number of members (i.e., h-refinement). For Gauss quadrature, the element order should be greater than one” [21]. The element order refers to the order of shape functions for each finite element, which in this case is set to five. For this reason, the number of members is set to one.

### 5.2.2. Blade input file

Named “IEA-15-240-RWT\_BeamDyn\_blade”, this file defines the cross-sectional properties (inertial and structural) at various stations along the blade. The number of stations is changed through the variable “Station\_Total” which is set to twenty-one in this case. This results in a total of forty-one QPs.

Each station is defined through a non-dimensional parameter which specifies its location along the local blade reference axis ranging from [0.0, 1.0], referring the first to the root and the second to the tip, respectively. In each station the stiffness matrix and the mass matrix of the cross section are given, defined in the local coordinate system along the blade axis.

The stiffness matrix has the following form:

$$\begin{bmatrix} K_{ShrFlp} & 0 & 0 & 0 & 0 & 0 \\ 0 & K_{ShrEdg} & 0 & 0 & 0 & 0 \\ 0 & 0 & EA & 0 & 0 & 0 \\ 0 & 0 & 0 & EI_{Edg} & 0 & 0 \\ 0 & 0 & 0 & 0 & EI_{Flp} & 0 \\ 0 & 0 & 0 & 0 & 0 & GJ \end{bmatrix}$$

Where:

- $K_{ShrEdg}$  is the edge shear stiffnesses
- $K_{ShrFlp}$  is the flap shear stiffnesses
- EA is the extension stiffness
- $EI_{Edg}$  is the edge stiffnesses
- $EI_{Flp}$  is the flap stiffnesses

- GJ is the torsional stiffness

The mass matrix is given by:

$$\begin{bmatrix} m & 0 & 0 & 0 & 0 & -mY_{cm} \\ 0 & m & 0 & 0 & 0 & mX_{cm} \\ 0 & 0 & m & mY_{cm} & -mX_{cm} & 0 \\ 0 & 0 & mY_{cm} & i_{Edg} & -i_{cp} & 0 \\ 0 & 0 & -mX_{cm} & -i_{cp} & i_{Flp} & 0 \\ -mY_{cm} & mY_{cm} & 0 & 0 & 0 & i_{plr} \end{bmatrix}$$

Where:

- m is the mass density per unit span
- $X_{cm}$  and  $Y_{cm}$  are the local coordinates of the sectional center of mass
- $i_{Edg}$  is the edge mass moments of inertia per unit span
- $i_{Flp}$  is the flap mass moments of inertia per unit span
- $i_{plr}$  is the polar moment of inertia per unit span
- $i_{cp}$  is the sectional cross-product of inertia per unit span

The cross-section matrices of the twenty-one sections are already known data.

Table 4 summarizes the variables used in the primary input file and the blade input file for the simulations:

*Table 4. Input files variables*

Variable name	Value	Meaning
quadrature	2	Trapezoidal integration method
refine	2	Splits the space between two input stations into two segments
member_total	1	Blade beam model composed of one member
order_elem	5	Order of interpolation (basis) function
kp_total	50	Number of key points used to define the blade geometry
Station_Total	21	Number of sections at which the cross-sectional properties are defined

### 5.2.3. Other input parameters

In addition to the BeamDyn input files, some more files are needed by the other modules of OpenFAST to set the parameters of the simulation:

- Glue code: In the glue code file, named “IEA-15-240-RWT-UMaineSemi.fst”, the integration time step (DT) can be changed. A smaller time step allows for a more precise calculation but increases the computational time. It is necessary to find the balance between the two, for which several test simulations have been carried out, which are explained below. Final time step selected for the simulations is 0,0005 s.
- AeroDyn: The file for this module is called “IEA-15-240-RWT\_AeroDyn15” and allows to set the model of aerodynamics which will be used to compute the loads on the blade.
- Inflow file: In this module the wind speed can be changed, as well as the type of wind condition (steady or turbulent). All the simulations in this work use turbulent wind conditions in order to get more realistic result. The wind speeds are specified below.

- Turbsim: With this module it is possible to generate turbulent wind distributions with de desired mean wind speed, plus modifying more characteristics on the incident wind.
- HydroDyn: In this module it is possible to set the model of the waves (still or non-still water) as well as the wave significant height (m) and peak period of the waves.
- ElastoDyn: In this module, the degrees of freedom (DOF) of the platform can be controlled (fixed or not) as well as the initial blade pitch angle. The precone ( $-4^\circ$ ) and tilt ( $-6^\circ$ ) angles of the wind turbine are fixed here also.

The simulations are run with the help of a matlab script in which the simulation time can be set.

### 5.3. Setting the simulation parameters

Given that the simulations take a long time and to better understand how some input parameters affect the simulation results, some test simulations are first run.

The simulation time is set to 120 seconds (which approximately takes half an hour of running time). This is a small amount of time and is not representative of real situations, but sufficient for testing purposes. The integration time step is set to 0.0005 seconds in the glue code. Latter verifications will make sure that the precision with this integration time is enough. Also, the effect of the waters is neglected and the still water model is used.

To get representative results, the following three wind speeds are chosen:

- 10 m/s
- 14 m/s
- 18 m/s

All of them have been generated using 'Turbsim', which creates turbulent wind distributions with the mean values above mentioned, referred to the hub height. The wind speed distributions are shown in figure 26.

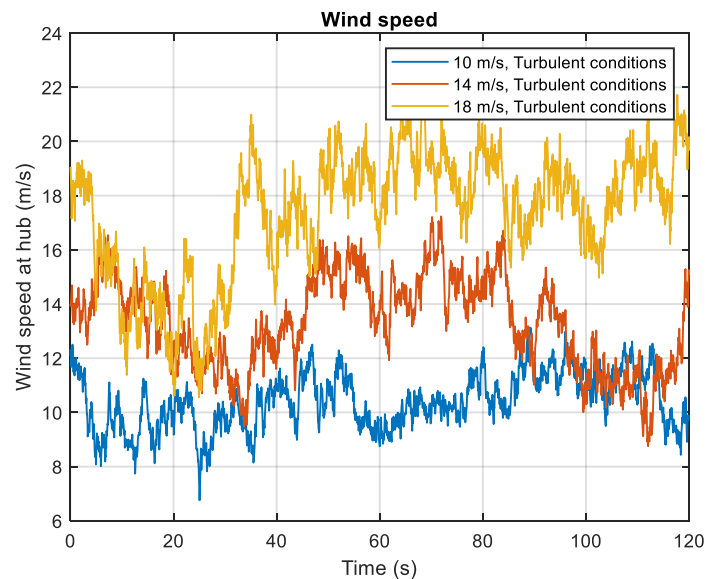


Figure 26. Wind speed distributions for 10, 14 and 18 m/s, 120s

The table 5 summarizes the parameters adopted for the testing simulations:

Table 5. Variables for the test simulations

Variable	Value(s)	Units
Simulation Time (T)	120	s
Integration time step (dT)	0.0005	s
Wind speed (turbulent)	10	m/s
	14	
	18	
Wave conditions	Still water	-

Among the forty-one quadrature points, which are the points of the blade in which BeamDyn performs the calculations, BeamDyn can output the data at a maximum of 9 nodes. The position vector of the quadrature points is specified in the BeamDyn summary file after running the simulation and is exposed below (table 6). Note that they cover the whole blade span, ranging from the blade root (Z = 0 m) to the blade tip (Z = 117 m).

Table 6. Quadrature points position vector in the reference blade coordinate system

QP #	X (m)	Y (m)	Z (m)
1	0.00E+00	0.00E+00	0.00E+00
2	2.75E-02	0.00E+00	2.93E+00
3	5.80E-02	0.00E+00	5.85E+00
4	9.01E-02	0.00E+00	8.78E+00
5	1.23E-01	0.00E+00	1.17E+01
6	1.55E-01	0.00E+00	1.46E+01
7	1.85E-01	0.00E+00	1.76E+01
8	2.12E-01	0.00E+00	2.05E+01
9	2.36E-01	0.00E+00	2.34E+01
10	2.54E-01	0.00E+00	2.63E+01
11	2.67E-01	0.00E+00	2.93E+01
12	2.74E-01	0.00E+00	3.22E+01
13	2.73E-01	0.00E+00	3.51E+01
14	2.65E-01	0.00E+00	3.80E+01
15	2.48E-01	0.00E+00	4.10E+01
16	2.21E-01	0.00E+00	4.39E+01
17	1.85E-01	0.00E+00	4.68E+01
18	1.38E-01	0.00E+00	4.97E+01
19	8.08E-02	0.00E+00	5.27E+01
20	1.24E-02	0.00E+00	5.56E+01
21	-6.75E-02	0.00E+00	5.85E+01
22	-1.59E-01	0.00E+00	6.14E+01
23	-2.62E-01	0.00E+00	6.44E+01
24	-3.78E-01	0.00E+00	6.73E+01
25	-5.05E-01	0.00E+00	7.02E+01
26	-6.45E-01	0.00E+00	7.31E+01
27	-7.96E-01	0.00E+00	7.61E+01
28	-9.60E-01	0.00E+00	7.90E+01
29	-1.13E+00	0.00E+00	8.19E+01
30	-1.32E+00	0.00E+00	8.48E+01
31	-1.52E+00	0.00E+00	8.78E+01
32	-1.73E+00	0.00E+00	9.07E+01
33	-1.95E+00	0.00E+00	9.36E+01

34	-2.18E+00	0.00E+00	9.65E+01
35	-2.41E+00	0.00E+00	9.95E+01
36	-2.66E+00	0.00E+00	1.02E+02
37	-2.92E+00	0.00E+00	1.05E+02
38	-3.18E+00	0.00E+00	1.08E+02
39	-3.45E+00	0.00E+00	1.11E+02
40	-3.72E+00	0.00E+00	1.14E+02
41	-4.00E+00	0.00E+00	1.17E+02

The output nodes (the nodes where the results are gotten) are specified in the BeamDyn input file. They are selected from the root to the tip as evenly distributed as possible (note that the quadrature points are not evenly distributed along the span). The correspondence between the output nodes (N) and the quadrature points (QP) and its coordinates are specified in the table 7.

Table 7. Output nodes position

Node #	QP #	Non-dimensional span	Span (m)
1	1	0	0.0000
2	6	0.125	14.6250
3	11	0.25	29.2500
4	16	0.375	43.8750
5	21	0.5	58.8000
6	26	0.625	73.1250
7	31	0.75	87.7500
8	36	0.875	102.3750
9	41	1	117.0000

To better understand the results, the translational DOF of the tip (motions on X, Y and Z axes) are presented in figures 27, 28 and 29 respectively:

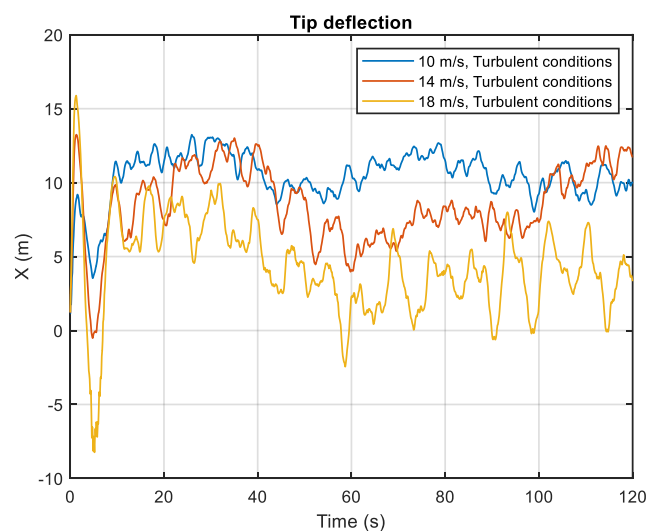


Figure 27. Tip deflection on X axis for 10, 14, 18 m/s, 120s

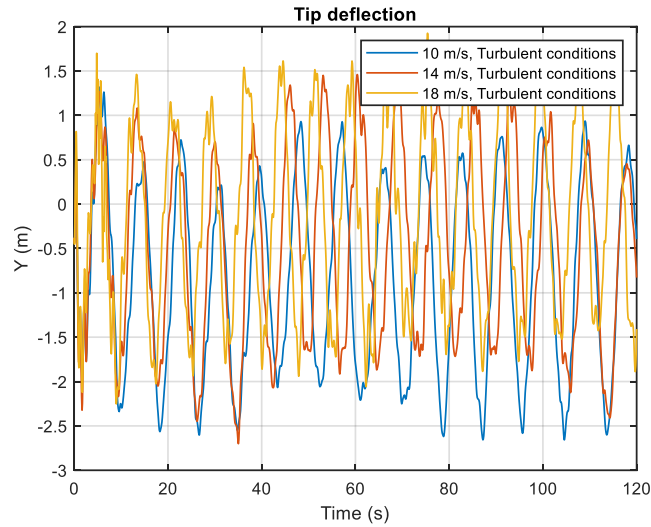


Figure 28. Tip deflection on Y axis for 10, 14 and 18 m/s, 120s

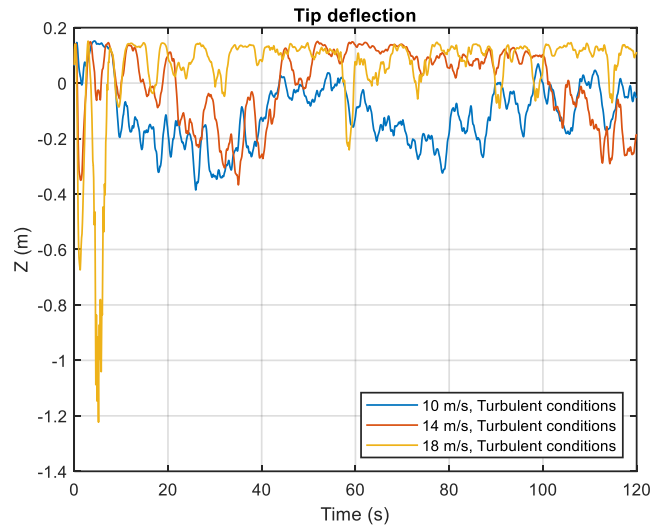


Figure 29. Tip deflection on Z axis for 10, 14 and 18 m/s

The effects of the deflection are much higher on the X axis (0, 13 m) than in the Y (-2.5, 1.5 m) and Z (-1.2, 0.2 m) axes. The first instants are dominated by oscillations as the initial blade pitch is set to  $0^\circ$  and the controller adjust it as can be seen on figure 30. Counter-intuitively, (ignoring therefore the transient time at the beginning of the simulation) the deflection on the X axis is slightly bigger for the 10 m/s case and decreases with the windspeed. This is due to the action of the controller, which increases the blade pitch for higher wind speeds. If the controller was switched off, the expected results would be the opposite of those obtained.

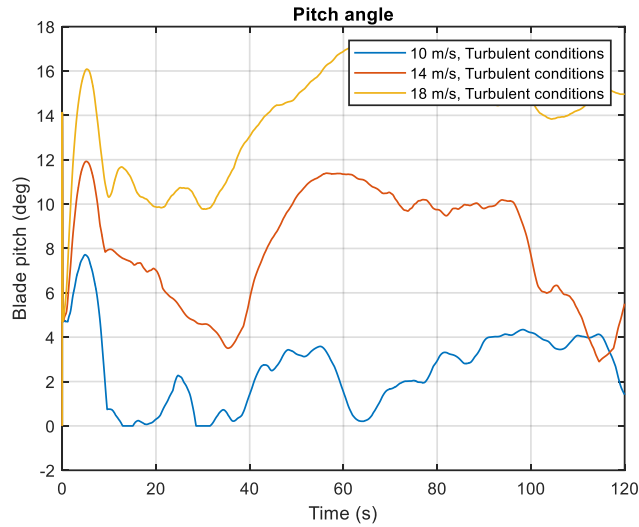
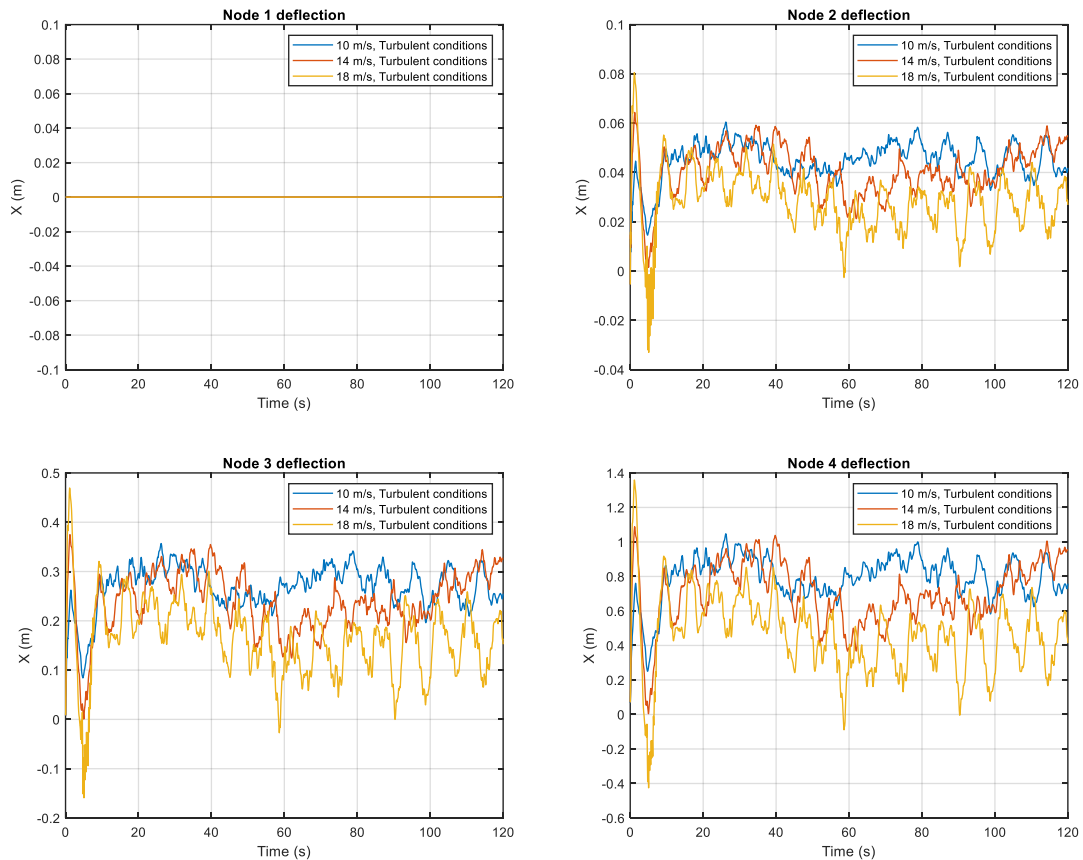


Figure 30. Pitch angle for 10, 14 and 18 m/s

In the Y and Z directions the deflection is one and two orders of magnitude smaller than in the X direction, respectively. It is observed that in these axes the deflection increases slightly with wind speed.

The deflection on X axis (as it is the one that best represents the blade behaviour) is now presented for the nine output nodes (figure 31):



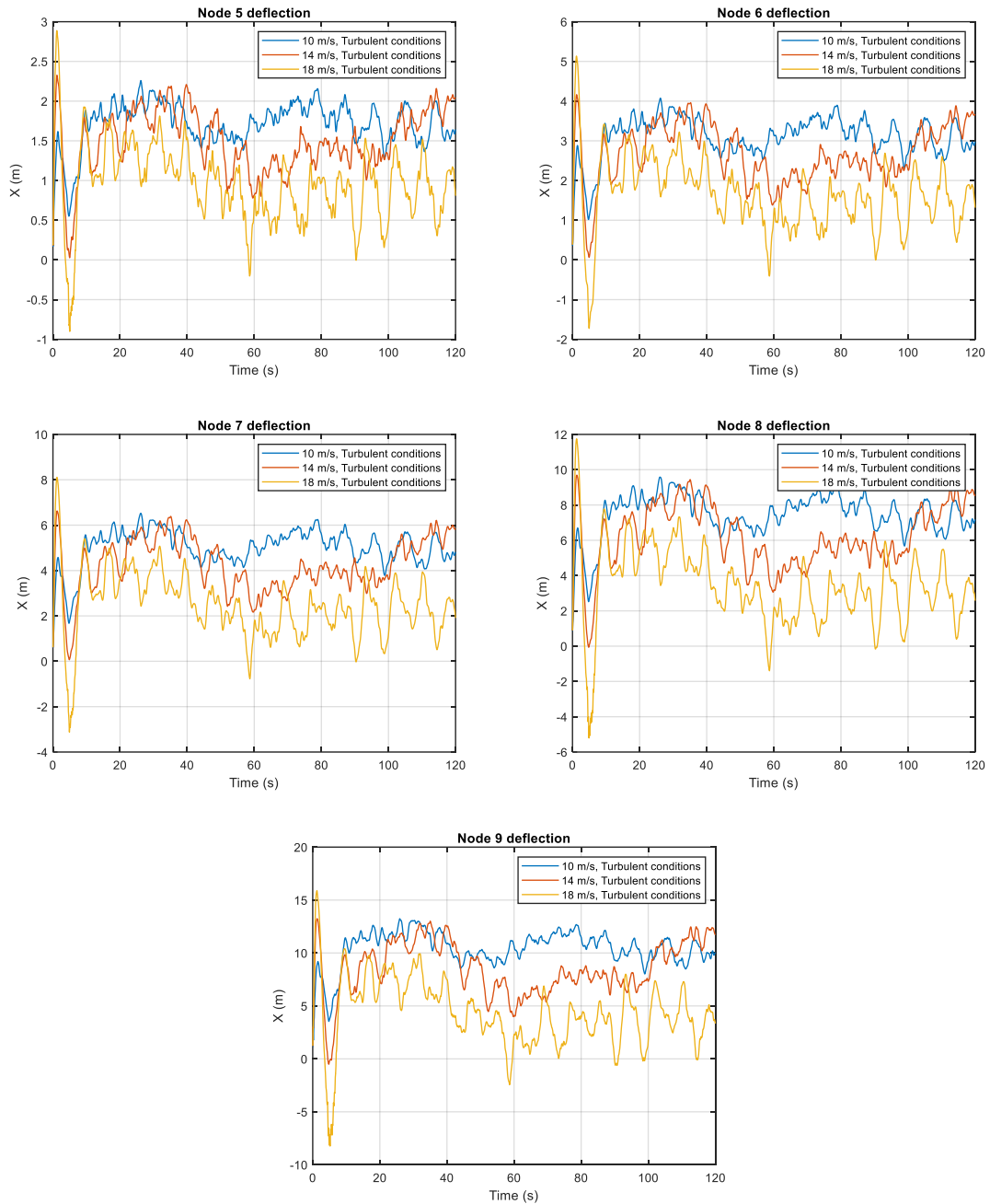


Figure 31. Deflection in nodes 1-9 for 10, 14 and 18 m/s, 120s

Where the first and ninth nodes correspond to the root and the tip of the blade, respectively. As expected, the deflection is maximum at the tip and decreases as the span decreases, until it reaches zero displacement at the root. The shape of the deflection of the nodes as the z-coordinate increases is similar.

Having these data, it is possible retrieve the maximum deflection of the blade. This happens for the 10 m/s windspeed case, where the deflection (X axis) reaches 13,24 m at its maximum point, which happens at  $t = 25.9$  s. This point is represented in figure 32.

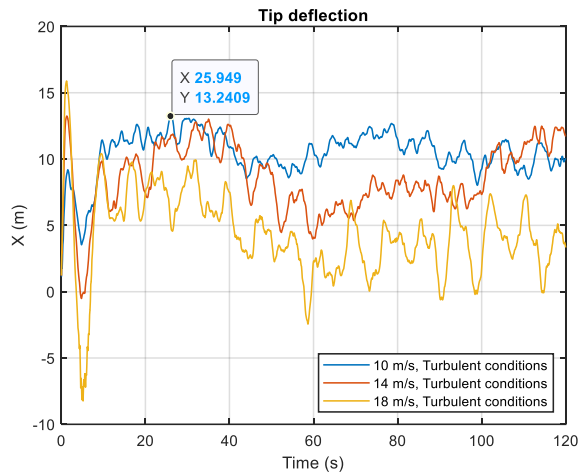


Figure 32. Maximum deflection, 10m/s and 120s

With the deflection of the nodes, a matlab script is created to plot the three-dimensional deflection of the blade, for every time step. With it, is possible to see how the blade changes shape over time. The 3D deformed and undeformed shape of the blade at the instant of maximum deflection is represented in figure 33, whereas the deflection in the X and Y axes at the same moment are plotted in figure 34.

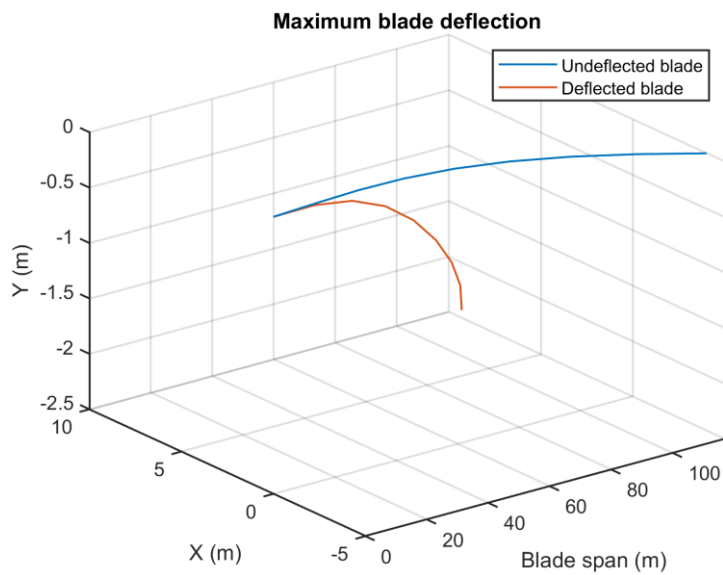


Figure 33. Three-dimensional deflection, 10m/s and 120s

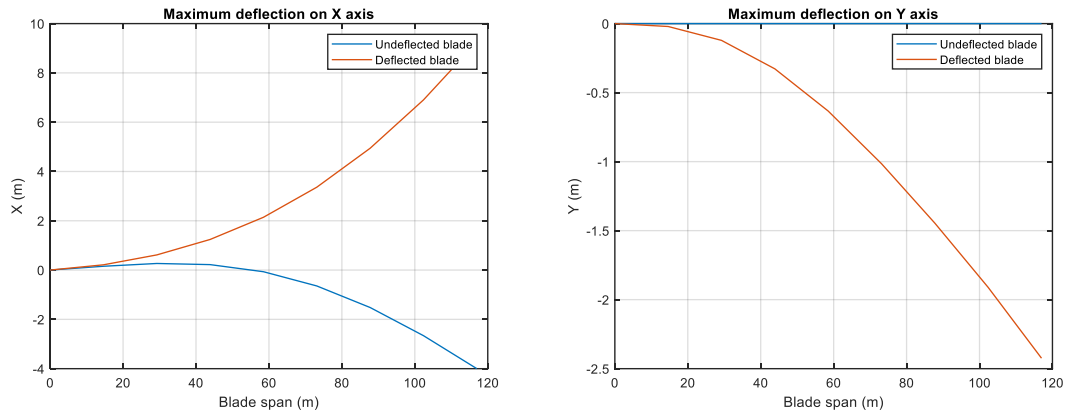


Figure 34. Maximum deflection on X (left) and Y (left) axes, 10m/s and 120s

To verify that the chosen time step is sufficiently accurate, another 30-second simulation is performed with a smaller time step of 0.0002s. The results are compared with the previous results and the tip deflection is shown in figure 35.

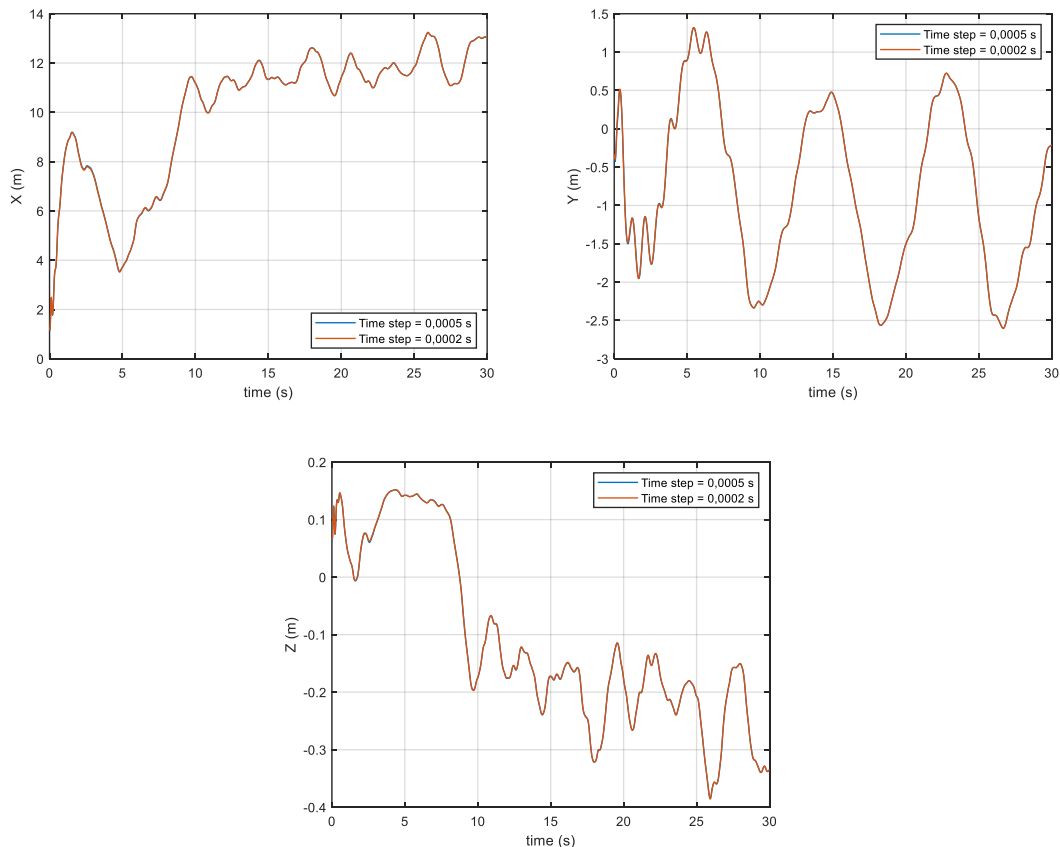


Figure 35. Time step comparison of the tip deflection, between 0.0005s and 0.0002s

The deflection for the smaller time step (0.0002s, in orange), is the same as the bigger one (0.0005s in blue) as both graphs overlap, so it is possible to conclude that a time step of 0.0005s is small enough to get accurate results. It is noted that the simulations with the smaller time step have taken much longer time to complete (about 5 hours for just 30 seconds of simulation time), while the one with higher time step achieved the same accuracy while running much quicker.

Bigger time steps have also been tested: convergence is not reached for time steps bigger than 0.0006s. In any case, for values smaller the results are consistent. For this reason, the final time step chosen to perform the simulations is 0.0005s.

## 5.4. Design load case

### 5.4.1. Site environmental conditions

In order to carry out a realistic and representative fatigue analysis and to take account of the external forces on the blades, a location has to be chosen and the environmental conditions from this location have to be used in the simulations. The variables involved are:

- Wind speed ( $V$ ), in meters per second
- Significant height of the waves ( $H_s$ ), in meters
- Peak period of the waves ( $T_s$ ), in seconds

In this case the same data as in [22] is used (Sirigu, et al, 2022), as the results are to be compared. As explained by Sirigu, et al, 2022, the real scatter of the wind, height and period of the waves is obtained from the shore of Pantelleria, Italy in ten years of data acquisition. The occurrence of the wind speed in Pantelleria based on these data is shown in figure 36.

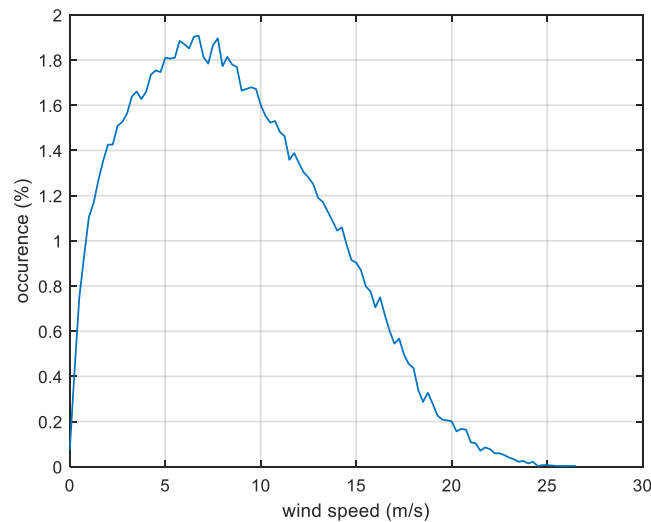


Figure 36. Occurrence of the wind speed in Pantelleria, Italy in ten years of data collection [22]

The standard IEC 61400 [23] describes the design load cases for offshore wind turbines. The life of a wind turbine can be represented by a set of design scenarios that cover the most significant conditions it may experience throughout its lifetime. These situations include normal design conditions, but also transport, installation and maintenance conditions. For all of them, the standard describes a set of design load conditions (DLC) which are divided into:

- Power generation (DLC 1)
- Power generation plus fault occurrence (DLC 2)
- Start-up (DLC 3)
- Normal shut-down (DLC 4)

- Emergency stop (DLC 5)
- Parking (stationary or idling) (DLC 6)
- Parking and fault conditions (DLC 7)
- Transport, assembly, maintenance and repair (DLC 8)

The load case DLC 1.2 (power production in normal turbulence) is used for the fatigue analysis. This load case is used for fatigue assessment and consists of the simulation of power production without faults performed for wind speeds in the entire operational range with normal turbulence ( $V_{in} < V_{hub} < V_{out}$ ) and a normal sea state. The wind and wave states are evaluated according to a joint probability distribution and each wind speed ( $V_{hub}$ ) is assigned a wave state ( $H_s$ ,  $T_p$ ). The wind speed is discretized in intervals of 0,25 m/s, the wave height in intervals of 0,25 m and the peak period in intervals of 0,25 s.

Table 8 summarises the environmental conditions for setting up the simulation:

*Table 8. Wind and sea states used in the simulations*

<b>V (m/s)</b>	<b>Hs (m)</b>	<b>Ts (s)</b>
5	1.2	6.24
7	1.37	6.25
9	1.59	6.20
11	1.89	6.24
13	2.22	6.38
15	2.64	6.62
17	3.19	7.06
19	3.72	7.38
21	4.31	7.85
23	4.71	7.95

Resulting in ten different simulations to be performed. The simulation time is set to 600s (10 min) as recommended by [24].

#### 5.4.2. Applied forces on the blade

Each of the conditions described above produce different forces applied on the blades. With MOST [25], these forces can be obtained through a lookup table in Matlab. For example, for a wind speed of 15 m/s, the following normal and tangential pressures ( $p_n$  and  $p_t$ , respectively) act on the blade (figures 37 and 38):

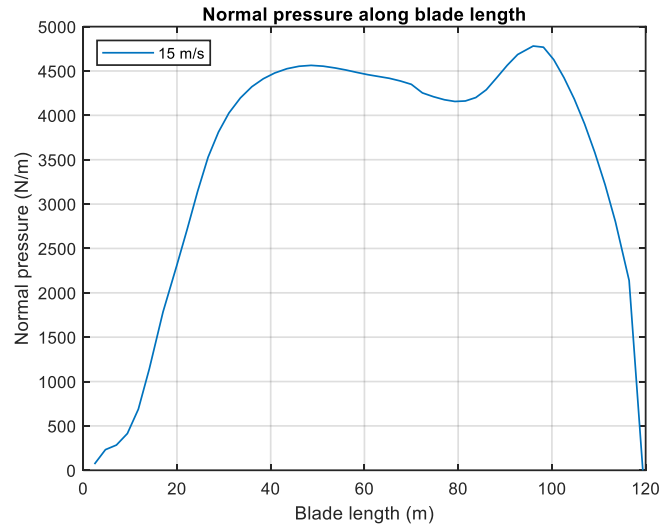


Figure 37. Normal pressure ( $p_n$ ) along blade length

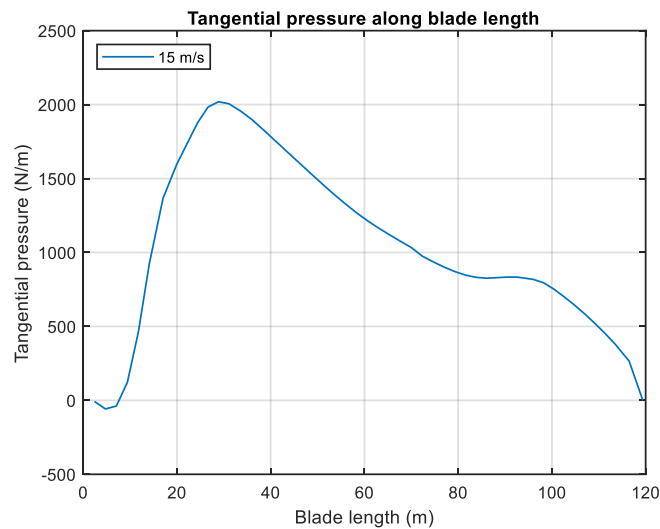


Figure 38. Tangential pressure ( $p_t$ ) along blade length

Where both  $p_n$  and  $t_n$  are zero at the root and blade tip and are calculated according to:

$$p_n = \frac{1}{2} \rho v^2 C_n l$$

$$p_t = \frac{1}{2} \rho v^2 C_t l$$

In every section along the span, where:

- $\rho$  is the air density ( $1.225 \text{ kg/m}^3$ )
- $v$  is the wind speed
- $C_n$  is the normal drag coefficient
- $C_t$  is the tangential drag coefficient
- $l$  is the chord of the section

Integrating the pressures along the length of the blade gives the external forces,  $F_x$  and  $F_y$  (figures 39 and 40) and moments,  $M_x$  and  $M_y$  (figures 41 and 42):

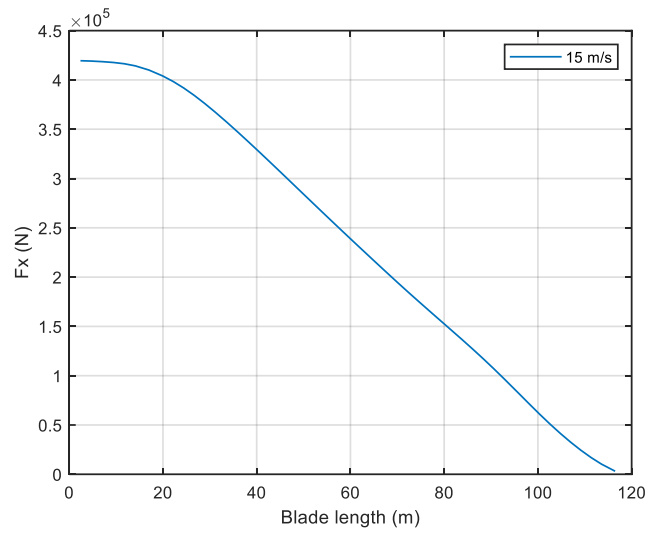


Figure 39.  $F_x$  along the blade length

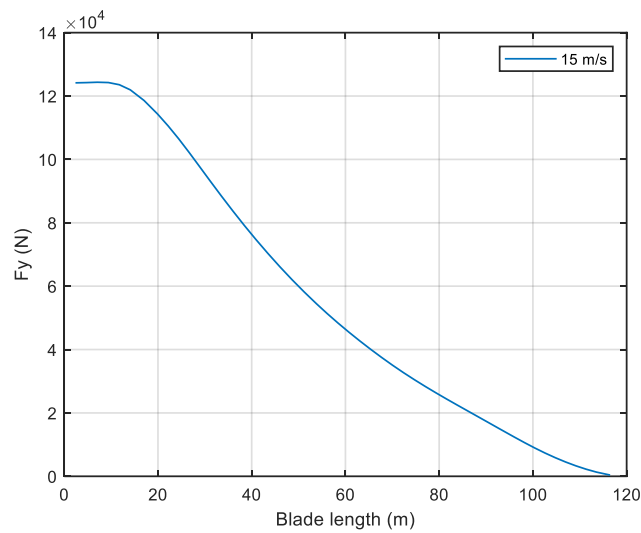


Figure 40.  $F_y$  along the blade length

Where it can be seen that both  $F_x$  and  $F_y$  decrease monotonically from the root of the blade to the tip. Note that  $F_x$  is an order of magnitude larger than  $F_y$ .  $F_x$  and  $F_y$  are calculated according to:

$$F_x = \int p_n(z) dz$$

$$F_y = \int p_t(z) dz$$

Where  $z$  is the blade span.

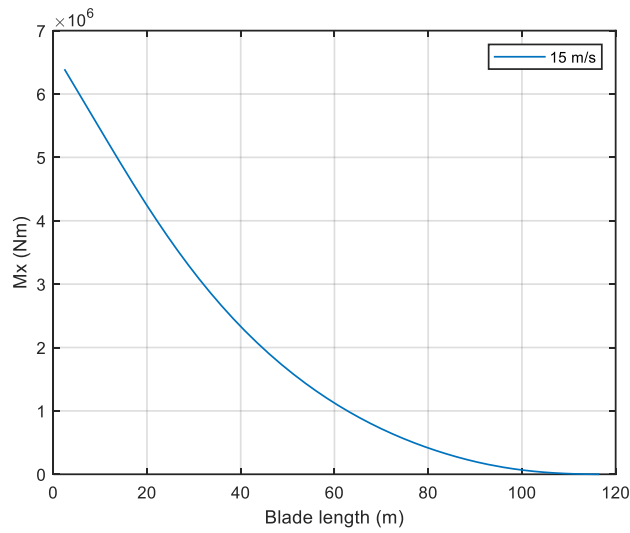


Figure 41.  $M_x$  along the blade length

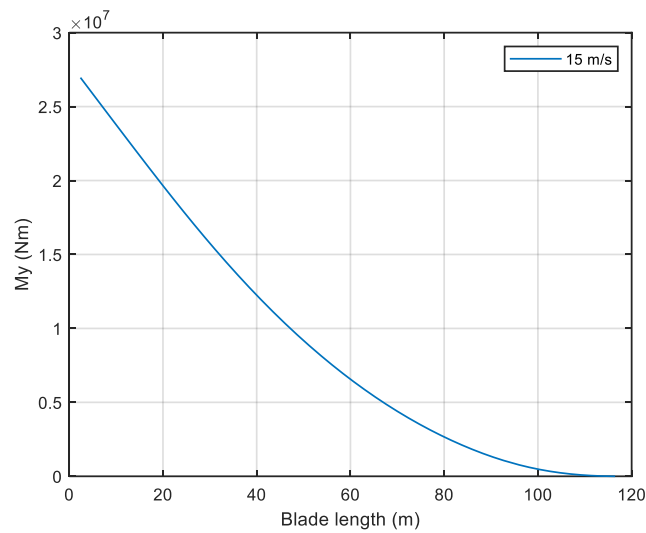


Figure 42.  $M_y$  along the blade length

The external moments  $M_x$  and  $M_y$  are calculated according to:

$$M_x = \int p_n(z) z dz$$

$$M_y = \int p_t(z) z dz$$

In this case,  $M_y$  is predominant over  $M_x$ . Again, both decrease monotonically from the root to the tip.

## 5.5. Simulation results

In this section the results obtained in the simulation are presented. Table 9 summarizes the main parameters used in the simulation.

*Table 9. Simulation inputs*

Variable	Value(s)	Units	V (m/s)	Hs (m)	Ts (s)
Simulation Time (T)	600	s	5	1.2	6.24
Integration time step (dT)	0.0005	s	7	1.37	6.25
Output nodes	9	-	9	1.59	6.20
			11	1.89	6.24
			13	2.22	6.38
			15	2.64	6.62
			17	3.19	7.06
			19	3.72	7.38
			21	4.31	7.85
Total number of simulations:	10		23	4.71	7.95

Each simulation takes between two to three hours to complete. For each wind speed and sea state, a structure in Matlab is created to store the results. Each structure contains the following arrays of values in time:

- Time step of the simulation
- Windspeed
- Power
- Rotor speed
- DOF of the platform (surge, sway, heave, roll, pitch and yaw)
- Blade pitch
- DOF of the blade tip
- DOF of the blade nodes
- Internal forces at the blade root (forces and moments)
- Internal forces at the blade nodes (forces and moments)

Each of them with a length of 1.200.000 time-steps (corresponding to 600s/0,0005s). The results of the simulation are shown below, disregarding the first ten seconds of simulation to overcome the transient effects. For clarity purposes, only the results of three different wind speeds, 7, 15, and 21m/s are showed, given that showing all the results at once does not allow to appreciate them properly. The generated wind speeds are shown in figure 43.

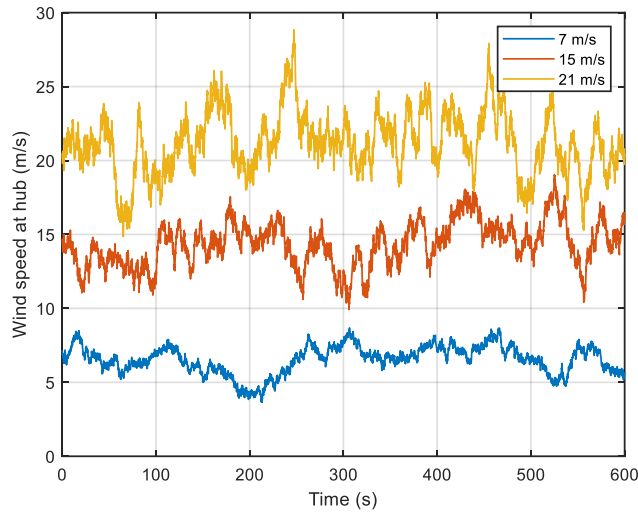


Figure 43. Wind speed

### 5.5.1. Power

The power developed by the wind turbine is showed in figure 44, during the 600s of simulation. For 15 and 21m/s wind speeds, the power is centred around the rated power which is 15 MW. On the other hand, for the case of 7 m/s the extracted power is clearly lower since the wind speed is less than the nominal wind speed (10.59 m/s).

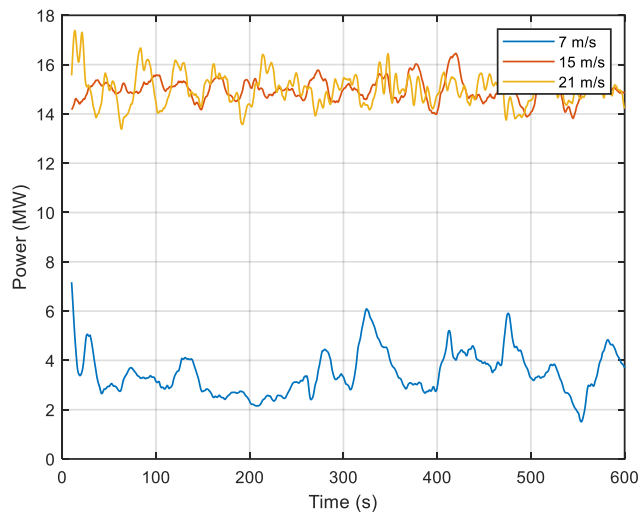


Figure 44. Power

### 5.5.2. Rotor speed

The rotor speed is showed in figure 45, during the 600s of simulation. For 15 and 21m/s wind speeds, the rotor speed is centred around its maximum one which is 7,56 rpm. Regarding the 7m/s case, the rotor speed is centred around its minimum value which is 5 rpm.

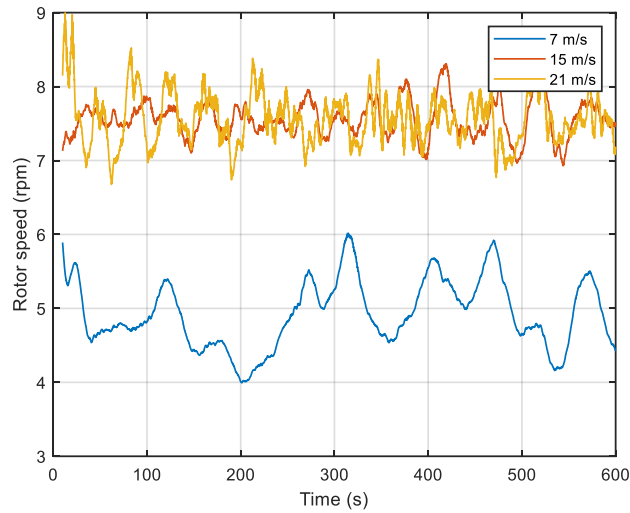
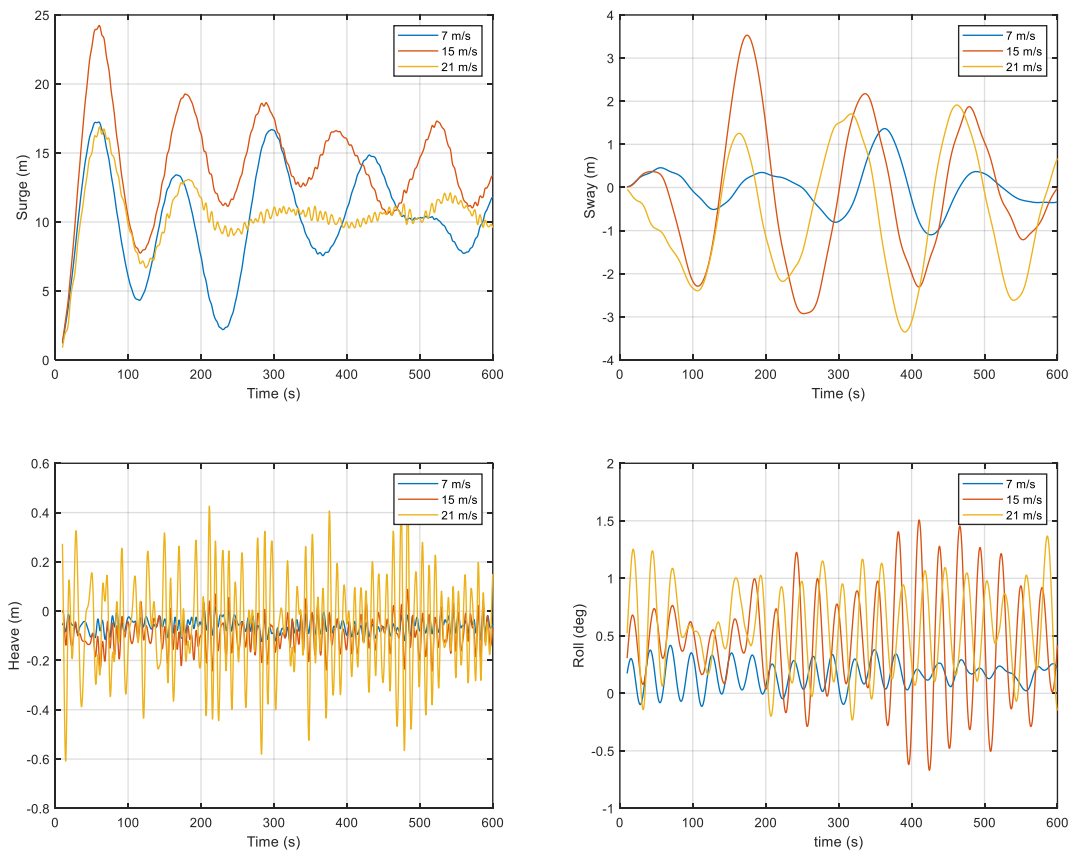


Figure 45. Rotor speed

### 5.5.3. DOF of the platform

Figure 46 shows the DOF of the platform: three translational (surge, sway and heave) and three rotational (roll, pitch and yaw).



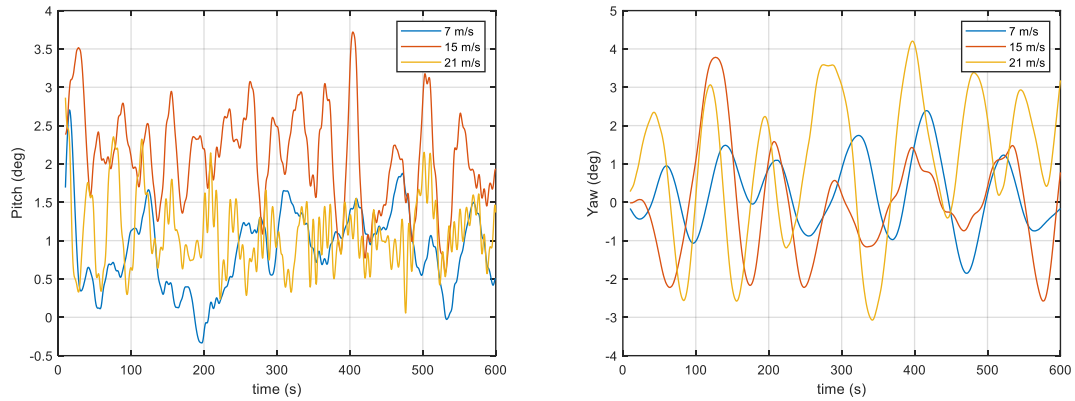


Figure 46. DOF of the platform

As can be seen between the translational DOF, the amplitude of the oscillations of the surge is higher than the ones on the sway and the heave, reaching almost 25 meters. This is because the surge axis is aligned with the direction of the waves and therefore the oscillations on this axis are bigger.

The effect of the waves can be clearly seen in the case of the highest wind speed, 21m/s, where the vertical oscillations (heave) exceed half a metre. In contrast, for lower waves (and therefore lower wind speeds), the oscillations are less than half this magnitude.

Concerning the rotational DOF, the pitch presents higher oscillations as it axes is perpendicular to the direction of the waves, reaching almost 4°. The yaw presents oscillations of the same order of magnitude while the roll oscillations reach a maximum if 1,5°.

#### 5.5.4. Blade pitch angle

Figure 47 shows the pitch angle of the blade during the 600s of simulation.

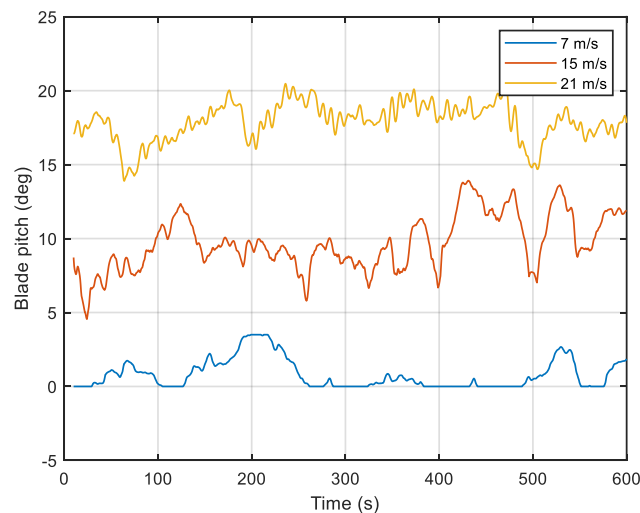


Figure 47. Blade pitch angle

As explained above in the test simulations, the higher the wind speed, the higher the pitch angle set by the controller, which is consistent with the results. For the 7m/s case the pitch is

practically zero, while for the 15 and 21 m/s cases the pitch angle ranges between 10 and 17 degrees, respectively.

### 5.5.5. DOF of the blade tip

Figure 48 presents the translational deflections of the blade tip along X axis. Figure 49 presents the translational deflections of the blade tip along Y and Z axes. Y and Z motions have been adjusted on time axis for better visualization.

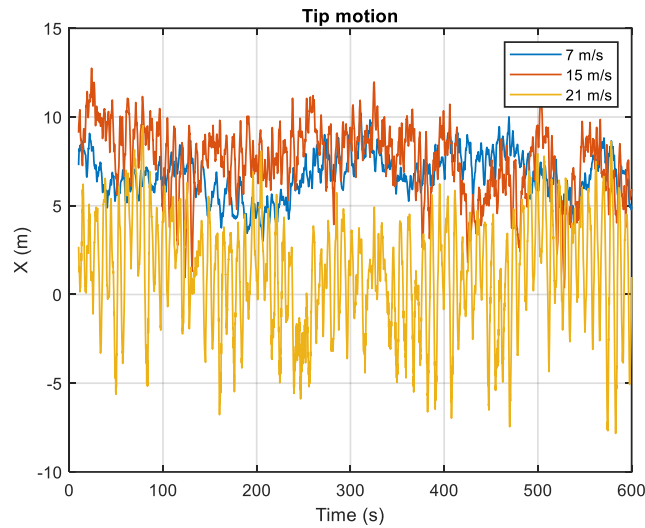


Figure 48. Tip deflection along X

As seen before, the average deflection is higher for medium wind speeds. This is because at low speeds, the wind thrust force is small and causes little deflection, while at high speeds the controller increases the pitch angle and the deflection decreases. The intermediate case (15 m/s, orange) is the one with the highest deflection, as the wind speed is considerable but the pitch angle is not so large. On the other hand, as the wind speed increases, the oscillations increase: the 7 m/s case (blue) presents oscillations between [5, 10] m; while the 21 m/s case presents oscillations between [-8, +10] m.

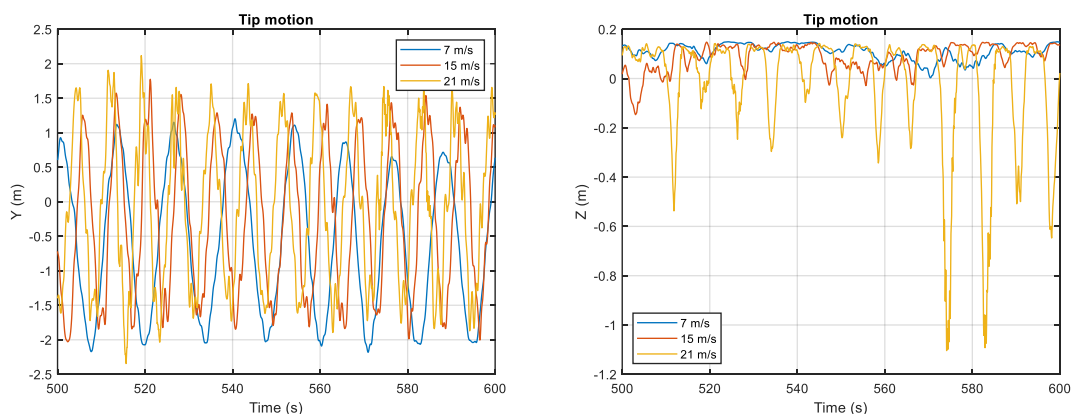


Figure 49. Tip deflection along Y (left) and Z (right)

As for the other translational deflections, their effects are, in general, much smaller. On the Y axis the mean deflections and the oscillations are similar for the different wind speeds and range

from [-2.5, 2] m approximately. On Z axis the mean deflection is small for all the cases, however for greater wind speeds it presents negative oscillations up to -1 m.

The maximum deflection between all the case studied is found to happen at a wind speed of 13 m/s, where the maximum deflection reached along X axis is 14,785 m relative to the undeflected position of the blade. Figure 50 shows a 3D representation of the deflected and undeflected blade at this exact moment. Figure 51 shows the same instant but referred to X and Y axes.

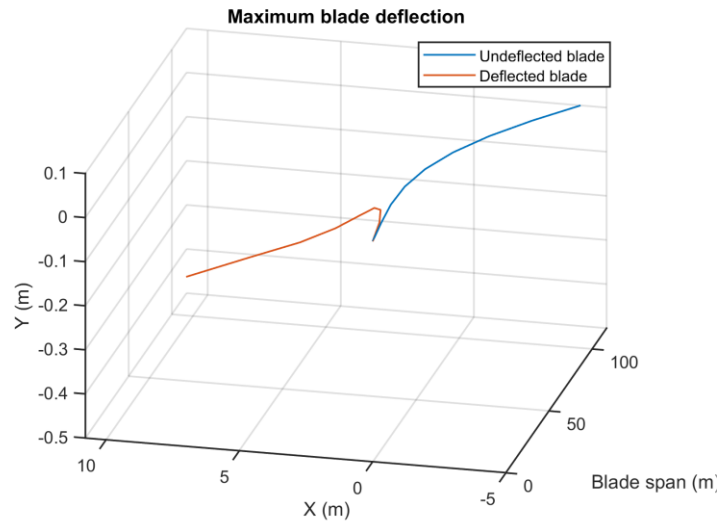


Figure 50. Maximum deflection. Wind speed is 13 m/s

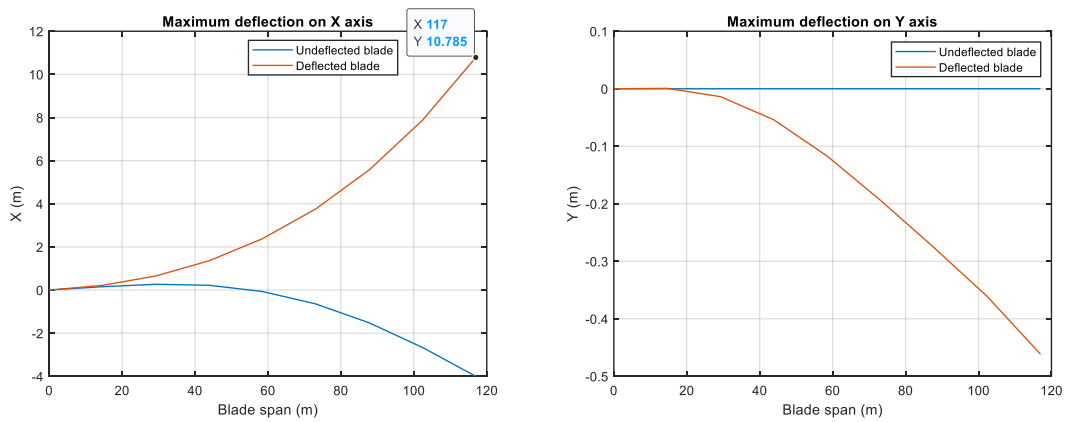


Figure 51. Maximum deflection along X and Y. Wind speed is 13 m/s

### 5.5.6. DOF of the blade nodes

Figure 52 presents the translational deflections along X axis of the nine nodes of the blade for the 15 m/s case. Each coloured line represents a node of the blade: the node one coincides with the blade root and the node nine coincides with the tip. Figure 53 presents the translational deflections along Y and Z axis.

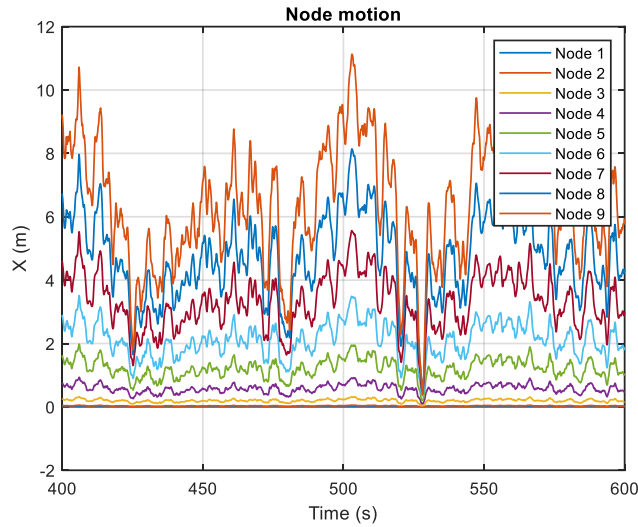


Figure 52. Nodes deflection along X. Wind speed is 15 m/s

It can be clearly seen that the shape of the deflection of all the nodes is the same and increases as the blade span increases. For node 1, at the root, the deflection is zero or practically zero as the blade is cantilevered to hub. The deflection increases at the different nodes until it reaches the ninth node, at the tip which has no external motion restrictions.

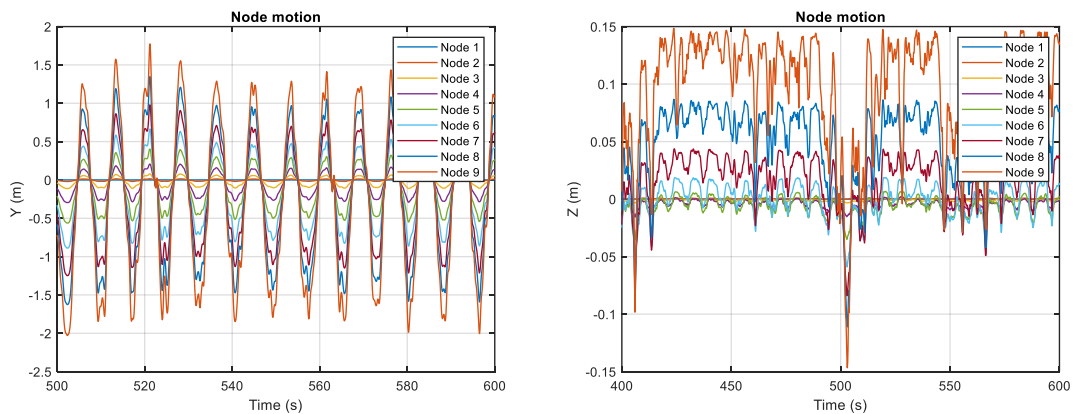


Figure 53. Nodes deflection along Y (left) and Z (right). Wind speed is 15 m/s

As for the deflection in the Y and Z axes, the trend is the same. The deflection is zero at the root and increases along the blade until it reaches the tip, where it becomes maximum. The shape of all the nodes is the same.

### 5.5.7. Internal forces at the blade root

Figure 54 presents the internal forces and moments in the root section of the blade. The forces, expressed in Newtons (N), are the edgewise force (or the internal force along X axis), flapwise force (or internal force along Y axis) and vertical force (or internal force along Z axis, that is the direction of the blade span). The moments, expressed in Newton-meters (Nm), are the edgewise moment (or internal moment along X axis), flapwise moment (or internal moment along Y axis) and the torque moment (or internal moment along Z axis).

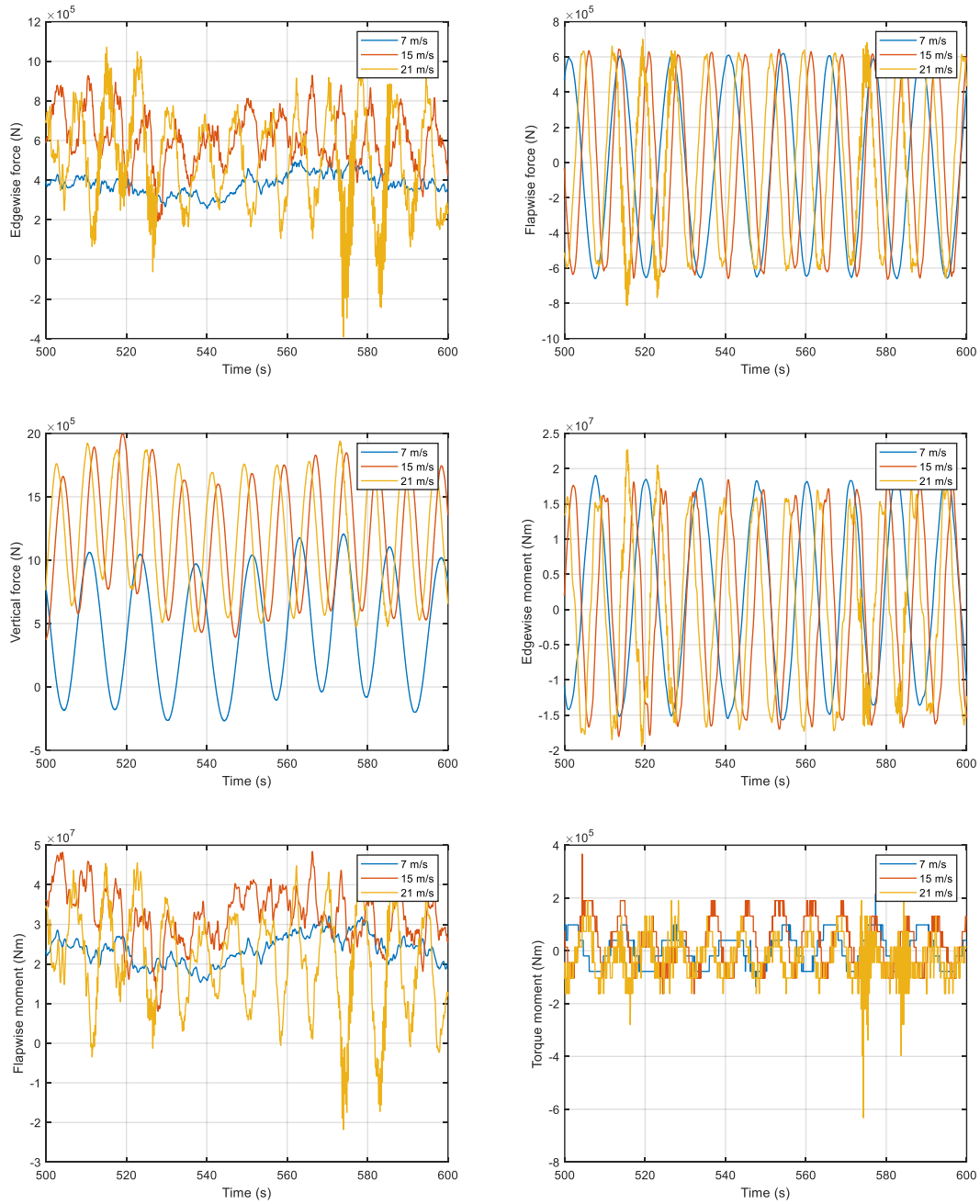


Figure 54. Blade root reaction forces

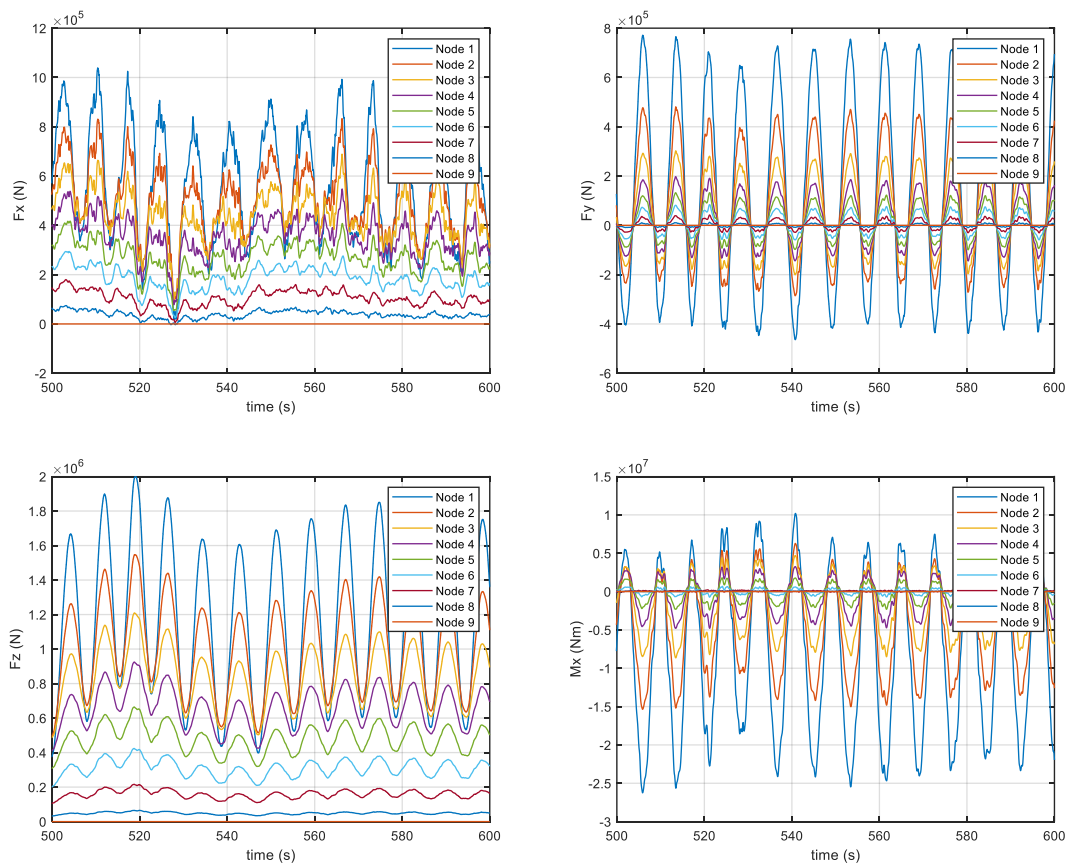
The edgewise, flapwise and vertical forces are of the same order of magnitude. The edgewise force exhibits larger oscillations and higher mean values as the wind speed increases. It generally oscillates between the values  $[0, 10 \times 10^5]$  N for the higher wind speed values. As for the flapwise force, the oscillations are similar for all cases, generally in the range  $[-6 \times 10^5, 6 \times 10^5]$  N, and centred at the origin. Finally, the vertical force is where the highest values are reached, close to  $20 \times 10^5$  N. In this case, the higher the wind speed, the higher the average vertical force (see how in the figure, the vertical force in the case of 7 m/s is lower than that of 15 m/s, which in turn is lower than that of 21 m/s). As for the oscillations, they are all of similar intervals  $[-2, 12]$  N for the 7 m/s case, and  $[5, 20]$  N for the 15 and 21 m/s cases, approximately).

The last three graphs of the figure show the bending moments (flapwise and edgewise) and the torque moment. The edgewise moment is the one that gives torque to the rotor, while the

flapwise moment is the one generated by the wind force. Both are orders of magnitude larger ( $10^7$  Nm) than the torque moment ( $10^5$  Nm). The edgewise moment has similar oscillations for different wind speeds, centred at the origin and in the range of approximately  $[-2 \times 10^7, 2 \times 10^7]$  Nm. In the flapwise moment, the amplitude of the oscillations increases with wind speed, reaching peak values of  $5 \times 10^7$  Nm. For lower speeds, the curve is more constant and changes less abruptly. Finally, the torque moment generally presents oscillations of more moderate amplitude, in the range of  $[-2 \times 10^5, 2 \times 10^5]$  Nm and centred at the origin.

### 5.5.8. Internal forces at the blade nodes

Figure 55 shows the internal sectional forces ( $F_x$ ,  $F_y$  and  $F_z$ ) in Newtons, and moments ( $M_x$ ,  $M_y$  and  $M_z$ ) in Newton-meters of the nine different nodes along the blade length. Each coloured line represents a node of the blade: the node one coincides with the blade root and the node nine coincides with the tip. The wind speed for the case shown is 15 m/s.



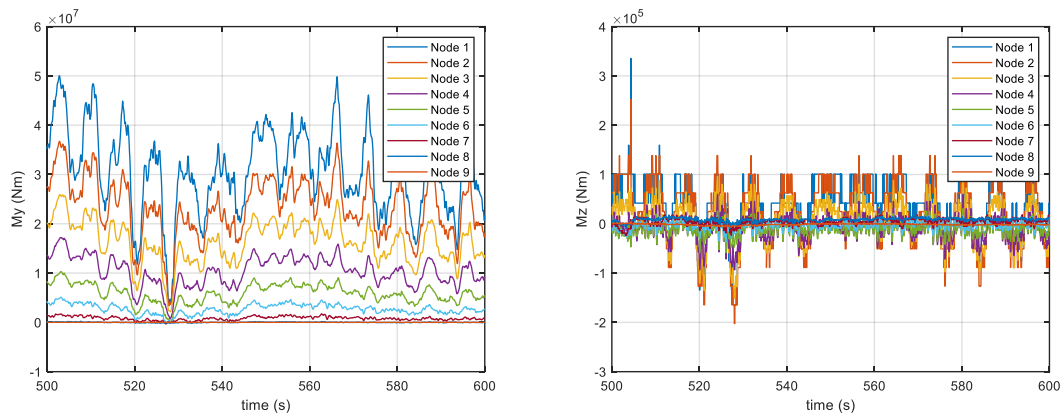


Figure 55. Internal forces at the blade nodes. Wind speed is 15 m/s

The shape of the internal forces for all the nodes is the same and decreases with the blade span. For node 1 at the blade root, the forces and moments reach the maximum values as is where the blade is cantilevered. For node 9, all the forces cancel out, as it is the end of the blade.

## 6. Fatigue analysis

In this section the fatigue analysis methodology is explained and applied. Firstly, on the root of the blade, and finally on several sections distributed along the blade.

### 6.1. Fatigue analysis on the blade root

The fatigue analysis on the blade root can be done following a simplified approach due to its simple geometry and composition: a circular cross-section with a thickness of 100 mm, made with a traditional triaxial fiberglass composite. The methodology followed in this analysis is the same approach used by Sirigu, et al, 2022 [22], as results are to be compared.

The root section is shown in figure 56 and its dimensions and material properties are listed on table 10.

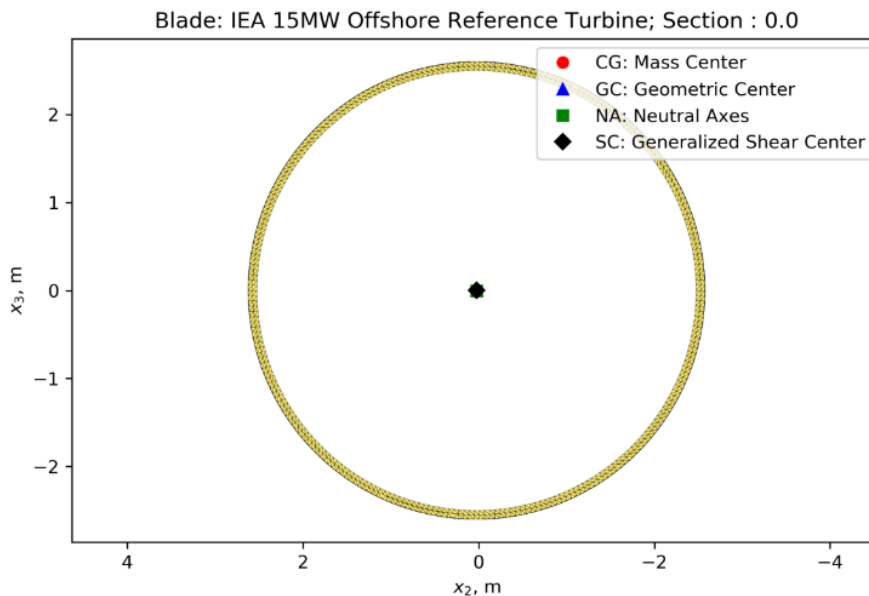


Figure 56. Blade root cross-section

Table 10. Geometry of the blade root cross-section and properties of the composite material [22]

<b>Composite name</b>	Vectorply E-LT-5500 (triaxial fiberglass)
<b>Density</b>	1960 kg/m <sup>3</sup>
<b>Ultimate tensile strength <math>S_{ut}</math></b>	396 MPa
<b>Fatigue parameter <math>m</math> (Slope of S-N curve)</b>	39.6 MPa
<b>External diameter</b>	5.2 m
<b>Thickness</b>	100 mm
<b>Area section</b>	1.6022 m <sup>2</sup>
<b>Inertia section</b>	5.2112 m <sup>4</sup>

### 6.1.1. Stress recovery

The first step to perform the fatigue analysis on the blade root is to retrieve the stress on different points along the section, on the basis of the internal forces and moments that have been obtained from the simulations. The fatigue analysis only considers the uniaxial load on the blade, caused by the bending moments ( $M_x$  and  $M_y$ ) due to the aerodynamic and the gravitational forces, and the vertical force ( $F_z$ ) caused by the gravity and the centrifugal forces. Thus, the internal shear forces ( $F_x$  and  $F_y$ ) are neglected, as well as the torsional moment ( $M_z$ ).

The resulting axial stress or mechanical stress derived from these forces is computed as:

$$\sigma = \frac{M_x \cdot R \cdot \cos(\alpha + \beta)}{J} + \frac{M_y \cdot R \cdot \sin(\alpha + \beta)}{J} + \frac{N}{A}$$

Where:

- $M_x$  is the edgewise moment, i.e., the moment that gives torque to the rotor
- $M_y$  is the flapwise moment, i.e., the moment caused by the wind thrust force
- $N$  is the axial force (or vertical force,  $F_z$ )
- $A$  is the area of the cross section (see table 10)
- $J$  is the inertia of the cross section (see table 10)
- $R$  is the external radius of the blade root circumference
- $\alpha$  is the blade pitch angle
- $\beta$  is the angle along the blade root circumference

The stress is evaluated on the external circumference of the blade root (as it is where the stress due to the bending moments is greater), at several points with a discretization of 10 degrees ( $\beta$  angle). The resulting mechanical stress is shown on figure 57 for the whole simulation time (except the first ten seconds, as they have been disregarded to ignore the transient) and a closer look is shown on figure 58. The stress is shown in the point  $\beta = 90^\circ$ , which, as will be seen later, is the most critical one in the cross section).

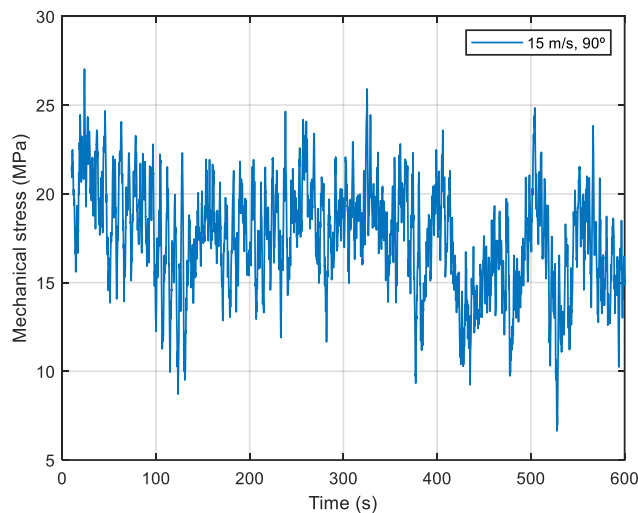


Figure 57. Mechanical stress at the blade root.  $\beta = 90^\circ$  and wind speed is 15 m/s

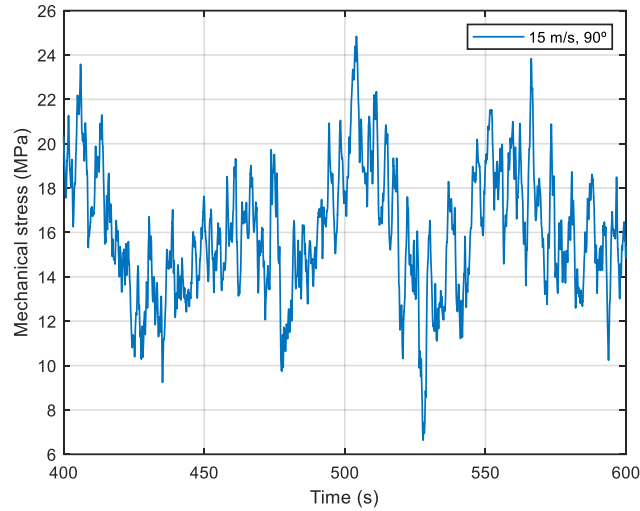


Figure 58. Closer look to the mechanical stress at the blade root,  $\beta = 90^\circ$  and wind speed is 15 m/s

### 6.1.2. Damage and life calculation

The next step on the fatigue analysis is to compute the damage equivalent load and the expected fatigue life on the blade section. To do so, the theory explained in the second chapter will be used.

Starting from the mechanical stress, a Rainflow algorithm is used, according with the ASTM E 1049, to calculate the number of cycles and the alternate and mean stress ( $\sigma_a$  and  $\sigma_m$ , respectively) of each of them. The S-N curve equation is shown below:

$$S_e = S_{ut} - m \cdot \log_{10}(N)$$

To account for the effect of the mean stress, a constant life Goodman diagram has to be used. A variety of different curves exist, but for the sake of simplicity, the modified Goodman line will be used. This curve is linear (as opposed to others, which may be quadratic or with other shapes, see fatigue theory in chapter two), and is one of the simplest analyses, but a widely used resource as it generally fits great with the actual fatigue behaviour. The modified Goodman line is characterized by the following equation:

$$\frac{\sigma_a}{S_e} + \frac{\sigma_m}{S_{ut}} = 1$$

This rule states that the fatigue life at alternating stress  $\sigma_a$  and mean stress  $\sigma_m$  is equal to the fatigue life at an equivalent zero-mean-stress alternating stress state of  $S_e$ . By putting the two equations together and substituting  $S_e$ , one can obtain explicitly the  $N$  value of cycles that the material can withstand at each point. The algebraic steps are shown below:

$$\frac{\sigma_a}{S_{ut} - m \log_{10}(N)} + \frac{\sigma_m}{S_{ut}} = 1$$

$$\log_{10}(N) = \frac{S_{ut}^2 - \sigma_a \cdot S_{ut} - \sigma_m \cdot S_{ut}}{m(S_{ut} - \sigma_m)}$$

$$N = 10 \frac{S_{ut}^2 - \sigma_a \cdot S_{ut} - \sigma_m \cdot S_{ut}}{m(S_{ut} - \sigma_m)}$$

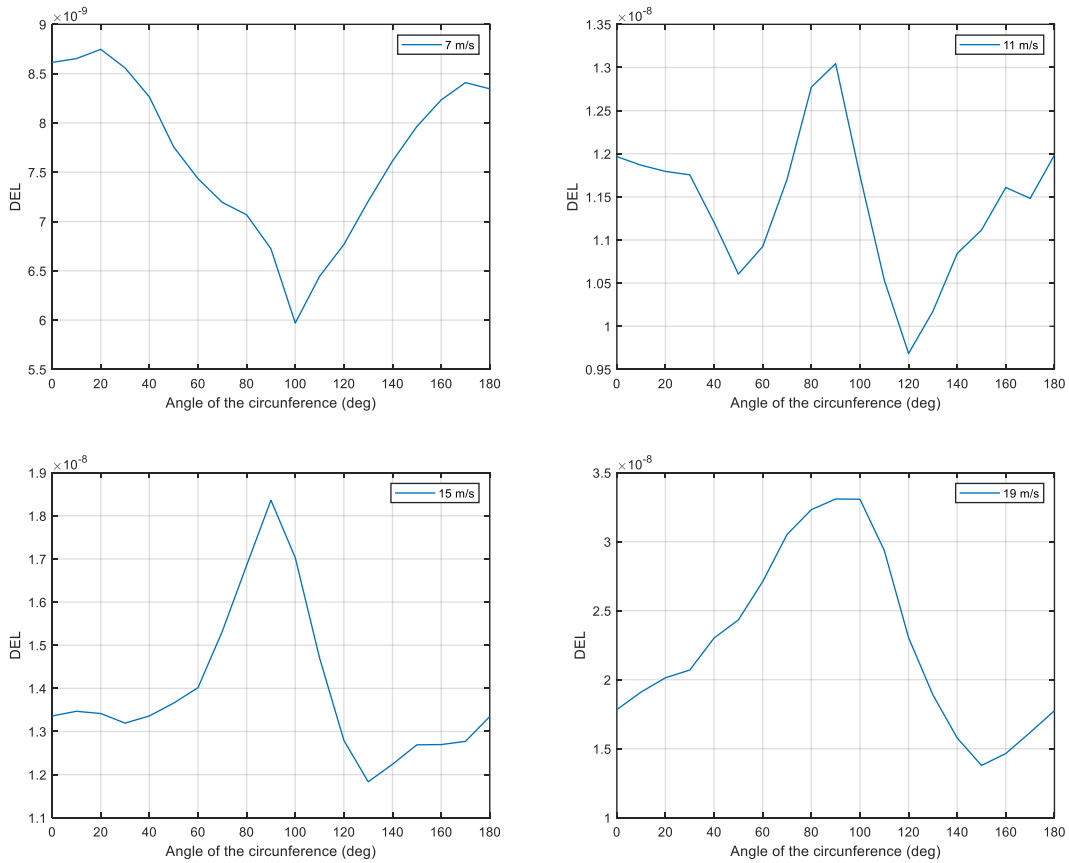
Where  $\sigma_a$  and  $\sigma_m$  are obtained from the Rainflow algorithm. Once obtained the N value for each cycle of the load history, the damage equivalent load (DEL) is computed by applying the Palmgren-Miner method:

$$DEL = \sum_i^n \frac{1}{N_i}$$

Where:

- N is the total number of cycles counted by the Rainflow algorithm
- $N_i$  is the number of cycles the point can withstand for a given cycle characterized by  $\sigma_m$  and  $\sigma_a$

The DEL varies along the different points in the circumference as well as with the wind speed because it depends on the pitch angle and the ratio between the aerodynamic and gravitational forces [22]. Figure 59 shows the DEL along the different points on the circumference, for different wind speeds:



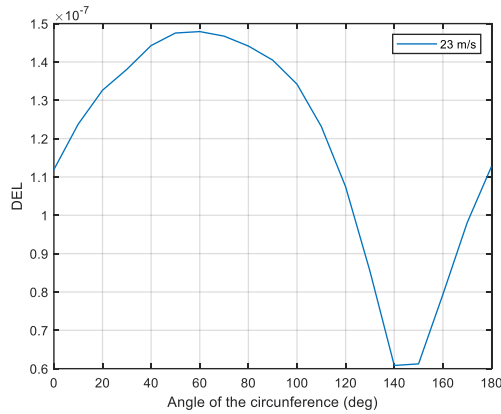


Figure 59. DEL along blade root circumference for 7, 11, 15, 19, 23 m/s wind speeds

For most of the wind speed spectrum (approximately 9 to 21 m/s), the critical angle is  $\beta = 90^\circ$  as it is the point with the highest DEL. This means that the flapwise moment ( $M_y$ ) due to the thrust of the wind, is predominant over the edgewise moment ( $M_x$ ) or torque of the generator. For cases where the wind speed is lower, the reverse is true, and the angles around  $\beta = 90^\circ$  or  $\beta = 100^\circ$  suffer the least DEL. However, the effect of the DEL in these cases is not as noticeable precisely because the wind speed is low. Finally, when the wind speed is higher, the points that suffer most from the effect of the loads are those located around  $\beta = [40^\circ, 90^\circ]$ . With this information, it seems likely that the point with the highest DEL is  $\beta = 90^\circ$ .

The effect of the wind speed on the DEL can be seen on figure 60, which shows the angle  $\beta = 90^\circ$ .

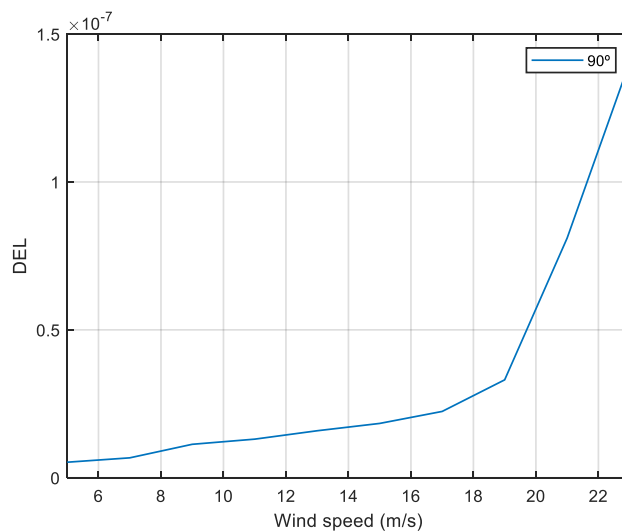


Figure 60. DEL for different wind speeds  $\beta = 90^\circ$

As expected, lower wind speeds produce less damage on the blade than higher ones. As seen on the last chapter, for higher wind speeds, in particular, higher than the rated one of the wind turbine, the mean components of the thrust force and bending moment decrease, but the amplitude of the oscillations becomes greater. This explains the increase of the DEL for the bigger wind speeds. This figure is important, as it allows to relate the DEL of each point (in this case, the critical angle) of the section with the corresponding wind speed.

To obtain the service life of the blade root, the actual wind speed has to be taken into account. For this purpose, the DEL curve in figure 60 is interpolated with the occurrence of the wind speed (figure 36), which represents the real environmental conditions in Pantelleria.

To calculate the mean DEL over a year with these conditions the next expression is used, which takes into account that only 590 seconds of conditions where simulated (600 s of which the first ten have been disregarded):

$$Mean\ DEL = \sum_v \left( \frac{3600}{590} \cdot DEL_v \right) \cdot (occ_v \cdot 24 \cdot 365)$$

Where:

- $DEL_v$  is the DEL associated with the wind speed  $v$  for the 590 seconds of simulation
- $occ_v$  is the occurrence of the wind speed  $v$

The resulting mean DEL over a year is represented on figure 61. As discussed above, the critical angle of the blade root section is  $\beta = 90^\circ$  which has an average annual damage of  $6.0795e-04$ .

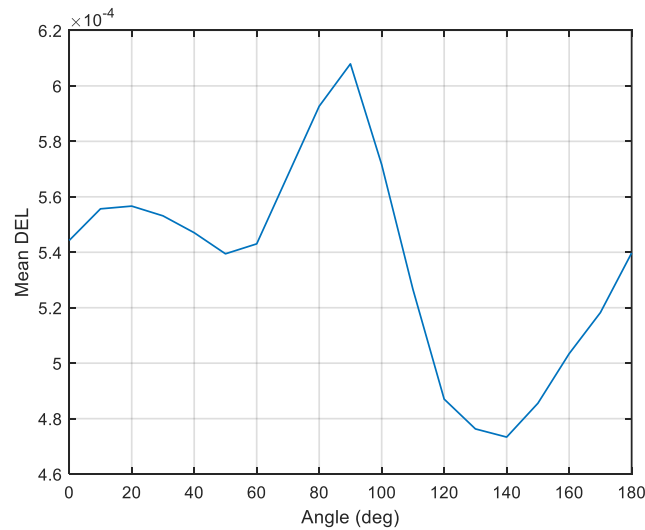


Figure 61. Mean DEL on blade root

The service life, in years can be computed as one over the mean DEL:

$$L = \frac{1}{\sum_v \left( \frac{3600}{590} \cdot DEL_v \right) \cdot (occ_v \cdot 24 \cdot 365)}$$

The service life of the root section is shown in figure 62. On table 11, the different points of the section are compared.

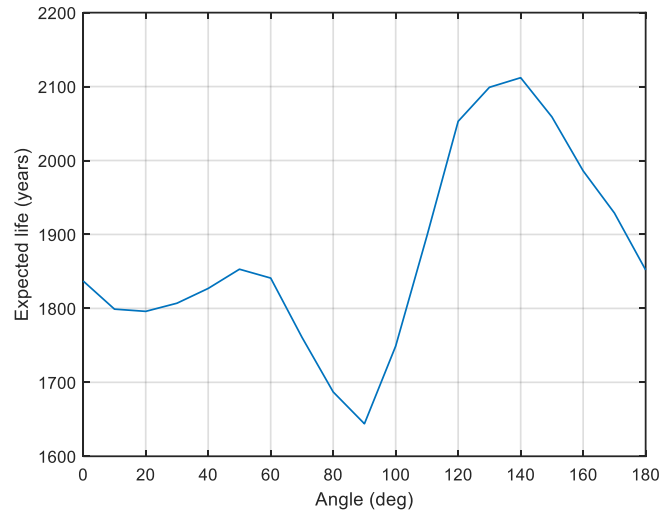


Figure 62. Service life on blade root

Table 11. Service life at the blade root

Angle $\beta$ (degrees)	Service life (years)
0°	1837
10°	1799
20°	1796
30°	1807
40°	1827
50°	1853
60°	1841
70°	1761
80°	1687
<b>90°</b>	<b>1644</b>
100°	1749
110°	1898
120°	2053
130°	2099
140°	2112
150°	2059
160°	1986
170°	1929
180°	1852

### 6.1.3. Results analysis

The service life of the section is the one of the most critical angle, which in this case is 1644 years. This result is very high compared to the average lifetime of a wind turbine, which ranges from 20 to 30 years. This is due to several reasons. Firstly, the fatigue analysis carried out in this work is very simple, as it only considers axial stresses, and disregards shear stresses. The shear stress can also be very high and lead to other types of failure, such as inter-fibre failure. In the present analysis, which is unidirectional, only tensile/compression failure has been considered.

In order to take into account shear and torsional stresses and thus other types of failure, a multi-axial fatigue analysis should be carried out.

Secondly, the constant life diagram used is linear. This is only an approximation and may underestimate the effect of the mean stress, so as a next step, a curve that better fits the fatigue properties of the material could be used.

In the paper “Development of a simplified blade root fatigue analysis for floating offshore wind turbines” (Sirigu, et al, 2022), different simplified models of the wind turbine are compared under the same fatigue approach used here, to check the validity of MOST (numerical model for floating offshore wind developed by the Politecnico di Torino). The paper compares the service life under three different cases:

- MOST: with three DOF on the platform, a rigid body blade model and simplified aerodynamics
- FAST (simplified): with three DOF on the platform and a rigid boy blade model
- FAST (complete): with six DOF on the platform, more complex aerodynamics and a flexible blade model

The only different between the FAST complete model and the one used in this work is the use of BeamDyn into FAST, to obtain the internal forces and moments on the blades.

Table 12 shows a comparison on the results obtained between the three models previously described and the one used in this work. As can be seen, as the complexity of the model increases the service life becomes higher. As stated by Sirigu, et al, 2022, “The complete version of FAST shows smaller peaks and less oscillations of bending moment (My) due to the flexibility of the blades” which results in less amplitude in the stress cycle. This explains why the complete models show a higher fatigue life.

*Table 12. Comparison between service life using different models*

<b>Model</b>	<b>Service life (years)</b>
MOST [22]	591
FAST (simplified) [22]	581
FAST (without BeamDyn) [22]	1215
FAST (with BeamDyn)	1644

As discussed in the paper “Comparison of blade optimisation strategies for the IEA 15MW reference turbine” (Scott & Graves, 2022) [26], in which a structural analysis of the 15 MW wind turbine’s blades using the finite element analyses, most critical failure mode is the inter-fibre failure at 15-20% of the blade length, while the blade root shows lower damage, because the blade root’s thickness is mainly driven by the high stiffness required for this section. It is important to emphasise that these results correspond to static material failure analyses and not to dynamic cases, such as fatigue. However, they can be used as a guide for the study of fatigue in the rest of the blade.

In the following, some sections between the 10-30% of the blade length are studied with the same approach to see if results, as expected, will be more realistic.

## 6.2. Fatigue analysis on blade sections

The change of blade shape from root to airfoil occurs between 2% and 15% of the blade length. In this transition zone, the loads are still quite high as it is close to the cantilever, and it is likely that the most critical section for fatigue failure is located here. Taking this into account and the above mentioned in the previous section, three airfoils are studied in this section, located at 12%, 20% and 28% of the blade length. The software BECAS is used as a postprocessor to get the stress based on the forces.

### 6.2.1. Postprocessing of the forces

The data coming from the simulations is stored in different matlab structures for each wind speed and sea state. It is remembered that the internal forces of the blade available as data, correspond to nine different sections almost evenly distributed along the blade span. For each of the sections, the forces are stored in a matrix of dimensions 1.200.000x6, which correspond to the simulations made with BeamDyn (10 minutes of simulation time with a time step of 0,0005s).

These data are post processed with the help of a matlab script: the first ten seconds of simulations are disregarded, the dimensions are reduced, and the forces are interpolated to the desired sections of the blade. The procedure is explained below:

To reduce the computational time for the calculations, it is helpful to reduce the dimensions of the vectors of the internal forces. This can be done as long as the accuracy or quality of the results is not reduced. In this case, the downsizing of the force vector does not affect the precision as the time step used in the simulations is sufficiently small, as shown in figure 63: figure 63 left shows the original size vector whereas figure 63 right shows the reduced-dimension vector.

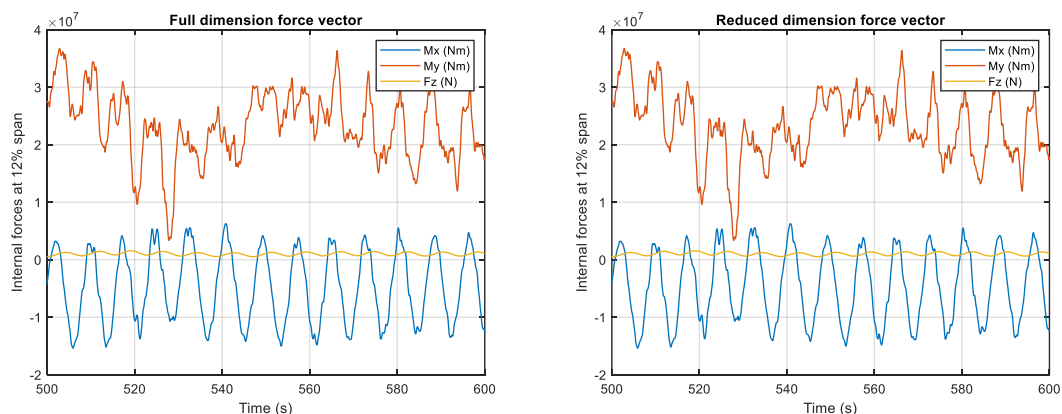


Figure 63. Downscaling of the force vector for the 12% blade length section. Full (left) vs reduced (right)

The forces are reduced 10 times its dimension in time. While the original vectors have time dimensions of 1.200.000-time length, the reduced ones are 180.000 long.

The last step is to interpolate the internal forces to the three sections to be studied. From the available nodes, each at a different blade length, the forces are obtained in the sections of 12%, 20% and 28% of the blade length. Linear interpolation has been used for the sake of simplicity. Table 13 shows the span of the sections in which the data are available (the nine nodes resulting

from BeamDyn output) and the span of the three sections of study in which the forces are obtained by interpolation.

Table 13. Span of the sections

Section	Span (%)	Internal forces
Node 1	0	BeamDyn output
<b>12% Section</b>	<b>12</b>	<b>Linear interpolation</b>
Node 2	12,5	BeamDyn output
<b>20% Section</b>	<b>20</b>	<b>Linear interpolation</b>
Node 3	25	BeamDyn output
<b>28% Section</b>	<b>28</b>	<b>Linear interpolation</b>
Node 4	37,5	BeamDyn output
Node 5	50	BeamDyn output
Node 6	62,5	BeamDyn output
Node 7	75	BeamDyn output
Node 8	87,5	BeamDyn output
Node 9	100	BeamDyn output

The resulting forces are stored in text files (which is the file format that BECAS needs as an input) for the different wind speeds, as specified below:

- LOADS\_5.in
- LOADS\_7.in
- LOADS\_9.in
- LOADS\_11.in
- LOADS\_13.in
- LOADS\_15.in
- LOADS\_17.in
- LOADS\_19.in
- LOADS\_21.in
- LOADS\_23.in

This process is repeated for the three different sections as each has different internal reaction forces. The resulting interpolated forces are shown below: figure 64 shows the bending moment  $M_x$  (in Nm) for the three sections; figure 65 and figure 66 show the bending moment  $M_y$  (Nm) and the axial force  $F_z$  (N), respectively.

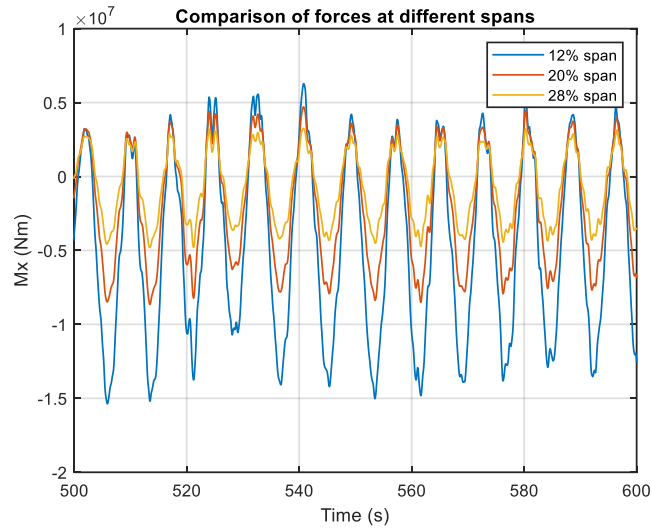


Figure 64. Bending moment  $M_x$  along the three study sections

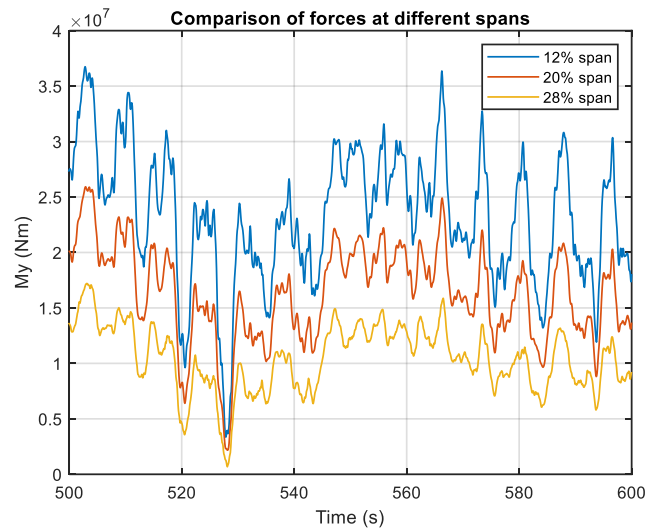


Figure 65. Bending moment  $M_y$  along the three study sections

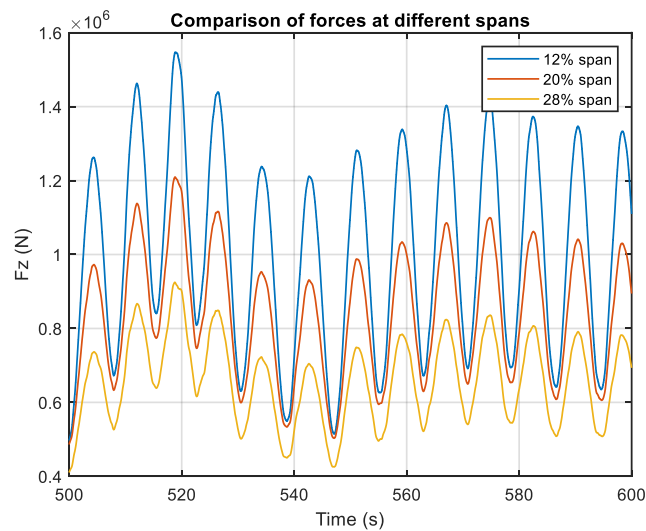


Figure 66. Axial force  $F_z$  along the three study sections

As expected, and as seen in the chapter on the analysis of the simulations, the internal forces decrease as the blade length increases. The 12% blade length section shows that both the bending moments and axial force present higher amplitude in the oscillations than the 20% blade length section. At the same time, in the latter, forces are greater than the ones on the 28% blade length section. Fatigue analysis will determine which of these is the most critical.

### 6.2.2. Cross-sections properties

In order for BECAS to perform the analysis on the cross-sections, several data of the airfoils are needed as an input. The inputs are separated in different files for each airfoil, which are specified below:

The first input are the nodal positions: an array with the list of nodal positions (x coordinate and y coordinate of the airfoil). Each of the node represents a point in the airfoil and is used to build the 2-D finite element mesh of the cross section.

The second input file contents the information of the elements of the mesh: it is an array with the element connectivity table where for each element a label is indicated, as well as the node labels of which it is composed. BECAS supports different element types:

- Q4 elemet: linear rectangular four node plane element
- Q8 elemet: quadratic rectangular eight node plane element
- Q8R elemet: quadratic rectangular eight node plane element using reduced integration
- T6 elemet: quadratic triangular six node plane element

However only linear rectangular elements are used here to create the meshes of the airfoils. That is, every element is composed of rectangles of four nodes. For the three sections, the meshes consist of 488 nodes and 372 elements.

The third input file specifies a material number for each element, as well as a fiber angle and a fiber plane angle for each of them. Figure 67 shows the sections sorted by colour according to their material. The materials of which the airfoils are made up are and its labelling is shown in table 14:

*Table 14. Material labels of the airfoils*

<b>Material name</b>	<b>Material number</b>
Biaxial fiberglass	1
Carbon fiber	2
Medium density foam	3
Gelcoat	4
Triaxial fiberglass	5
Uniaxial fiberglass	6

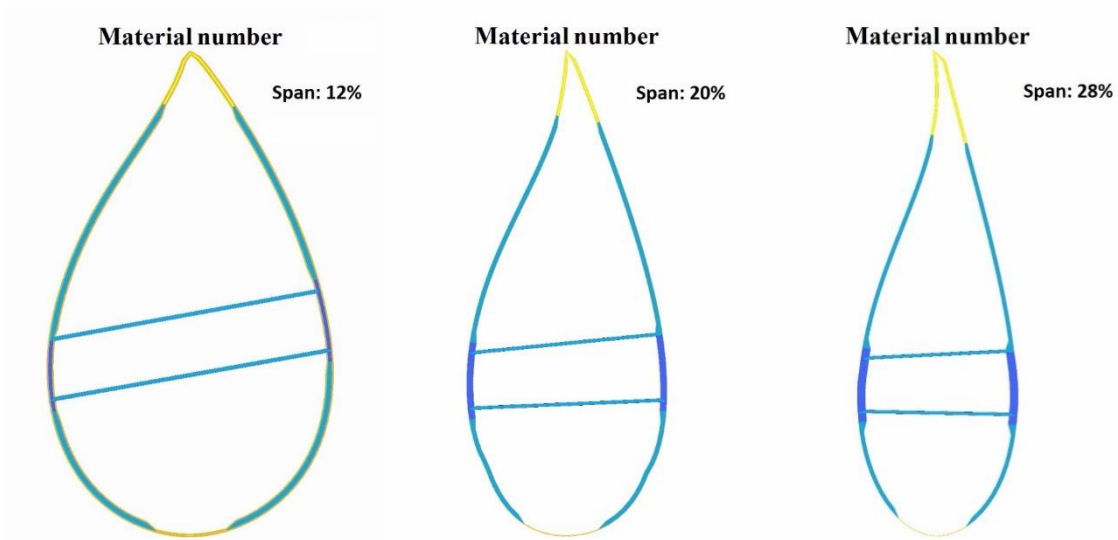


Figure 67. Material classification of the airfoils

Each of the material properties are specified in a fourth input file. The material mechanical properties are included here and are needed to retrieve the stresses from the forces. The properties are given with respect to the material coordinate system and are defined as:

- $E_{11}$ : the Young modulus of material the 1 direction (Pa)
- $E_{22}$ : the Young modulus of material the 2 direction (Pa)
- $E_{33}$ : the Young modulus of material the 3 direction (Pa)
- $G_{12}$ : the shear modulus in the 12 plane (Pa)
- $G_{13}$ : the shear modulus in the 13 plane (Pa)
- $G_{23}$ : the shear modulus in the 23 plane (Pa)
- $\nu_{12}$ : the Poisson's ratio in the 12 plane
- $\nu_{13}$ : the Poisson's ratio in the 13 plane
- $\nu_{23}$ : the Poisson's ratio in the 23 plane
- $\rho$ : the material density ( $\text{kg/m}^3$ )

The materials mechanical properties are shown in table 15. All of them have been taken from the IEA 15 MW ontology file which describes the blade geometry and the materials characteristics.

Table 15. Mechanical properties of the airfoil materials

Property	Material 1	Material 2	Material 3	Material 4	Material 5	Material 6
$E_{11}$ (Pa)	1.110E+10	1.145E+11	1.292E+08	3.440E+09	2.870E+10	4.460E+10
$E_{22}$ (Pa)	1.110E+10	8.390E+09	1.292E+08	3.440E+09	1.660E+10	1.700E+10
$E_{33}$ (Pa)	1.670E+10	8.390E+09	1.292E+08	3.440E+09	1.670E+10	1.670E+10
$G_{12}$ (Pa)	1.353E+10	5.990E+09	4.894E+07	1.323E+09	8.400E+09	3.270E+09
$G_{13}$ (Pa)	3.490E+09	5.990E+09	4.894E+07	1.323E+09	3.490E+09	3.480E+09
$G_{23}$ (Pa)	3.490E+09	5.990E+09	4.894E+07	1.323E+09	3.490E+09	3.500E+09
$\nu_{12}$	0.5	0.27	0.32	0.3	0.5	0.262
$\nu_{13}$	0.066	0.27	0.32	0.3	0	0.35
$\nu_{23}$	0.066	0.27	0.32	0.3	0.17	0.264
$\rho$ ( $\text{kg/m}^3$ )	1.940E+03	1.220E+03	1.300E+02	1.235E+03	1.940E+03	1.940E+03

The last input file contains the material strength characteristics, necessary for the material failure analysis as well as the fatigue analysis. Among them, the ones needed for the fatigue purposes are:

- $\sigma_{11}^t$  tensile strength in the 1 direction (Pa)
- $\sigma_{22}^t$  tensile strength in the 2 direction (Pa)
- $\sigma_{33}^t$  tensile strength in the 3 direction (Pa)
- $\tau_{12}$  shear strength in the 12 plane (Pa)
- $\tau_{13}$  shear strength in the 13 plane (Pa)
- $\tau_{23}$  shear strength in the 23 plane (Pa)
- $\sigma_{11}^c$  compressive strength in the 1 direction (Pa)
- $\sigma_{22}^c$  compressive strength in the 2 direction (Pa)
- $\sigma_{33}^c$  compressive strength in the 3 direction (Pa)
- m slope of the SN curve

The strength characteristics are shown in table 16. The data has been taken from the IEA 15 MW ontology file.

Table 16. Strength characteristics of the airfoil materials

Property	Material 1	Material 2	Material 3	Material 4	Material 5	Material 6
$\sigma_{11}^t$ (Pa)	42900000	1.55E+09	2083000	74	3.96E+08	6.09E+08
$\sigma_{22}^t$ (Pa)	42600000	7.73E+08	2083000	74	76400000	38100000
$\sigma_{33}^t$ (Pa)	15300000	7.73E+08	2083000	74	15300000	15290000
$\tau_{12}$ (Pa)	1.03E+08	3.87E+08	1250000	21260000	1.03E+08	18910000
$\tau_{13}$ (Pa)	17200000	3.87E+08	1250000	21260000	17200000	17240000
$\tau_{23}$ (Pa)	13200000	3.87E+08	1250000	21260000	13200000	13160000
$\sigma_{11}^c$ (Pa)	-7.1E+07	-1E+09	-1563000	-87	-4.5E+08	-4.7E+08
$\sigma_{22}^c$ (Pa)	-7.1E+07	-5.2E+08	-1563000	-87	-1.7E+08	-1.1E+08
$\sigma_{33}^c$ (Pa)	-1.1E+08	-5.2E+08	-1563000	-87	-1.1E+08	-1.1E+08
m	10	16.1	10	10	10	10

With these input files it is possible to compute the cross-section properties needed for the stress analysis that will come after it: stiffness and mass matrix, as well as the position of the shear, elastic and mass centres. The stiffness matrix of the cross section is especially important, as conforms the constitutive equation of the problem.

The mass and stiffness matrix of the three cross sections are shown below. The subscript refers to the span of the cross section.

$$M_{12\%} = \begin{bmatrix} 1.2879 & 0 & 0 & 0 & 0 & -0.5131 \\ 0 & 1.2879 & 0 & 0 & 0 & 0.0332 \\ 0 & 0 & 1.2879 & 0.5131 & -0.0332 & 0 \\ 0 & 0 & 0.5131 & 3.8362 & -0.1118 & 0 \\ 0 & 0 & -0.0332 & -0.1118 & 1.6006 & 0 \\ -0.5131 & 0.0332 & 0 & 0 & 0 & 5.4367 \end{bmatrix} \cdot 1.0e + 03$$

$$\begin{aligned}
K_{12\%} &= \begin{bmatrix} 0.1549 & 0.0077 & 0 & 0 & 0 & 0.0175 \\ 0.0077 & 0.3167 & 0 & 0 & 0 & 0.0136 \\ 0 & 0 & 2.4826 & 0.8684 & -0.1157 & 0 \\ 0 & 0 & 0.8684 & 6.0250 & -0.5061 & 0 \\ 0 & 0 & -0.1157 & -0.5061 & 3.8878 & 0 \\ 0.0175 & 0.0136 & 0 & 0 & 0 & 1.4620 \end{bmatrix} \cdot 1.0e + 10 \\
M_{20\%} &= \begin{bmatrix} 0.6204 & 0 & 0 & 0 & 0 & -0.5021 \\ 0 & 0.6204 & 0 & 0 & 0 & 0.0237 \\ 0 & 0 & 0.6204 & 0.5021 & -0.0237 & 0 \\ 0 & 0 & 0.5021 & 2.1263 & -0.0660 & 0 \\ 0 & 0 & -0.0237 & -0.0660 & 0.4355 & 0 \\ -0.5021 & 0.0237 & 0 & 0 & 0 & 2.5619 \end{bmatrix} \cdot 1.0e + 03 \\
K_{20\%} &= \begin{bmatrix} 0.0422 & 0.0025 & 0 & 0 & 0 & 0.0046 \\ 0.0025 & 0.0855 & 0 & 0 & 0 & 0.0050 \\ 0 & 0 & 2.1927 & 0.8625 & -0.0493 & 0 \\ 0 & 0 & 0.8625 & 3.9333 & -0.1918 & 0 \\ 0 & 0 & -0.0493 & -0.1918 & 2.2840 & 0 \\ 0.0046 & 0.0050 & 0 & 0 & 0 & 0.2377 \end{bmatrix} \cdot 1.0e + 10 \\
M_{28\%} &= \begin{bmatrix} 0.4822 & 0 & 0 & 0 & 0 & -0.4690 \\ 0 & 0.4822 & 0 & 0 & 0 & 0.0197 \\ 0 & 0 & 0.4822 & 0.4690 & -0.0197 & 0 \\ 0 & 0 & 0.4690 & 1.6565 & -0.0433 & 0 \\ 0 & 0 & -0.0197 & -0.0433 & 0.1934 & 0 \\ -0.4690 & 0.0197 & 0 & 0 & 0 & 1.8499 \end{bmatrix} \cdot 1.0e + 03 \\
K_{28\%} &= \begin{bmatrix} 0.0221 & 0.0002 & 0 & 0 & 0 & 0.0009 \\ 0.0002 & 0.0369 & 0 & 0 & 0 & 0.0026 \\ 0 & 0 & 2.1669 & 0.9028 & -0.0520 & 0 \\ 0 & 0 & 0.9028 & 3.3948 & -0.0684 & 0 \\ 0 & 0 & -0.0520 & -0.0684 & 1.2917 & 0 \\ 0.0009 & 0.0026 & 0 & 0 & 0 & 0.0639 \end{bmatrix} \cdot 1.0e + 10
\end{aligned}$$

BECAS also retrieves the position of some of the most important points of the section, such as the elastic and shear and mass centres. The shear center is defined as the point at which a load applied parallel to the plane of the section will produce no torsion (i.e., nor curvature,  $k_z = 0$ ). On the other hand, the elastic center is defined as the point where a force applied normal to the cross section will produce no bending curvatures (i.e.,  $k_x = k_y = 0$ ). It is remembered that the coordinate system of the cross section is the following:

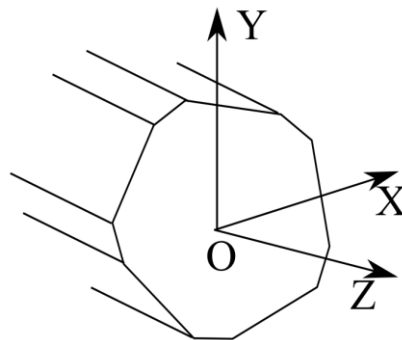


Figure 68. Cross section coordinate system

The position of the shear, elastic and mass centres of the airfoils are shown in figure 69:

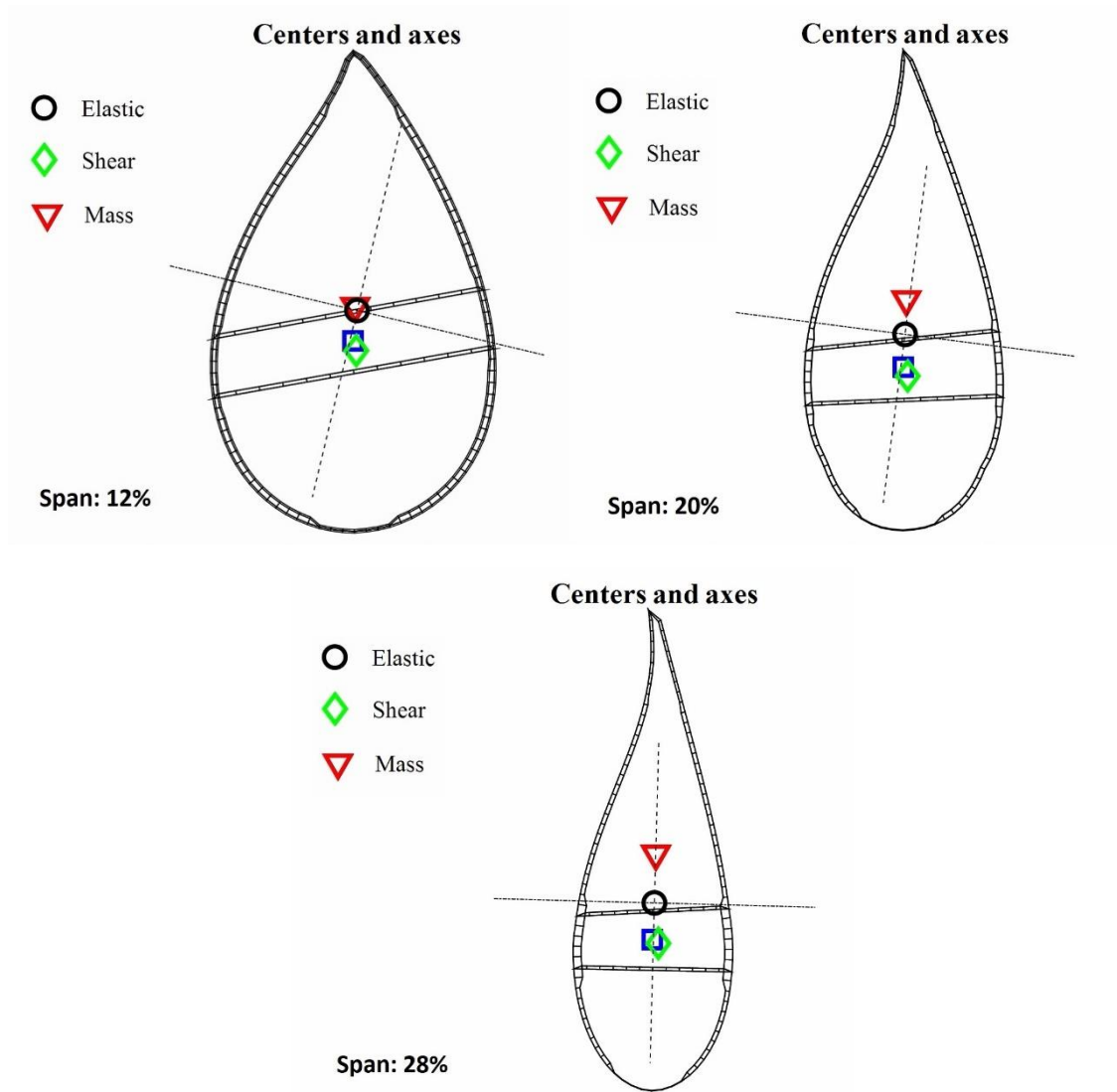


Figure 69. Position of the elastic, shear and mass centres

### 6.2.3. Stress recovery

Using the BECAS functionalities, it is possible to determine the three-dimensional strains and stress components at each element in the cross-section finite element mesh.

This is of great help for fatigue analysis, since for each vector of internal forces, the stress distribution at multiple points of the section (in each of the mesh elements) can be obtained. This is done for each of the internal forces state along time, and the stress distribution over time is obtained. Finally, the fatigue equations are applied on the elements and the most critical point of the section is found, which will determine the fatigue life.

The following figures show the deformations and stresses in the cross sections, for the same instant of time. The strain and stress,  $\epsilon$  and  $\sigma$ , are given as:

$$\epsilon^T = [\epsilon_{xx}, \epsilon_{yy}, 2\epsilon_{xy}, 2\epsilon_{xz}, 2\epsilon_{yz}, \epsilon_{zz}]$$

$$\sigma^T = [\sigma_{xx}, \sigma_{yy}, \sigma_{xy}, \sigma_{xz}, \sigma_{yz}, \sigma_{zz}]$$

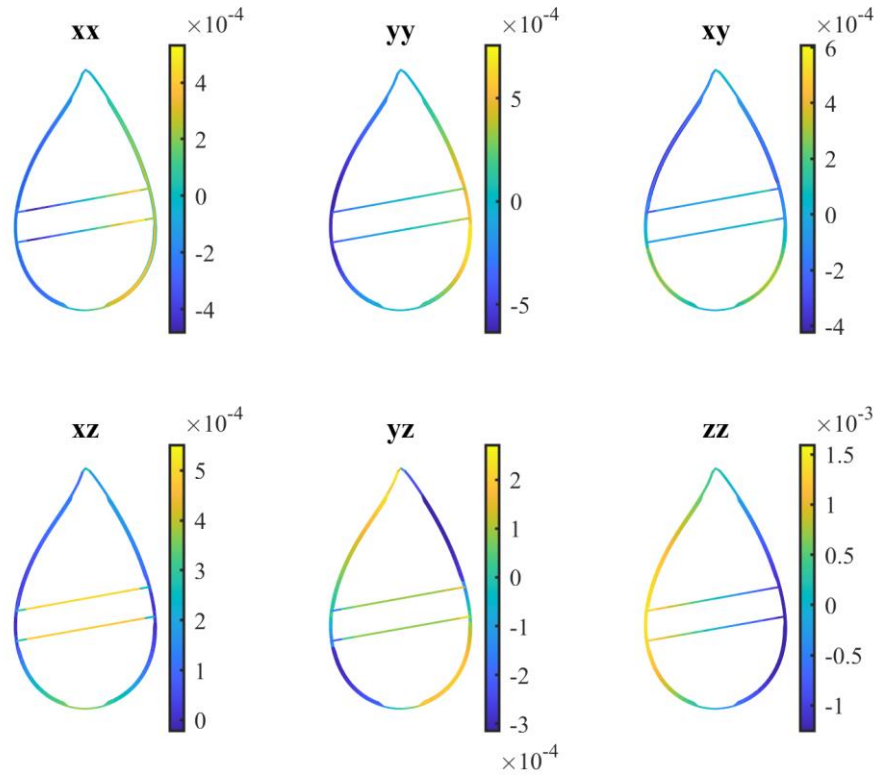


Figure 70. Strains on the 12% blade length cross-section

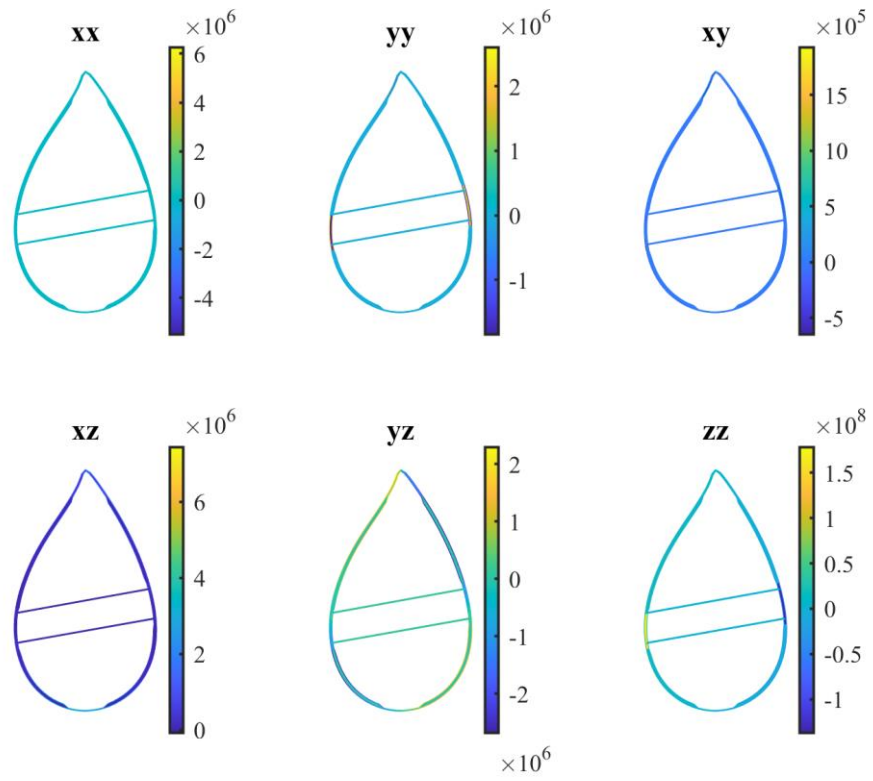


Figure 71. Stresses on the 12% blade length cross-section

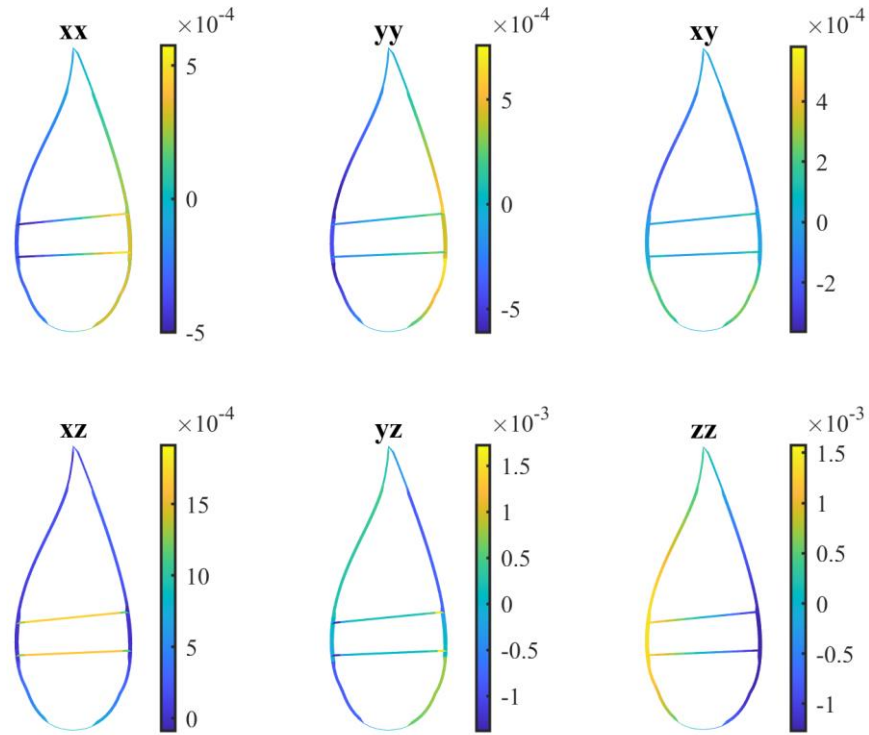


Figure 72. Strains on the 20% blade length cross-section

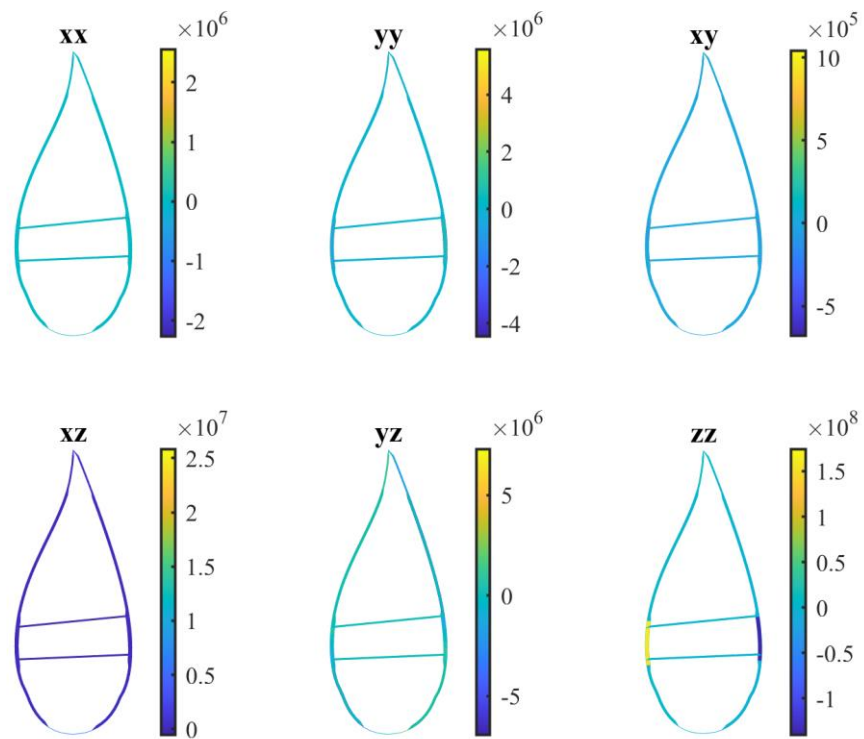


Figure 73. Stresses on the 20% blade length cross-section

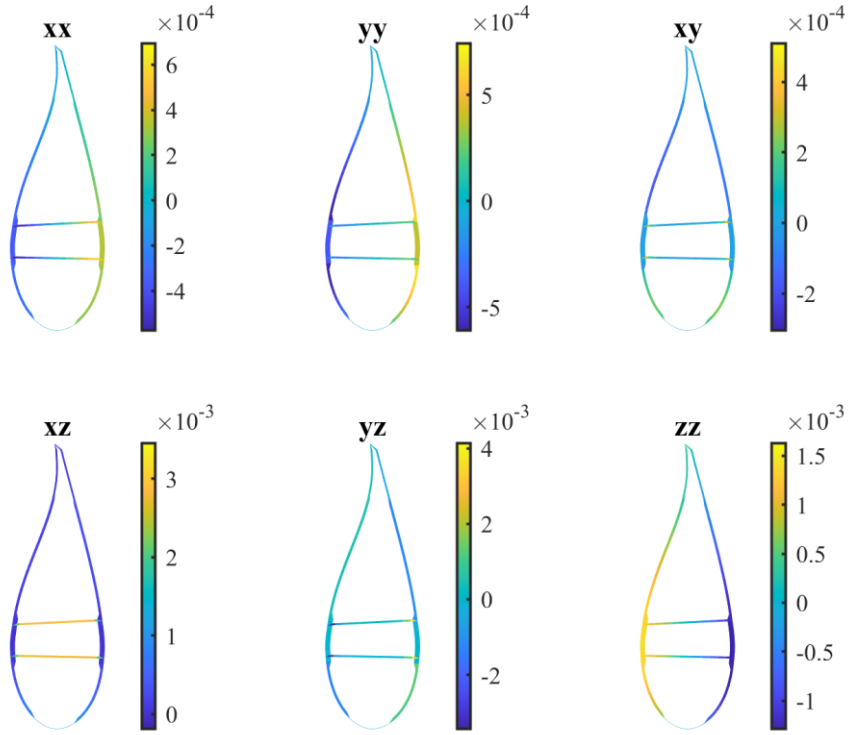


Figure 74. Strains on the 20% blade length cross-section

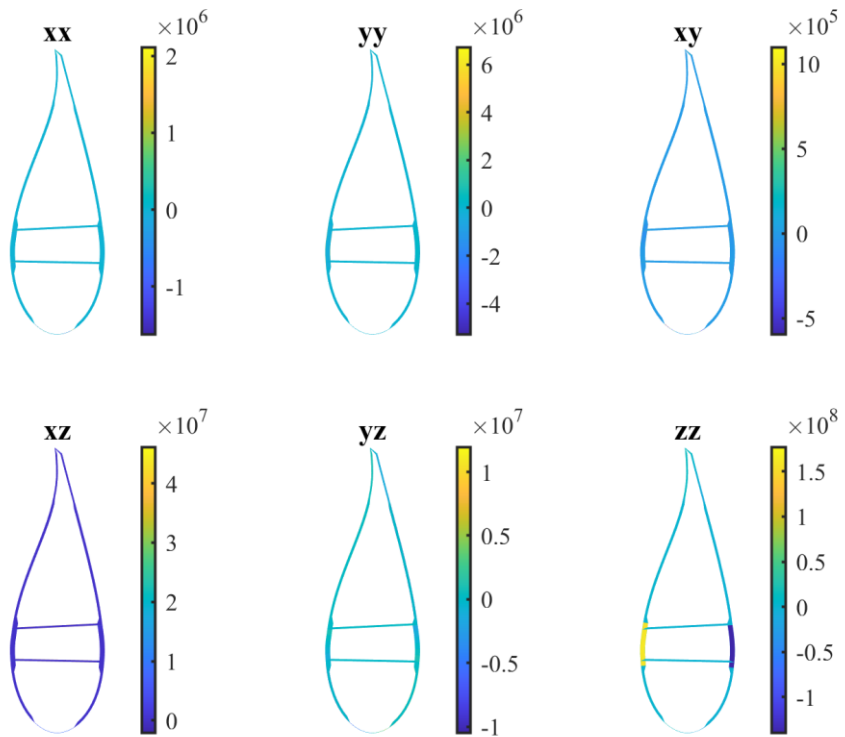


Figure 75. Stresses on the 28% blade length cross-section

In terms of stresses, it can be seen that the trend is the same for all three airfoils. The predominant stress is the axial stress ( $\sigma_{zz}$ ), which is at least one order of magnitude higher than the others. The areas subject to the highest axial stresses are the spar caps: on the pressure side the stresses are compressive, while on the suction side the predominant stresses are tensile. Meanwhile, the other areas of the airfoil are hardly subject to axial stresses.

Shear stresses (especially  $\sigma_{yz}$ ) also reach high values at certain points along the airfoil, although they are not taken into account for the uniaxial fatigue analysis. Both positive and negative values are distributed along the pressure and suction sides.

In terms of strains, the pressure side is subject to negative (compressive) deformations while the suction side is subject to positive (tensile) deformations. Shear deformation ( $\epsilon_{xz}$  and  $\epsilon_{yz}$ ) is predominant on the shear webs.

#### 6.2.4. Damage and life calculation

Having retrieved the stress history for all the elements on the cross sections, it is possible to apply the fatigue analysis seen in the previous section and determine the most critical point in the cross section and the fatigue life.

The applied methodology is the same as the one used in the blade root analysis:

$$S_e = S_{ut} - m \cdot \log_{10}(N)$$

$$\frac{\sigma_a}{S_e} + \frac{\sigma_m}{S_{ut}} = 1$$

Where  $\sigma_a$  and  $\sigma_m$  are obtained from the Rainflow algorithm for the stress cycle in each of the elements of the cross sections. The S-N equation and the Goodman line are joined to compute the value N of cycles that the pint of the cross section can withstand and de damage equivalent load (DEL) for each wind speed is computed:

$$N = 10^{\frac{S_{ut}^2 - \sigma_a \cdot S_{ut} - \sigma_m \cdot S_{ut}}{m(S_{ut} - \sigma_m)}}$$

$$DEL = \sum_i^n \frac{1}{N_i}$$

Figure 76 shows the maximum DEL on the cross sections for every wind speed. The results are similar to those of the blade root. For higher wind speeds the mean components of the thrust force and bending moment decrease, but the amplitude of the oscillations becomes grater, which explains the increase of the DEL. On the other hand, the section subjected to the most damage is the one located at 12% of the blade length, right in the transition zone of the blade shape between the root circumference and the airfoil. It is followed by the section furthest from the root (28% of the span). Lastly, the section receiving the least damage is the middle section, at 20% of the span.

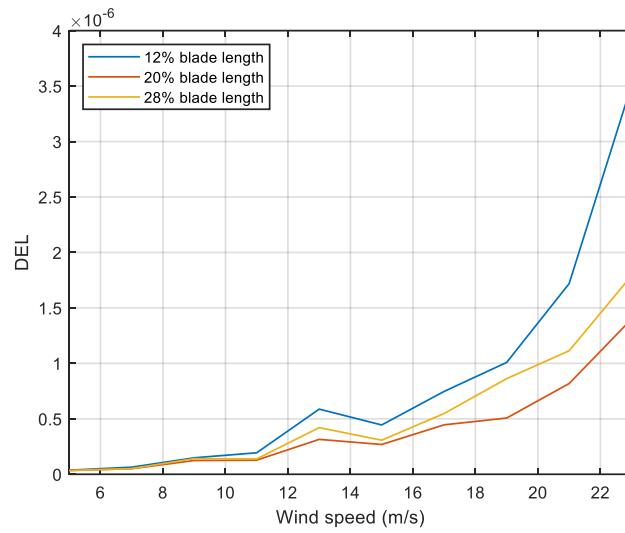


Figure 76. DEL as a function of the wind speed for the different cross sections

With this, the accumulated DEL after simulations can be shown in the cross-section. Figures 77, 78 and 79 show the damage in the whole section and the detail of the most damaged area.

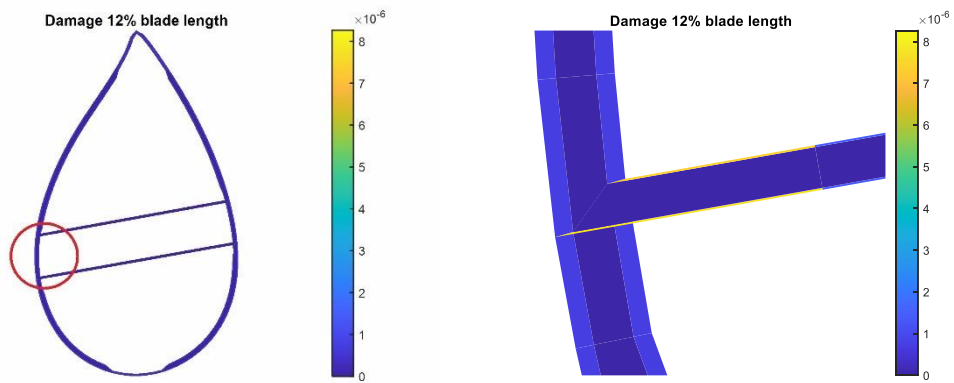


Figure 77. Damage at the cross section, 12% blade length

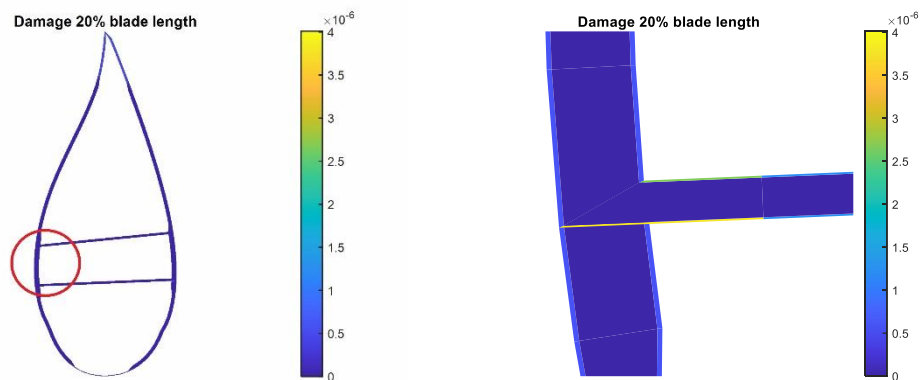


Figure 78. Damage at the cross section, 20% blade length

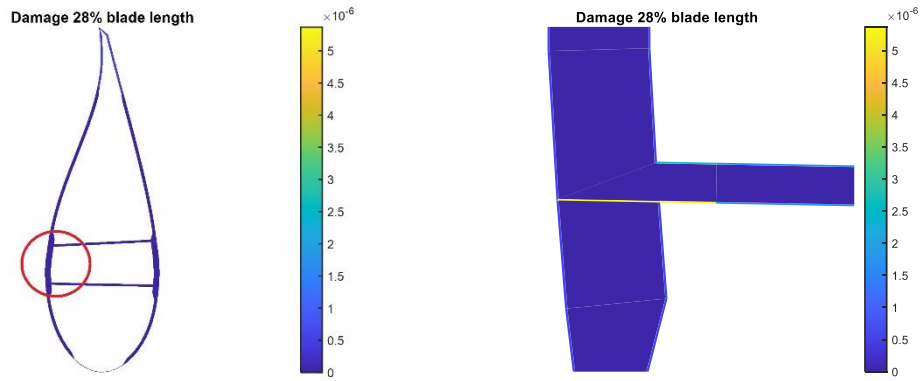


Figure 79. Damage at the cross section, 12% blade length

In all cases, the most damaged area is at the junction between the spar caps and the shear webs on the suction side of the airfoil.

Finally, the mean DEL over a year is computed interpolating the DEL of the last figure with the occurrence of the wind speed, and with that, the service life of the blade:

$$\text{Mean DEL} = \sum_v \left( \frac{3600}{590} \cdot \text{DEL}_v \right) \cdot (\text{occ}_v \cdot 24 \cdot 365)$$

$$L = \frac{1}{\sum_v \left( \frac{3600}{590} \cdot \text{DEL}_v \right) \cdot (\text{occ}_v \cdot 24 \cdot 365)}$$

The service life of the blade for the three sections is shown in table 17:

Table 17. Service life of the blade

Cross section	Service life (years)
12% of span	131
20% of span	200
28% of span	169

### 6.2.5. Results analysis

The results show that the fatigue life of the blade is 131 years and the critical section located at 12% of the blade length. The other sections would withstand more time (200 and 169 years for the 20 and 28% sections, respectively) and are therefore not critical.

The results are considerably higher than the actual average lifetime of the blade of a wind turbine (20-30 years) and this is due to several reasons. Firstly, in the design of the blades a high factor for fatigue failure was used. NREL used a 2.32 safety factor which causes the results in this work to be overestimated.

Secondly, it should be mentioned that only three cross sections of the blade have been studied. There could be other more critical sections that give a lower service life value. As mentioned, the most critical sections are found at the change of shape of the blade (from 2% to 15% of its length), as confirmed by the results of this work.

Lastly, as explained in the analysis of the fatigue life on the blade root, the approach followed here for the fatigue methodology is very simple, as it only considers axial stresses, and does not take into account shear stresses which can also be pretty high. Also, the constant life diagram used is linear, which can underestimate the effect of the mean stress.

## Conclusions

Wind energy plays a crucial role in the energy transition, being one of the most developed and established renewable energy sources in the world. In order to exploit the wind resource to the maximum, wind turbine farms are located at sea, and in particular, the new trend is to do so on floating platforms, further away from the coast. This allows to obtain a higher capacity factor thanks to the better quality of the wind resource, i.e., more energy is obtained for the same installed power. At the same time, the environmental impact is reduced, as is the high cost associated with foundations fixed to the seabed, which is replaced by those of the semi-submersible platform, which are much smaller.

However, moving generators away from the shore has its downside: maintenance becomes costly and has to be reduced as much as possible, so the design and simulation stages can save large costs if done properly. In this context, the prediction of the service life of wind turbines and, in particular, of the composite materials of which their blades are composed is of great importance.

This paper has presented the theory and methodology of fatigue analysis for this purpose, applied on the 15 MW offshore reference wind turbine. For this purpose, first of all, the design of the wind turbine has been used to perform simulations with realistic environmental conditions and load cases. With the help of the OpenFAST and BeamDyn as the simulation tool, the internal loads of different cross sections of the blade have been extracted.

These data have been post-processed with the help of the BECAS software to obtain the stress history at multiple points of different blade sections, based on the internal forces obtained in the simulations. With this, it is possible to apply fatigue theory and determine the service life of the blade.

This methodology has been applied to four different sections of the blade: the root, and three sections located at 12%, 20% and 28% of the blade length. The root of the blade is cantilevered and therefore is where the stresses are higher, however, it is governed by a high stiffness, making it not a critical area. Moving away from the root, the internal forces decrease but the blade section also reduces, so these sections become more critical. Specifically, the most critical section of those studied is the one located at 12% of the blade length, precisely in the transition zone from root circumferential shape to airfoil, which ranges from 2 to 15% of the length of the blade.

The result obtained is slightly overestimated due to the high safety factor used for fatigue failure in the blade design, as well as the simplifications assumed in this analysis which has only considered the uniaxial stress along the blade. However, the work is useful to identify the most critical zones of the blade under a realistic set of load cases.

## References

- [1] Ewind. What is wind energy? [Online] Available: <https://www.ewind.es/about-wind-energy/what-is-wind-energy>
- [2] Global Wind Report 2022. GWEC. [Online] Available: [https://gwec.net/wp-content/uploads/2022/04/Annual-Wind-Report-2022\\_screen\\_final\\_April.pdf](https://gwec.net/wp-content/uploads/2022/04/Annual-Wind-Report-2022_screen_final_April.pdf)
- [3] Wind energy in Europe: 2021 Statistics and the outlook for 2022-2026. 2022. *Wind EUROPE*. [Online] 2022. <https://windeurope.org/intelligence-platform/product/windenergy-in-europe-2021-statistics-and-the-outlook-for-2022-2026/>
- [4] Offshore Wind Outlook 2019. IEA. [Online] Available: <https://www.iea.org/reports/offshore-wind-outlook-2019>
- [5] GWEC Report Floating offshore wind. 2022. [Online] Available: A global opportunity. <https://gwec.net/wp-content/uploads/2022/03/GWEC-Report-Floating-Offshore-Wind-A-Global-Opportunity.pdf>
- [6] Malcolm Forbes-Cable. 2020. Offshore wind propels the UK's net zero ambitions. [Online] Available: <https://www.woodmac.com/news/opinion/offshore-wind-propels-the-uks-net-zero-ambitions/>
- [7] Sutherland, H. 1999. A Summary of the Fatigue Properties of Wind Turbine Materials. *Sandia National Laboratories*.
- [8] ASTM E206. Standard definitions of terms relating to fatigue testing and the statistical analysis of fatigue data (R 1979) (E1-1985).
- [9] "What is metal fatigue?" *YENA Engineering* [Online] Available: <https://yenaengineering.nl/what-is-metal-fatigue/>
- [10] Raffaella Sesana. 2021-2022. Applied mechanics and Machine design. *Politecnico di Torino*.
- [11] Matha, D. 2009. Model Development and Loads Analysis of an Offshore Wind Turbine on a Tension Leg Platform, with a Comparison to Other Floating Turbine Concepts. *National Renewable Energy Laboratory*.
- [12] Calvin M. Stewart. 2021. Fatigue Analysis for Extreme Environments, Stress-Life Approach. *Department of Mechanical Engineering, University of Texas*.
- [13] Gaertner, E. et al. 2020. Definition of the IEA Wind 15- Megawatt Offshore Reference Wind Turbine Technical Report. *National Renewable Energy Laboratory*.
- [14] Allen, C. et al. 2020. Definition of the UMaine Voltturn US-S Reference Platform Developed for the IEA Wind 15- Megawatt Offshore Reference Wind Turbine Technical Report. *National Renewable Energy Laboratory*.
- [15] Spar Cap and Shear Web Bonding Inspection Solution for Wind Turbine Blades. Simon Alain. [Online] Available: <https://www.olympus-ims.com/en/applications/shear-web-bonding-inspection/>

- [16] Blasques JP, Bitsche R, Fedorov V, and Eder M. 2013. Applications of the BEam Cross section Analysis Software (BECAS). *Department of Wind Energy, Technical University of Denmark*.
- [17] Roland Feil, Tobias Pflumm, Pietro Bortolotti, Marco Morandini. 2020. A cross-sectional aeroelastic analysis and structural optimization tool for slender composite structures. *Composite Structures* 253.
- [18] Wang, Q., Sprague, M. A., Jonkman, J., Johnson, N., & Jonkman, B. 2017. BeamDyn: a high-fidelity wind turbine blade solver in the FAST modular framework. *Wind Energy*, 20(8), 1439–1462.
- [19] OpenFAST. NREL. [Online]  
[https://openfast.readthedocs.io/en/main/source/user/fast\\_to\\_openfast.html](https://openfast.readthedocs.io/en/main/source/user/fast_to_openfast.html)
- [20] Blasques, J. P., & Stolpe, M. 2012. Multi-material topology optimization of laminated composite beam cross sections. *Composite Structures*, 94, 3278- 3289
- [21] Q. Wang, J. Jonkman, M. Sprague, and B. Jonkman. March 2016. BeamDyn User’s Guide and Theory Manual.
- [22] M. Sirigu, E. Faraggiana, A. Ghigo, E. Petracca, G. Mattiazzo & G. Bracco. 2022. Development of a simplified blade root fatigue analysis for floating offshore wind turbines. *Politecnico di Torino*.
- [23] IEC 61400. Wind Energy Generation Systems - Part 3-1: Design Requirements For Fixed Offshore Wind Turbines (June 2021).
- [24] Natarajan, Anand; Hansen, Morten Hartvig; Wang, Shaofeng. 2016. Design Load Basis for Offshore Wind turbines. *DTU Wind Energy Report No. E-0133*.
- [25] Sirigu, M. et al. 2022. Development of MOST, a Fast Simulation Model for Optimisation of Floating Offshore Wind Turbines in Simscape Multibody. *J. Phys.: Conf. Ser.* 2257 012003.
- [26] Scott, Samuel, & Peter Graves. 2022. Comparison of Blade Optimisation Strategies for the IEA 15MW Reference Turbine. *J. Phys.: Conf. Ser.* 2265.
- [27] Nikhar J. Abbas et al. 2022. A reference open-source controller for fixed and floating offshore wind turbines.
- [28] Massimo Sirigu. 2022. MOST – Hydrodynamics and control system. *Politecnico di Torino*.

## List of figures

Figure 1. New worldwide wind capacity predictions (2020-2030) [2] .....	1
Figure 2. The growth of total wind energy capacity in Europe, 2012-21 [3] .....	2
Figure 3. New wind installations in Europe in 2021 per country [3].....	3
Figure 4. Evolution of the largest commercially available wind turbines [4].....	4
Figure 5. Average simulated capacity factors for offshore wind worldwide [4].....	5
Figure 6. Floating offshore designs [6].....	6
Figure 7. Schematic S-N diagram for different fatigue critical structures [7] .....	7
Figure 8. Fatigue failure [9], [10].....	8
Figure 9. Characterization of a cyclic load [10] .....	9
Figure 10. Different stress ratios [10] .....	9
Figure 11. S-N curve [12] .....	10
Figure 12. Normalized S-N for a typical fiberglass composite, R=-1 [7].....	11
Figure 13. Typical symmetric Goodman Diagram [7].....	12
Figure 14. Different Goodman curves [10] .....	12
Figure 15. IEA-15-240 RWT and VoltturnUS-S reference platform [13].....	13
Figure 16. DTU FFA-W3 airfoil family used in the IEA Wind 15-MW blade design [13].....	15
Figure 17. Blade internal structure scheme [15].....	16
Figure 18. Blade cross sections at different spans [13].....	17
Figure 19. Platform view (left) and top-side view (right) [14] .....	18
Figure 20. Controller zones [28].....	19
Figure 21. Schematic description of the workflow for structural analysis of the wind turbine blades [16].....	21
Figure 22. Methodology to account for 3D structural designs in 1D beam finite element models [17] .....	22
Figure 23. Beam model (up) and shell model (down) of a wind turbine blade [16].....	23
Figure 24. Coupled interaction between BeamDyn and FAST [21].....	24
Figure 25. BeamDyn Blade Geometry - Top: Side View; Middle: Front View (Looking Downwind); Bottom: Cross Section View (Looking Toward the Tip, from the Root) [21].....	25
Figure 26. Wind speed distributions for 10, 14 and 18 m/s, 120s .....	29
Figure 27. Tip deflection on X axis for 10, 14, 18 m/s, 120s .....	31
Figure 28. Tip deflection on Y axis for 10, 14 and 18 m/s, 120s .....	32
Figure 29. Tip deflection on Z axis for 10, 14 and 18 m/s .....	32
Figure 30. Pitch angle for 10, 14 and 18 m/s .....	33
Figure 31. Deflection in nodes 1-9 for 10, 14 and 18 m/s, 120s .....	34
Figure 32. Maximum deflection, 10m/s and 120s .....	35
Figure 33. Three-dimensional deflexion, 10m/s and 120s.....	35
Figure 34. Maximum deflection on X (left) and Y (left) axes, 10m/s and 120s.....	36
Figure 35. Time step comparison of the tip deflection, between 0.0005s and 0.0002s.....	36
Figure 36. Occurrence of the wind speed in Pantelleria, Italy in ten years of data collection [22] .....	37
Figure 37. Normal pressure (pn) along blade length .....	39
Figure 38. Tangential pressure (pt) along blade length .....	39
Figure 39. Fx along the blade length .....	40
Figure 40. Fy along the blade length.....	40

Figure 41. Mx along the blade length .....	41
Figure 42. My along the blade length .....	41
Figure 43. Wind speed .....	43
Figure 44. Power .....	43
Figure 45. Rotor speed .....	44
Figure 46. DOF of the platform .....	45
Figure 47. Blade pitch angle .....	45
Figure 48. Tip deflection along X.....	46
Figure 49. Tip deflection along Y (left) and Z (right) .....	46
Figure 50. Maximum deflection. Wind speed is 13 m/s .....	47
Figure 51. Maximum deflection along X and Y. Wind speed is 13 m/s.....	47
Figure 52. Nodes deflection along X. Wind speed is 15 m/s.....	48
Figure 53. Nodes deflection along Y (left) and Z (right). Wind speed is 15 m/s .....	48
Figure 54. Blade root reaction forces.....	49
Figure 55. Internal forces at the blade nodes. Wind speed is 15 m/s .....	51
Figure 56. Blade root cross-section.....	52
Figure 57. Mechanical stress at the blade root. $\beta = 90^\circ$ and wind speed is 15 m/s.....	53
Figure 58. Closer look to the mechanical stress at the blade root, $\beta = 90^\circ$ and wind speed is 15 m/s .....	54
Figure 59. DEL along blade root circumference for 7, 11, 15, 19, 23 m/s wind speeds .....	56
Figure 60. DEL for different wind speeds $\beta = 90^\circ$ .....	56
Figure 61. Mean DEL on blade root.....	57
Figure 62. Service life on blade root .....	58
Figure 63. Downscaling of the force vector for the 12% blade length section. Full (left) vs reduced (right).....	60
Figure 64. Bending moment Mx along the three study sections .....	62
Figure 65. Bending moment My along the three study sections .....	62
Figure 66. Axial force Fz along the three study sections.....	62
Figure 67. Material classification of the airfoils .....	64
Figure 68. Cross section coordinate system.....	66
Figure 69. Position of the elastic, shear and mass centres .....	67
Figure 70. Strains on the 12% blade length cross-section .....	68
Figure 71. Stresses on the 12% blade length cross-section .....	68
Figure 72. Strains on the 20% blade length cross-section .....	69
Figure 73. Stresses on the 20% blade length cross-section .....	69
Figure 74. Strains on the 20% blade length cross-section .....	70
Figure 75. Stresses on the 28% blade length cross-section .....	70
Figure 76. DEL as a function of the wind speed for the different cross sections.....	72
Figure 77. Damage at the cross section, 12% blade length .....	72
Figure 78. Damage at the cross section, 20% blade length .....	72
Figure 79. Damage at the cross section, 12% blade length .....	73

# List of tables

Table 1. Key Parameters for the IEA Wind 15-MW Turbine [13] .....	14
Table 2. Blade Properties [13] .....	15
Table 3. Key points defining the blade geometry in the Reference Blade Coordinate system ..	26
Table 4. Input files variables.....	28
Table 5. Variables for the test simulations.....	30
Table 6. Quadrature points position vector in the reference blade coordinate system .....	30
Table 7. Output nodes position.....	31
Table 8. Wind and sea states used in the simulations .....	38
Table 9. Simulation inputs.....	42
Table 10. Geometry of the blade root cross-section and properties of the composite material [22] .....	52
Table 11. Service life at the blade root .....	58
Table 12. Comparison between service life using different models .....	59
Table 13. Span of the sections .....	61
Table 14. Material labels of the airfoils.....	63
Table 15. Mechanical properties of the airfoil materials.....	64
Table 16. Strength characteristics of the airfoil materials .....	65
Table 17. Service life of the blade .....	73